Designed synthesis and structural investigation of novel zeolites in the ABC-6 family
[Redacted version]

Ruxandra Georgiana Chitac

A thesis submitted for the degree of PhD
at the
University of St Andrews

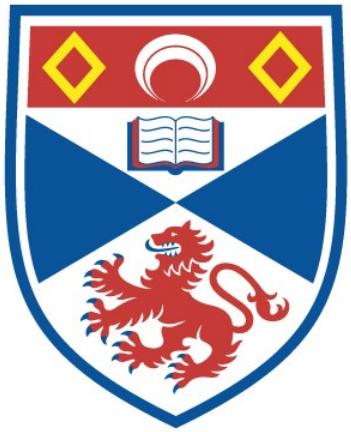

2023

Candidate's declaration

I, Ruxandra Georgiana Chitac, do hereby certify that this thesis, submitted for the degree of PhD, which is approximately 55,000 words in length, has been written by me, and that it is the record of work carried out by me, or principally by myself in collaboration with others as acknowledged, and that it has not been submitted in any previous application for any degree. I confirm that any appendices included in my thesis contain only material permitted by the 'Assessment of Postgraduate Research Students' policy.

I was admitted as a research student at the University of St Andrews in August 2019.

I received funding from an organisation or institution and have acknowledged the funder(s) in the full text of my thesis.

Date 22/08/2023 Signature of candidate

Supervisor's declaration

I hereby certify that the candidate has fulfilled the conditions of the Resolution and Regulations appropriate for the degree of PhD in the University of St Andrews and that the candidate is qualified to submit this thesis in application for that degree. I confirm that any appendices included in the thesis contain only material permitted by the 'Assessment of Postgraduate Research Students' policy.

Date 22/08/2023 Signature of supervisor

Permission for publication

In submitting this thesis to the University of St Andrews we understand that we are giving permission for it to be made available for use in accordance with the regulations of the University Library for the time being in force, subject to any copyright vested in the work not being affected thereby. We also understand, unless exempt by an award of an embargo as requested below, that the title and the abstract will be published, and that a copy of the work may be made and supplied to any bona fide library or research worker, that this thesis will be electronically accessible for personal or research use and that the library has the right to migrate this thesis into new electronic forms as required to ensure continued access to the thesis.

I, Ruxandra Georgiana Chitac, confirm that my thesis does not contain any third-party material that requires copyright clearance.

The following is an agreed request by candidate and supervisor regarding the publication of this thesis:

Printed copy

No embargo on print copy.

Electronic copy

Embargo on part (Abstract, Chapter 1 - Introduction, Chapter 2 - Methodology, Chapter 5 - Chapter 6 - Chapter 7 - General Conclusions and Future Work, Appendix) of electronic copy for a period of 3 years on the following ground(s):

- Publication would be commercially damaging to the researcher, or to the supervisor, or the University
- Publication would preclude future publication

Supporting statement for electronic embargo request

My research was sponsored by a commercial company and there are conditions on my research being made publicly available.

Title and Abstract

- I require an embargo on the abstract only.

Date 22/08/2023 Signature of candidate

Date 22/08/2023 Signature of supervisor

Underpinning Research Data or Digital Outputs

Candidate's declaration

I, Ruxandra Georgiana Chitac, understand that by declaring that I have original research data or digital outputs, I should make every effort in meeting the University's and research funders' requirements on the deposit and sharing of research data or research digital outputs.

Date 22/08/2023 Signature of candidate

Permission for publication of underpinning research data or digital outputs

We understand that for any original research data or digital outputs which are deposited, we are giving permission for them to be made available for use in accordance with the requirements of the University and research funders, for the time being in force.

We also understand that the title and the description will be published, and that the underpinning research data or digital outputs will be electronically accessible for use in accordance with the license specified at the point of deposit, unless exempt by award of an embargo as requested below.

The following is an agreed request by candidate and supervisor regarding the publication of underpinning research data or digital outputs:

Embargo on part (The research data connected to Chapters 5 and 6.) of electronic files for a period of 3 years on the following ground(s):

- Publication would be commercially damaging to the researcher, or to the supervisor, or the University (e.g. Intellectual Property Rights)
- Publication would preclude future publication

Supporting statement for embargo request

My research was sponsored by a commercial company and there are conditions on my research being made publicly available.

Title and Description

- I require an embargo on the description only

Date
22/08/2023

Signature of candidate

Date
22/08/2023

Signature of supervisor

This thesis is dedicated to my chemistry teacher from middle school, Mrs Elena Sunca, who inspired me to love chemistry and follow my passion for science.

Publications

Designed Synthesis of STA-30: A Small-Pore Zeolite Catalyst with Topology Type SWY

R. G. Chitac, J. Bradley, N. D. McNamara, A. Mayoral, A. Turrina and P. A. Wright, Chem. Mater., 2021, 33, 5242–5256.

STA-30, a new member of the SWY family of molecular sieves, methods of preparation and use

Inventors: R. G. Chitac, N. McNamara, A. Turrina, P. A. Wright, US20220333519A1, 2022 (published, in the examination period).

Co-templating in the Designed Synthesis of Small-pore Zeolite Catalysts

R. G. Chitac, M. D. Shannon, P. A. Cox, J. Mattock, P. A. Wright and A. Turrina, in AI-Guided Design and Property Prediction for Zeolites and Nanoporous Materials, eds. G. Sastre and F. Daeyaert, John Wiley & Sons Ltd, Hoboken, 2023, pp. 113–143.

Synthetic Control of Defect Structure and Resultant Hierarchical Extra-Large/Small-Pore Microporosity in Aluminosilicate Zeolite SWY

R. G. Chitac, V. L. Zholobenko, R. S. Fletcher, E. Softley, J. Bradley, A. Mayoral, A. Turrina and P. A. Wright, J. Am. Chem. Soc. 2023, 145, 40, 22097–22114.

Other contributions:

Cation Control of Cooperative CO2 Adsorption in Li-Containing Mixed Cation Forms of the Flexible Zeolite Merlinoite

V. M. Georgieva, E. L. Bruce, R. G. Chitac, M. M. Lozinska, A. M. Hall, C. A. Murray, R. I. Smith, A. Turrina and P. A. Wright, Chem. Mater., 2021, 33, 1157–1173.

Understanding the Anion-Templated, OSDA-Free, Interzeolite Conversion Synthesis of High Silica Zeolite ZK-5

M. M. Lozinska, E. L. Bruce, J. Mattock, R. G. Chitac, P. A. Cox, A. Turrina and P. A. Wright, *Chem. – A Eur. J.*, 2022, 28, e202201689.

Acknowledgements

I would like to thank my supervisors Prof. Paul Wright and Dr Alessandro Turrina for their support, guidance, and input. The many (online or in–person) conversations we have had over the past four years have contributed massively to my development as a researcher. Thank you for the challenges, the opportunities, and the ideas throughout this project.

My external collaborators provided invaluable help and taught me much about their particular fields. Paul Cox (University of Portsmouth) kindly answered my questions regarding computational chemistry. Mervyn Shannon (JM consultant) explained in detail structural aspects. Vladimir Zholobenko (Keele University) offered his expertise in FTIR spectroscopy and collaborated in the characterisation of some of the STA-30 zeolites. Ines Lezcano-Gonzalez and Andrew Beale (UCL) provided an insight into MTO and also tested some of the zeolites. Alvaro Mayoral (University of Zaragoza) collected STEM data that provided essential characterisation data.

This thesis would have not been possible without the help of many others who have aided in the characterisation of the many zeolites I have prepared. At University of St Andrews, I want to acknowledge Yuri Andreev for running the PXRD facilities, Gavin Peters for his assistance with the TGA and adsorption instruments, and Daniel Dawson, along with Malavika Manoj, for their work on solid–state NMR spectroscopy. I'm especially thankful to David Miller and Aaron Naden for their training and many insightful discussions on electron microscopy. Finally, I would like to give special thanks to Herbert Fruchtl who helped me use the HPC cluster. At Johnson Matthey, I would like to express my appreciation for Jonathan Bradley for all the NMR studies he has carried out, for Rob Fletcher, along with Emma Softley, for their work on adsorption studies and for Nicholas McNamara who has performed all the SCR testing. I would also like to acknowledge other JM staff who have performed XRF, ICP, and CHN tests. Finally, I would like to thank my colleague, Elliott Bruce, for the fruitful collaborations we have had over the years.

I am very grateful I had the opportunity to continue working with Magda Łozińska–Miller who first mentored me as an undergraduate in her role as post–doc in the PAW group. She has been a pillar of support and inspiration throughout my research career. I would

also like to thank fellow colleagues in the PAW group who have made it as seamless and fun as possible to continue working through some challenging pandemic years. The team at JMTC Chilton has also been very welcoming and they made the industrial placement periods in England a wonderful learning experience. I am very grateful for everyone's help there with using the lab facilities. Special thanks are owed to Vesi Georgieva and Raquel García who have both encouraged me throughout the PhD.

At last, I would like to express my gratitude for my family who have entertained and supported my dreams. My parents gave their everything so I can have the best opportunities and I wouldn't be at this point in my career without their encouragement. A special thanks has to go to my grandma who used to challenge me to do random math operations in my head, which helped me with on-the-fly calculations in the lab years later, and my grandpa who would track down all the best (and thickest) chemistry books for me, which meant that no textbook surprised me during my time at university. And finally, I am most grateful for my partner, Amaan, who has been there for every challenge and celebration along the way. His patience, kindness and amazing cooking skills helped me overcome any hurdle.

The School of Chemistry at University of St Andrews and Johnson Matthey Plc. are thanked for funding this work.

Research data underpinning this thesis are available at

https://doi.org/10.17630/7f7d6756-3c7c-4c47-94ed-0da7617a731b.

Chapter 3

Designed synthesis of STA-30: a small pore zeolite catalyst with topology type SWY

Disclaimer: This chapter is largely based on a published article in *Chemistry of Materials* (R. G. Chitac, J. Bradley, N. D. McNamara, A. Mayoral, A. Turrina and P. A. Wright, *Chemistry of Materials*, 2021, **33**, 5242–5256). The supporting information was incorporated into the main text of the article and the data from the MTO catalysis tests was also added into this chapter. Permission was granted by ACS Publications.

The synthesis was also reported in the patent application no. US20220333519A1, 2022 (STA-30, a new member of the SWY family of molecular sieves, methods of preparation and use – Inventors: Ruxandra Georgiana Chitac, Nicholas McNamara, Alessandro Turrina, Paul Anthony Wright) which has been published and it is pending examination.

Introduction

The discovery and development of new zeolitic aluminosilicates continues to add to the pool of potential adsorbents and catalysts for industrial processes. Among these, small pore materials (with pores of free diameters from 3 **–** 4 Å) have found widespread use and potential applications in air separation and carbon capture, and in the important catalytic processes of the conversion of methanol to light olefins (the MTO reaction) and the selective catalytic reduction (SCR) of NO emissions from diesel engines.[1,2]

For both reactions, materials with CHA topology are the most studied – SAPO-34 is the industry standard for MTO catalysis[3] (although activated aluminosilicate CHA, H-SSZ-13 also has good activity[4]) and Cu–exchanged zeolite SSZ-13 is the industry standard for NH_3–SCR of NO,[5,6] giving good conversion, selectivity and hydrothermal stability over a range of conditions. Nevertheless, other small pore zeolites also show commercial applicability (such as SSZ-39(AEI))[7,8] and, in general, zeolites with smaller pore sizes perform better than those with medium or large pores in the SCR reaction.[6,9] For example, SSZ-13 is a member of the ABC-6 family of zeolite structures. In this family, the frameworks are built from the stacking of layers of 6–membered rings (6Rs) parallel

to the *ab*–plane, connected by 4Rs along the *c*–direction. There are three different positions for these 6Rs, related through translation in the hexagonal *ab*–plane, centred at *x*, *y* coordinates of (0,0), (⅓,⅔) and (⅔,⅓) and denoted A, B and C. Each stacking sequence within this family can then be described using these letters. The CHA topology type, for example, has the AABBCC stacking sequence, giving rise to a single type of cage, the *cha* cage, connected to six others via 8–membered ring openings. The ABC-6 family exhibits many different materials: the 'Zeolite Atlas'[10] reports 25 materials discovered to date, either natural or synthetic, and new structures continue to be reported.[11] Li *et al.* analysed this structural family via a high–throughput computational study and concluded that there are at least 1150 energetically viable ABC-6 topologies that could be feasible targets for synthesis.[12]

The ABC-6 structure types can be prepared with different framework compositions, so that as well as aluminosilicate zeolites, many aluminophosphate (AlPO) zeotypes have been observed. For example, the silicoaluminophosphate (SAPO) analogue of chabazite, SAPO-34,[13] is widely used in the MTO reaction,[3] and has good activity as Cu-SAPO-34 in ammonia SCR of NO.[14] However, the (hydro)thermal stability at low temperatures of the Cu-SAPOs is lower than that of high silica Cu-zeolites under the conditions of SCR, where the required lifetimes are very long, and therefore aluminosilicates are the preferred catalysts for this reaction.[15] Nevertheless, structures observed as AlPOs (and SAPOs), if prepared as zeolites, can be of considerable catalytic interest.

Of the 25 reported zeotypes of the ABC-6 family, 11 have been prepared as both aluminosilicates and AlPOs (SAPOs),[10] which indicates the feasibility of compositional 'crossover' and demonstrates that ABC-6 structures known to occur as AlPOs can be candidates for synthesis as zeolites. Further, seven ABC-6 topology types were prepared for the first time as AlPOs or SAPOs, and while two of these have subsequently been synthesised as aluminosilicates, AFX – SAPO-56 and later SSZ-16,[16,17] and recently AFT – AlPO-52 and then SSZ-112 (highly faulted),[18,19] the remainder (AFV, AVE, AVL, SAT, SWY) are attractive targets. The topology type SWY, recently prepared as SAPO STA-20,[20] is one of these. The SWY structure has the 12–layer stacking sequence AABAABAACAAC and contains parallel columns of *can* cages and *d6r*s and of *gme* and larger *swy* cages, with the latter two types of cages connected via 8R windows. It is therefore closely related to the ERI and OFF structures (also ABC-6 structures, with stacking sequences AABAAC and AAB) and all are based on structural units of columns

of alternating *d6r*s and *can* cages (Figure 3.1). The difference lies in the orientation of the *can* cages and as a result the types of larger cages (ERI – *eri*; OFF – *gme*) or channels (OFF) that are present. Hence, we thought that a zeolite with this structure would be a good candidate for catalytic testing and so it offered an excellent target for designed synthesis.

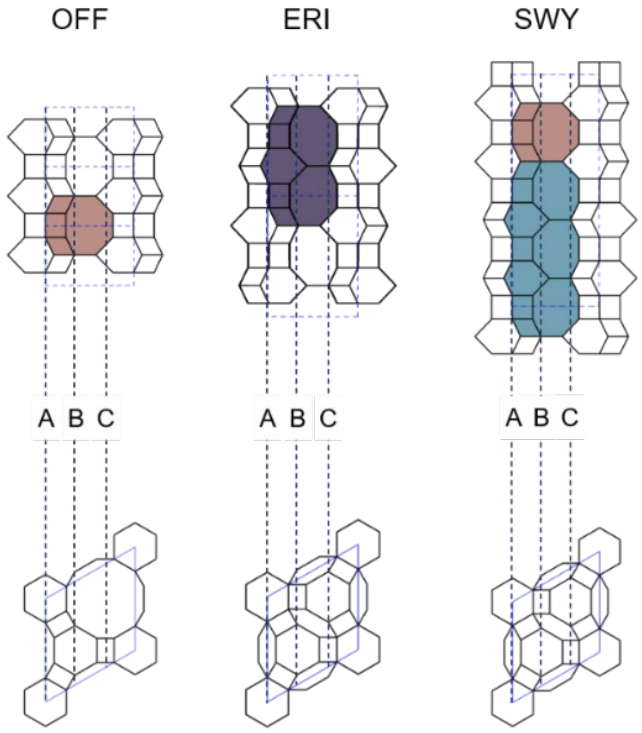

Figure 3.1 The layer stacking sequence and specific cages in the OFF, ERI and SWY frameworks (*gme* cage – light brown, *eri* cage – purple, *swy* cage – blue).

The designed synthesis of zeolites and zeotypes has achieved some notable successes in recent years, usually through the design of OSDAs that are a close fit to cages within the framework. It has been established that alkylammonium and other organic cations can be highly selective templates for zeolites during their hydrothermal crystallisation, and that it is possible to analyse and model potential new frameworks and assess their synthetic viability.[21–24] Therefore, a number of groups have adopted computational methodology to design a template for a framework of given structure and composition and then to prepare it. Examples include the synthesis of STA-18, topology type SFW, previously prepared highly faulted as the aluminosilicate SSZ-52 but realised as a SAPO by a retrosynthetic approach using modelling,[25] and the aluminosilicate ITQ-47, isostructural with the mineral *boggsite* and prepared via a phosphazene template.[26] Schmidt *et al.* were able to prepare a pure silica STW for the first time by template

design[27] and Shi *et al.* reported modelling studies to develop new templates for the same structure.[28] Furthermore, X. Hong et al.[29] were able to prepare an aluminosilicate with the IWR topology, which had previously been directly prepared only as the germanosilicate ITQ-24 or borosilicate or pure silica versions,[30,31] via computational assessment of candidate pyrrolidine–based OSDAs. Recently, Jo and S. B. Hong have reported a designed template synthesis of a zeolite with a previously unrealised topology type that had been predicted by consideration of hypothetical variants of the brewsterite zeolite structure.[32]

Whereas in SAPOs the use of organic templates is sufficient to guide the synthesis, in aluminosilicate syntheses there is a greater variability in gel compositions and inorganic cations (and anions, in fluoride syntheses). Therefore, the effect of these inorganic parameters is also important, and the metal cations contribute to determining which structure crystallises.[33] For example, Hong *et al.* made use of the effects of Sr^{2+} and Ba^{2+} cations in addition to those of Na^{+} and tetraethylammonium ions to guide syntheses within the extended RHO series of zeolites.[34,35]

Here, the designed synthesis of the aluminosilicate form of SWY is reported, using a combination of computational analysis of template–framework interactions and careful control of the parameters of the gel composition and the hydrothermal synthesis. The successful synthesis has been confirmed by advanced characterisation techniques and the catalytic performance of the stable activated form was investigated in the MTO reaction and also, once Cu–exchanged, in the ammonia SCR of NO.

Experimental

Synthesis

STA-30 type materials were prepared in stainless steel autoclaves with Teflon liners. First of all, the Al source – aluminium isopropoxide or aluminium hydroxide (>76.5%, Alfa Aesar) was dissolved in a solution of tetrapropylammonium hydroxide. Ludox HS-40 was added, and the mixture allowed to homogenise for at least 1.5 h. If the synthesis was carried out in large liners (>50 mL), then the isopropyl alcohol formed was allowed to evaporate by heating the gel (confirmed by monitoring weight loss) and the water content was adjusted to maintain the desired H_2O/SiO_2 ratio in the gel. The gel was aged for 20 h at 368 K. Aqueous solutions of 1,*n*-(diazabicyclo[2.2.2]octane)alkyl bromide (diDABCO-C*n*)Br_2 (*n* = 6-10, for *n* = 7, 9, 10, synthesis provided in the Appendix Chapter 3) and potassium hydroxide were prepared and added to the aged gel dropwise. The

resulting mixture was stirred at RT for a further 2 h, after which the autoclaves were rotated at 60 rpm and heated at 393 – 413 K for 5 days. At the 1.5 L scale, the rotation of the autoclave was replaced by mechanical stirring at 300 rpm using a double pitched blade type of impeller. The product was recovered by centrifugation and washed with deionised water. A typical gel composition was: 1.0 SiO_2: 0.05 Al_2O_3: 0.10 KOH: 0.12 (diDABCO-C8)Br_2: 0.4 TPAOH: 20 H_2O. The amount of Al source, KOH, H_2O and (diDABCO-C8)Br_2 could be varied to some extent without affecting the purity of the product.

A sample of aluminosilicate ERI zeolite was synthesised and activated. This was used as a benchmark comparison for STA-30 since they share many structural similarities, as has been mentioned. The aluminosilicate ERI synthesised possessed similar Si/Al (6.1) and crystallite morphology (rice grain) to those of the STA-30 materials described below. The gel composition used for its synthesis was 1.0 SiO_2: 0.04 Al_2O_3: 0.13 KOH: 0.10 1,4-dibromobutane : 0.21 1-methylpyrrolidine : 0.5 TPAOH: 19 H_2O. Al isopropoxide and Ludox HS-40 were the Al and Si sources, respectively. The gel was treated as described above for STA-30, with the only difference being that 1,4-dibromobutane and 1-methylpyrrolidine were added directly into the gel. The crystallisation took place at 423 K in autoclaves rotated at 60 rpm for 5 days. More details about this synthesis and other ERI syntheses will be discussed in Chapter 5.

Preparation of Cu exchanged samples for NH_3–SCR of NO

These additional post-synthetic modifications to the STA-30 and aluminosilicate ERI zeolites, and the subsequent testing were carried out by Nicholas McNamara, at Johnson Matthey in Wayne, USA.

To prepare the material as a Cu catalyst for SCR, activated forms of STA-30 with two different Si/Al ratios were slurried with copper (II) acetate monohydrate (Shepherd) dissolved in de–mineralised water at 313 K for 4 h, to give a Cu loading of 3.33 wt%. The slurried samples were then dried in a static oven at 353 K for at least 16 h. The Cu–containing STA-30 samples were then calcined in air at 823 K for 4 h. The samples were then pelletized and loaded into an SCR test rig. A gas mixture consisting of 500 ppm NO, 14% O_2, 4.6% H_2O, 5% CO_2 and a balance of N_2 was passed over the catalyst at a space velocity of 90 h^{-1}. The samples were heated to 423 K in this gas mixture and when 423 K was reached, NH_3 was added into the gas mixture at 500 ppm and the samples were held for 30 minutes isothermally to equilibrate. The temperature was then increased from

423 to 773 K at 5 K min^{-1} while the outlet gas composition was monitored by FTIR. The samples were also aged at 1023 K, for 80 hours under flowing air that contained 10% H_2O to test the performance of aged samples.

Operando MTO study

This study was carried out by Inez Lezcano–Gonzalez at UCL.

The reaction was performed in a commercially available CCR1000 stage by Linkam Scientific in which the temperature of the catalyst can be controlled. The activated forms of the zeolites under investigation (50 mg) were activated at 823 K (5 K min^{-1}) under a flow of O_2 for 1 hour. He gas was flushed through the system to remove all O_2, and the catalyst cooled to 623 K. The reaction was then performed using He as a carrier gas at a flow of 30 mL min^{-1}, with methanol injected into the system by use of a HPLC pump set to 1.7 µl min^{-1} corresponding to a WHSV of 1.6 h^{-1}. The cell outlet is carried to a Pfeiffer OmniStar MS to analyse the reaction products. UV–Vis spectra were measured on a Flame-S-XR1-ES Ocean Optics spectrometer throughout the course of the reaction, initially every 20 s and later every 5–15 min, using 900 ms integration time and 20 accumulations. The Kubelka–Munk equation was applied to convert reflectance measurements to absorbance values in all cases.

Results and discussion

Synthesis design

The SWY topology type described in the Introduction was prepared for the first time as the silicoaluminophosphate, SAPO STA-20, using diDABCO-$C6^{2+}$ and trimethylamine (TrMA) as organic structure directing agents. In that case, diDABCO-$C6^{2+}$ was found to occupy the *swy* cages, along with TrMA, while additional TrMA acted as a template for the *gme* cages.[20] DiDABCO–type dicationic molecules therefore provided a promising starting point in the design of potential templates for the *swy* cage in an aluminosilicate SWY. However, the trimethylamine is likely to be neutral at the high pH used in the zeolite synthesis.

The potential suitability of a series of diDABCO-Cn^{2+} molecules of different lengths (n = 6–10) as templates for the *swy* cage in a SWY framework with composition SiO_2 was assessed through molecular dynamics calculations. The minimum energy location of the molecules of the different diDABCO-Cn^{2+} templates is shown in Figure 3.2 and the calculated energies of overall stabilisation are listed in Table 3.1. Even though the unit

cell parameters were allowed to vary during the energy minimisations, they did not deviate significantly (<0.1 Å, <0.1°) for structures with different OSDAs included (Figure 3.3). The diDABCO-C8^{2+} molecule was observed to be a better fit than diDABCO-C6^{2+} (~14.1 Å) inside the *swy* cage cage (~22.7 Å) – the STA-20 SAPO prepared with the C6 variant also occludes a TrMA molecule. Even though the length of diDABCO-C7^{2+} seemed more appropriate, it was diDABCO-C8^{2+} that conferred the strongest binding energy to the optimised structure (Table 3.1). Longer molecules in this family incurred energy costs from higher torsion energies (OSDA molecules in their ground state conformation are shown in Figure 3.2 – Bottom). The binding energies derived from these calculations also show that OSDAs with an odd number of C atoms in the alkyl chains perform less well than those with an even number of C atoms. This appears to be due to the relative orientation of the DABCO end groups and the ends of the *swy* cage, and the resulting interactions between the end groups and the framework. Therefore, this modelling led to the choice of diDABCO-C8^{2+} as the best candidate template.

Table 3.1 Results of molecular dynamics calculations on an ideal SWY silica framework, with molecules of diDABCO-C*n*$^{2+}$ fitted inside both *swy* cages of a unit cell.

n	Binding energy (kJ mol^{-1})	ΔTorsion energy OSDA (kJ mol^{-1})
6	-1643	0.4
7	-1616	0.4
8	-1670	3.8
9	-1641	4.6
10	-1642	9.6

Beyond the choice of the OSDA, the synthetic conditions for targeting SWY were inspired by the gel composition (1.0 SiO_2: 0.05 Al_2O_3: 0.09 KOH: 0.10 RBr_2: 0.4 TPAOH: 16 H_2O) and conditions presented by Zhu *et al.* for the crystallisation of UZM-12, an aluminosilicate with the related ERI framework.[36] Both SWY and ERI frameworks belong to the ABC-6 family and have many building units in common, including the *can* cages, which are templated by K^+ cations. While in the work previously mentioned on UZM-12, the largest cage – *eri*, is templated by hexamethonium (HM^{2+}) molecules, this was replaced by the diDABCO-C8^{2+} molecule designed as a template for the *swy* cage, as described above.

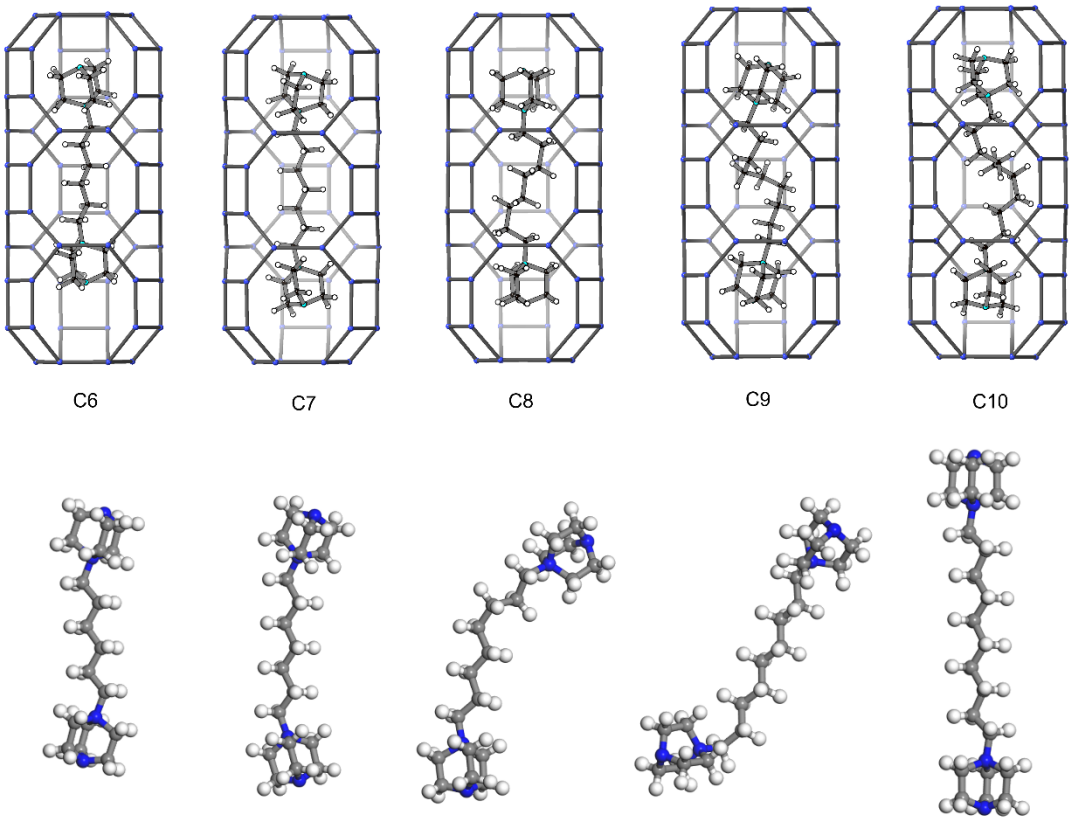

Figure 3.2 (Top) The fit of diDABCO-Cn^{2+} (n = 6 – 10) templates in the silicate SWY framework, modelled using molecular dynamic calculations. (Bottom) OSDA molecules in ground state, geometry determined through molecular dynamics (MD) calculations and geometry optimisation.

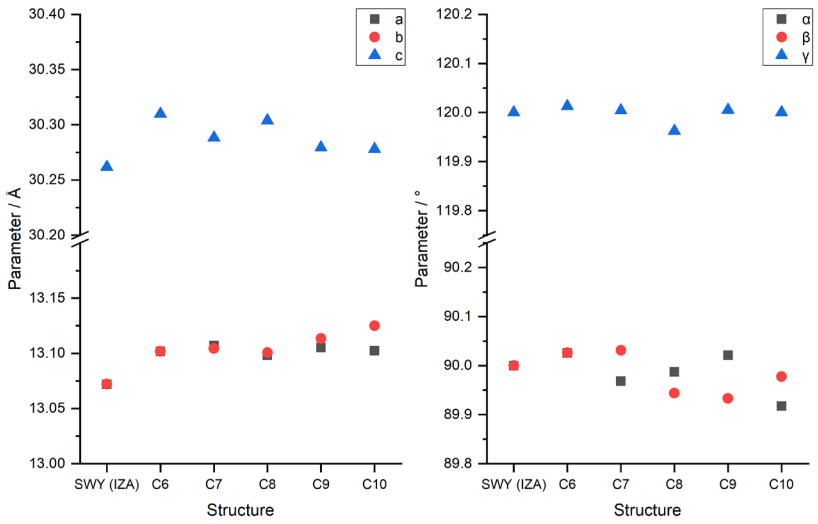

Figure 3.3 Variation of cell parameters in the optimised unit cells of the structures studied as part of the computational modelling carried out on the silicate SWY framework loaded with various diDABCO-C*n* templates (2 molecules / unit cell).

The synthesis of UZM-12 was achieved through a charge–density mismatch (CDM) approach in which a tetraalkylammonium hydroxide solution, together with Al and Si sources were aged at 368 K for 20 h. After the aging step, KOH and RBr_2 were also added to the gel. The same sequence of steps was followed for the designed synthesis targeting aluminosilicate SWY. Thus, the approach followed for the synthesis of aluminosilicate SWY can also be described as the CDM approach. The relevance of the steps in the gel preparation will be discussed in Chapter 4.

Syntheses were performed between 393 K and 423 K, using 50 mL autoclaves, with tumbling. The gel composition was close to that of Sample 1 in Table 3.2. Notably, crystallisation at the higher temperature of 423 K resulted in a ZSM-5 impurity, which can be attributed to the presence of the TPA^+ cations added here as mineralising agents in the first step of gel formation.[37] Otherwise, the same material appeared to have been formed between 393 – 413 K (SEM images PXRD patterns in Figure 3.4). The PXRD pattern of the product crystallised at 413 K was compared with the patterns simulated for the SWY framework (using the structure of as–prepared STA-20), as well as for zeolites erionite, offretite and their intergrowth, zeolite T (Figure 3.5). The preparation of the aluminosilicate erionite is provided in the Experimental section of this Chapter, and the syntheses of aluminosilicates offretite and zeolite T are provided in the Appendix Chapter 3. The patterns of these related materials are very similar, with many peaks in common, but there are peaks characteristic of the SWY structure because of the extended *c*–axis, including the (101) reflection at 8.3° 2θ. It immediately appeared that SWY-type aluminosilicate zeolites had been successfully prepared. The zeolite type was named STA-30 (St Andrews microporous material-30). Differences in intensity between the simulated pattern of STA-20 and the observed pattern of STA-30 are thought to arise mainly from their different extra–framework species, but additional proof was required that STA-30 was indeed a zeolite with the SWY topology (see below). For more context, usual differences between the simulated and measured XRD patterns of related zeolites discussed here can be found in Figure 3.5.

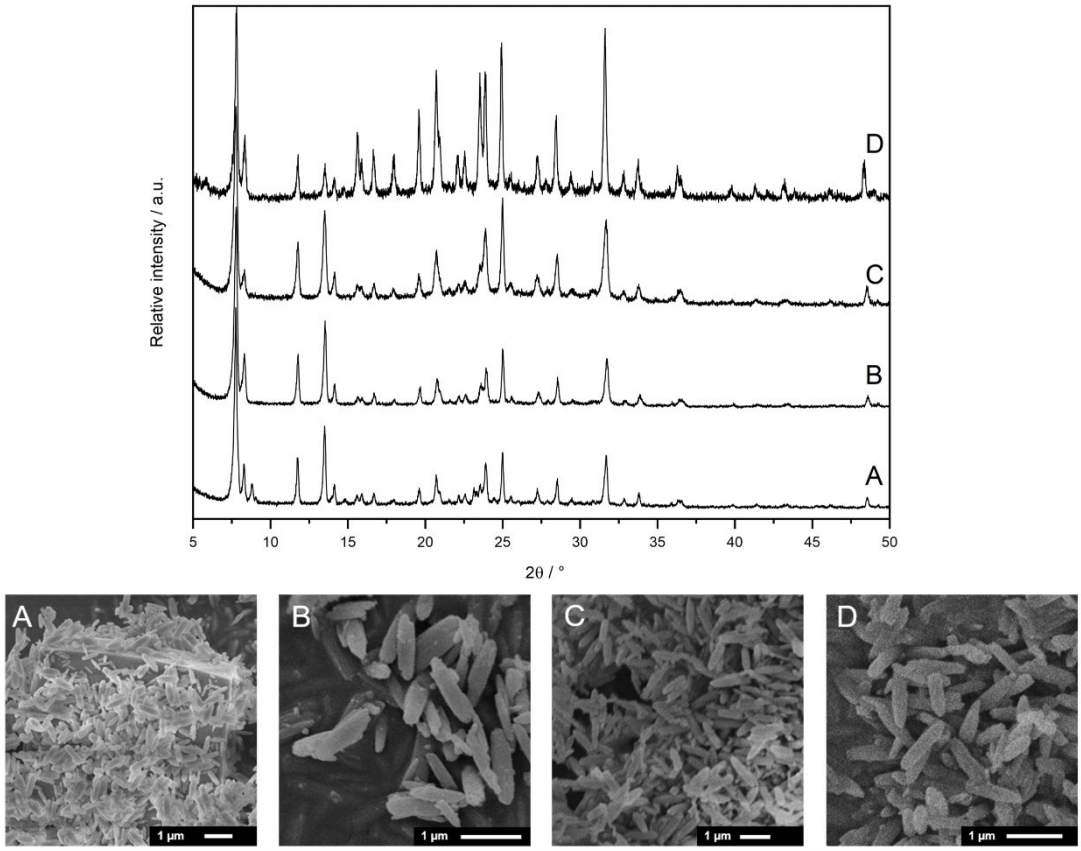

Figure 3.4 (Top) PXRD patterns of samples synthesised at temperatures from 423 K to 393 K for 5 days (in the order A–D), the XRD patterns of Samples A–C were collected from capillaries packed with calcined material, whereas the pattern of Sample D was collected from a capillary packed with as–prepared material. (Bottom) SEM images of samples synthesised at 423 K (A), 413 K (B), 403 K (C) and 393 K (D).

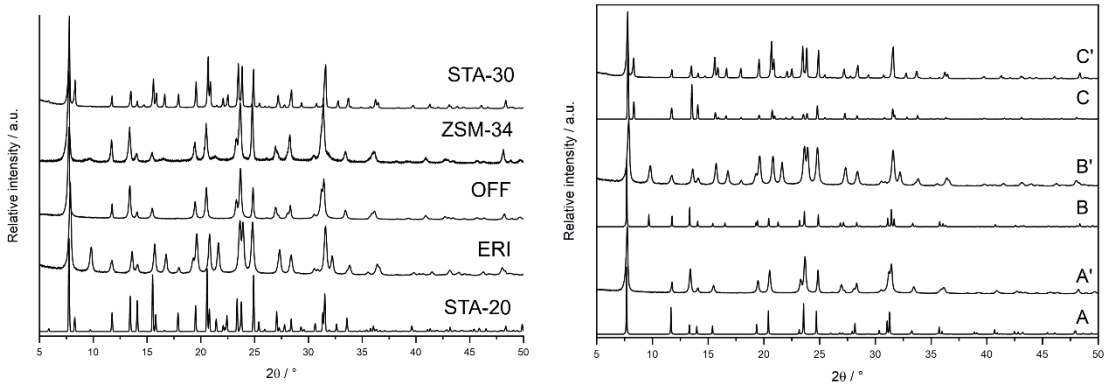

Figure 3.5 (Left) Comparison of the PXRD pattern of as–prepared STA-30 with the simulated pattern for SAPO STA-20[20] and observed PXRD patterns of other related zeolites in as–prepared form: erionite, offretite and ZSM-34. (Right) Comparison of simulated XRD patterns with those of as–prepared materials: A/A': erionite (ERI), B/B': offretite (OFF) and C/C': STA-30 (SWY).

The dependence of the crystallisation on the composition of the gel and other synthetic parameters was investigated taking 398 – 413 K as the preferred temperature range. Additionally, even though the synthesis can be carried out with other tetraalkylammonium solutions (PXRD patterns and SEM images in Figure 3.6), the 40% aqueous TPAOH solution was chosen as the preferred base for further testing.

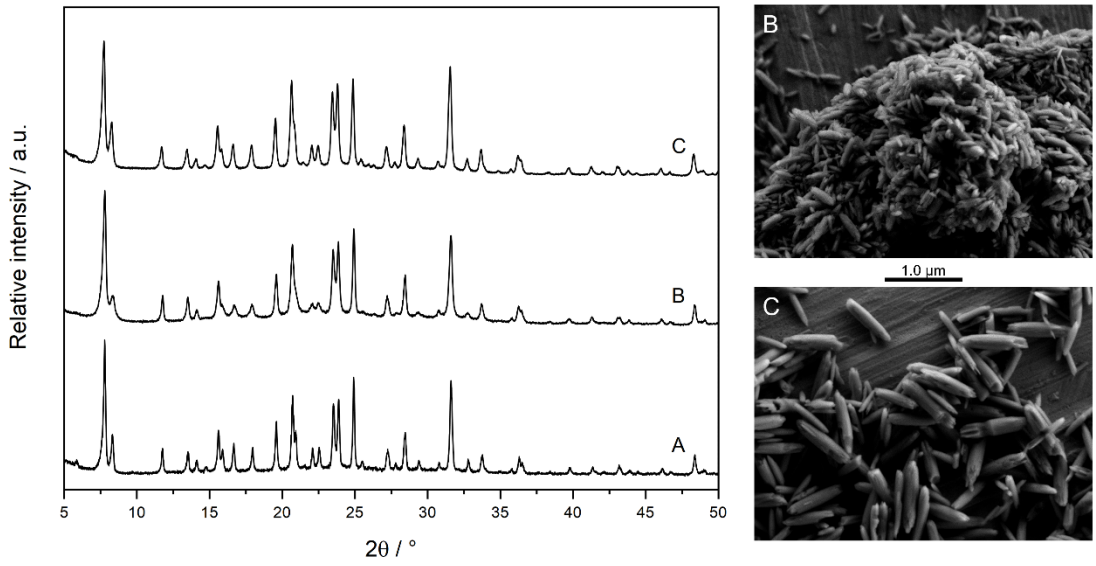

Figure 3.6 PXRD patterns of samples synthesised using various tetraalkylammonium hydroxide solutions as mineralisers: TPAOH (A), TEAOH (B) and TBAOH (C), along with SEM images of samples (B) and (C).

Most significantly, given its importance in determining hydrothermal stability, the Si/Al ratio of STA-30 could be increased from 5.8 to 7.1 (see Samples 1 and 2 in Table 3.2) by reducing the amount of Al added to the gel. Further reduction led to no product being formed after 5 days, when the synthesis was performed with Al(O-*i*-Pr)$_3$ in 50 mL tumbling autoclaves.

There is a lower limit to the K^+ content that enables crystallisation of STA-30 to occur (K/Si = 0.05, Sample 3, Table 3.2), even if the solution alkalinity was kept constant by the addition of more of the hydroxide (rather than the bromide) form of the diDABCO-C8^{2+}. The STA-30 products had ~0.7 K/Al (determined by EDS), which corresponds to a molar ratio of K/Si in the gel of about 0.05, indicating the K was taken up with high specificity. Changing the K^+ content had little effect on the particle morphology (Figure 3.7 – Top), in contrast to the effect observed previously for other materials from the ABC-6 family.[38,39]

Additionally, other diDABCO-Cn^{2+}, n = 7, 9 and 10, were used as OSDAs to test the predictions from the computational modelling. While STA-30 was still prepared in all cases, there were some notable differences between the XRD patterns of the products (Figure 3.8). The materials synthesised with shorter or longer molecules than diDABCO-C8^{2+} were less crystalline as indicated by worse signal–to–noise ratio and elevated background signal in the 20–30° *2θ* range of their PXRD patterns. This implies that these cations are less effective templates for the *swy* cage than diDABCO-C8^{2+}, in line with the computational data.

Scale up to 125 mL using Al(O-*i*-Pr)$_3$ was successful, giving a material with a lower Si/Al ratio when compared to a similar preparation on the 50 mL scale (Samples 2 and 5 in Table 3.2), without otherwise affecting the product (PXRDs in Figure 3.9). It was possible to lower the amount of Al(O-*i*-Pr)$_3$ in the gel to obtain a more silica–rich product (Sample 6,Table 3.2).

Since the method proved to be suitable for synthesis on larger scales, the suitability of Al(OH)$_3$ as the Al source was also investigated, because its use eliminates the need to remove the isopropyl alcohol evolved in the precursor gel formation. Furthermore, Al(O-*i*-Pr)$_3$ is an undesirable Al source commercially because of its high cost. The replacement of the Al(O-*i*-Pr)$_3$ was straightforward on the 125 mL scale (Sample 7,Table 3.2) as the TPAOH is a strong enough base to dissolve the reagent and enable successful crystallisation. However, the use of the hydroxide led to lower yields compared to the syntheses carried out with Al(O-*i*-Pr)$_3$. Notably, the Si/Al ratio of the product synthesised with Al(OH)$_3$ was higher than one synthesised with an equivalent amount of Al in the form of Al(O-*i*-Pr)$_3$ (Samples 7 and 5,Table 3.2). This proved that Al(OH)$_3$ is a viable Al source in this preparation of STA-30, which is further enforced by the successful scale up to a 1.5 L scale without any effect on the Si/Al ratio of the product (Sample 8,Table 3.2) compared to that observed in the case of Al(O-*i*-Pr)$_3$. Despite the compositional and synthetic differences between the samples discussed in this paragraph, the morphology and size of the crystals of STA-30 were similar to those shown in Figure 3.7A (~1 μm long rice grain shaped crystallites). Additionally, taking these various optimisations into account, it was possible to synthesise higher Si/Al ratio materials (Si/Al ratio of 7.3, Sample 10 in Table 3.2), which shows the potential of this method to produce zeolites with controlled chemical compositions.

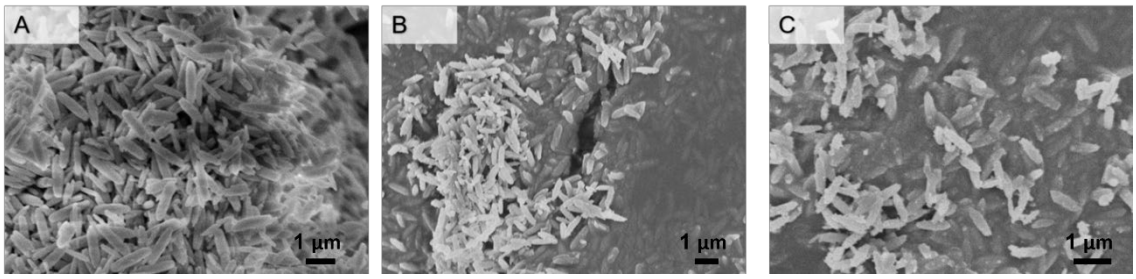

Figure 3.7 SEM images of samples made with x = 0.12 (A), 0.07 (B) and 0.06 (C), where x is the molar ratio in the gel composition 0.04 Al_2O_3 : 1.0 SiO_2 : 0.12 (diDABCO_C8)Br_2 : x KOH : 0.4 TPAOH : 20 H_2O.

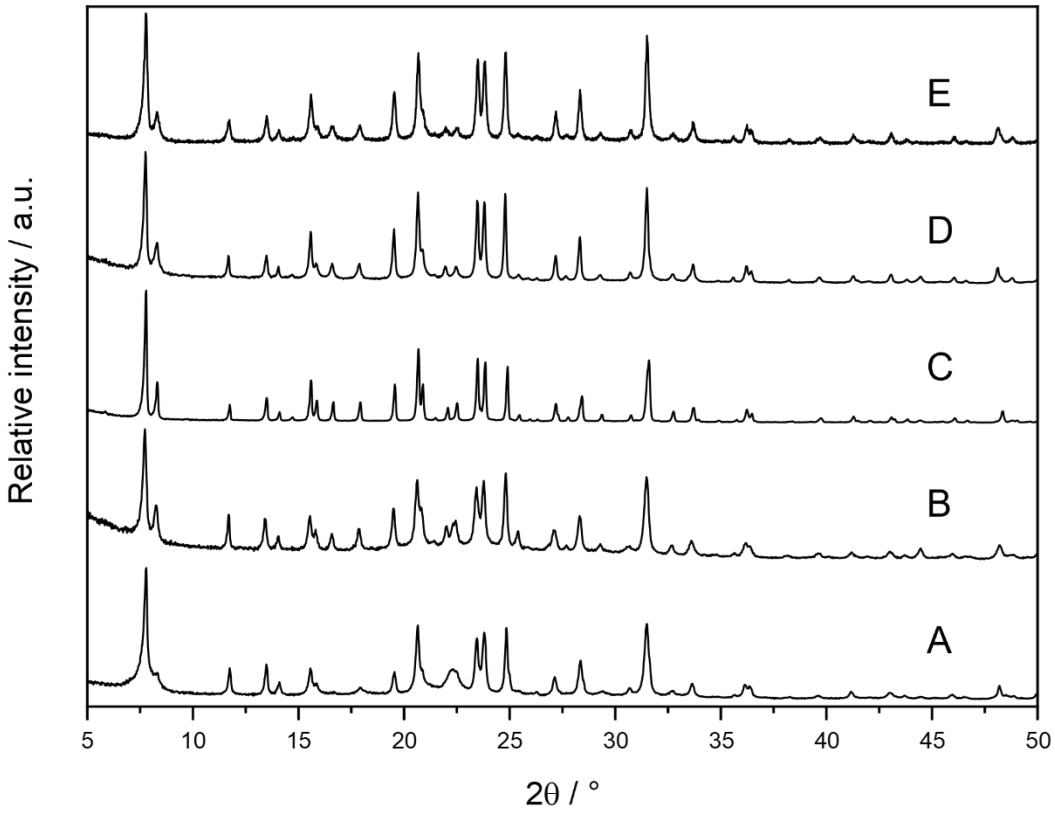

Figure 3.8 PXRD patterns of samples prepared with similar gel compositions and crystallisation temperatures, but with different OSDAs – diDABCO-$C6^{2+}$ (A), -$C7^{2+}$ (B), -$C8^{2+}$ (C), -$C9^{2+}$ (D) and -$C10^{2+}$ (E).

Table 3.2 Selection of syntheses related to the preparation of STA-30.

Sample	Al source	Molar ratio to SiO_2 in the gel[a]				Scale (mL)	Product Si/Al
		Al_2O_3	KOH	(diDABCO-C8)Br_2	H_2O		
1	Al(O-*i*-Pr)$_3$	0.05	0.10	0.12	20	50	5.8
2	Al(O-*i*-Pr)$_3$	0.04	0.10	0.12	20	50	7.1
3	Al(O-*i*-Pr)$_3$	0.04	0.05	0.13	20	50	6.7
4	Al(O-*i*-Pr)$_3$	0.04	0.08	0.10	20	125	5.5
5	Al(O-*i*-Pr)$_3$	0.04	0.12	0.13	20	125	5.8
6	Al(O-*i*-Pr)$_3$	0.03	0.12	0.13	20	125	6.8
7	$Al(OH)_3$	0.04	0.08	0.13	24	125	7.1
8	$Al(OH)_3$	0.04	0.08	0.13	20	1500	7.0
9	$Al(OH)_3$	0.03	0.12	0.13	20	125	6.3
10	$Al(OH)_3$	0.04	0.06	0.09	20	50	7.3

[a] All molar quantities as ratio to 1.0 SiO_2. The TPAOH/SiO_2 molar ratio for all samples was 0.4.

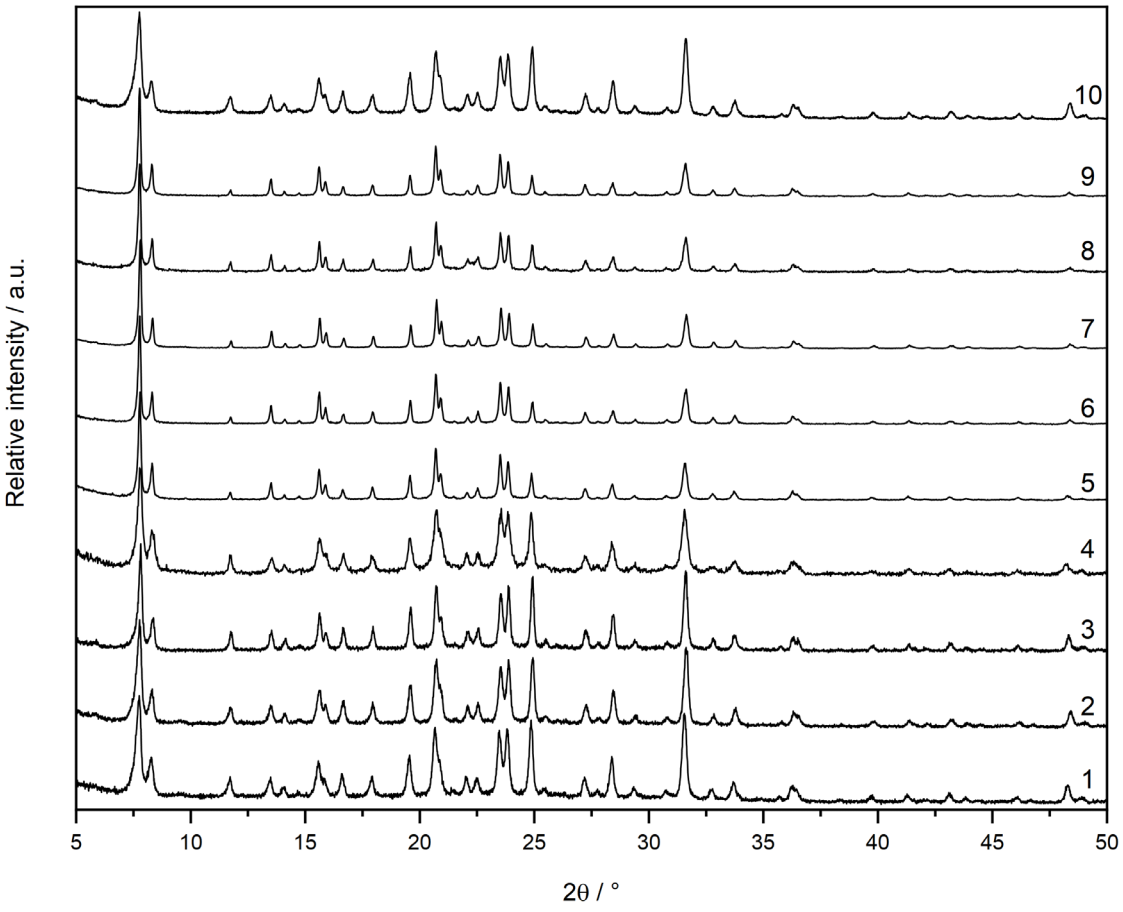

Figure 3.9 A comparison between the PXRD patterns of the as–prepared materials described in Table 3.2 – the patterns of samples 1–3 and 10 were collected from capillaries, whereas the patterns of samples 4–9 were collected from flat plates.

Crystallisation kinetics

A study of the crystallisation kinetics was carried out on one of the batches prepared on large scale (1500 mL) since small amounts of the gel could be sampled during the reaction in such reactors. The gel composition tested was similar to the one mentioned above for Sample 8.

The collection of PXRD patterns in Figure 3.10 show that STA-30 begins to crystallise after 3 days and is complete by 5 days (SEM images show crystals after 72 h – Figure 3.11). This correlates with the higher amount of solid recovered up to 72 h and the fact that those solids had higher Si/Al according to XRF as shown by Figure 3.11 and Figure 3.12. The phase formed before 3 days was largely amorphous, with a higher Si/Al showing preferential incorporation of Si over Al in the nucleation stage. The crystallisation occurs through the dissolution of this silica rich phase and the release of

Si and Al back into the mother liquor as evidenced by ICP (Appendix Figure 3.1). The K^+ levels in the recovered solids varied throughout the synthesis, but the K/Al value levelled when the crystallisation was complete.

This amorphous phase contained both diDABCO-C8^{2+} and TPA$^+$ according to ^{13}C CP MAS NMR spectra measured on the solids recovered during the study (Figure 3.13). While TPA$^+$ is not templating the STA-30 crystals, it is clear that it plays a role in the nucleation stages. Additionally, there is a splitting occurring in the peaks related to the DABCO end-groups of the OSDA after 4 days which is noticed in all STA-30 zeolites described in this chapter that have been analysed by ^{13}C NMR spectroscopy. This will be discussed later and also in the next chapter in more detail. The Al and Si environments in all solids are in the range expected for tetrahedral zeolitic environments, but they are broad in the early stages of the crystallisation, indicating an increased amount of disorder. The peaks become sharper and the environments are better defined after 5 days.

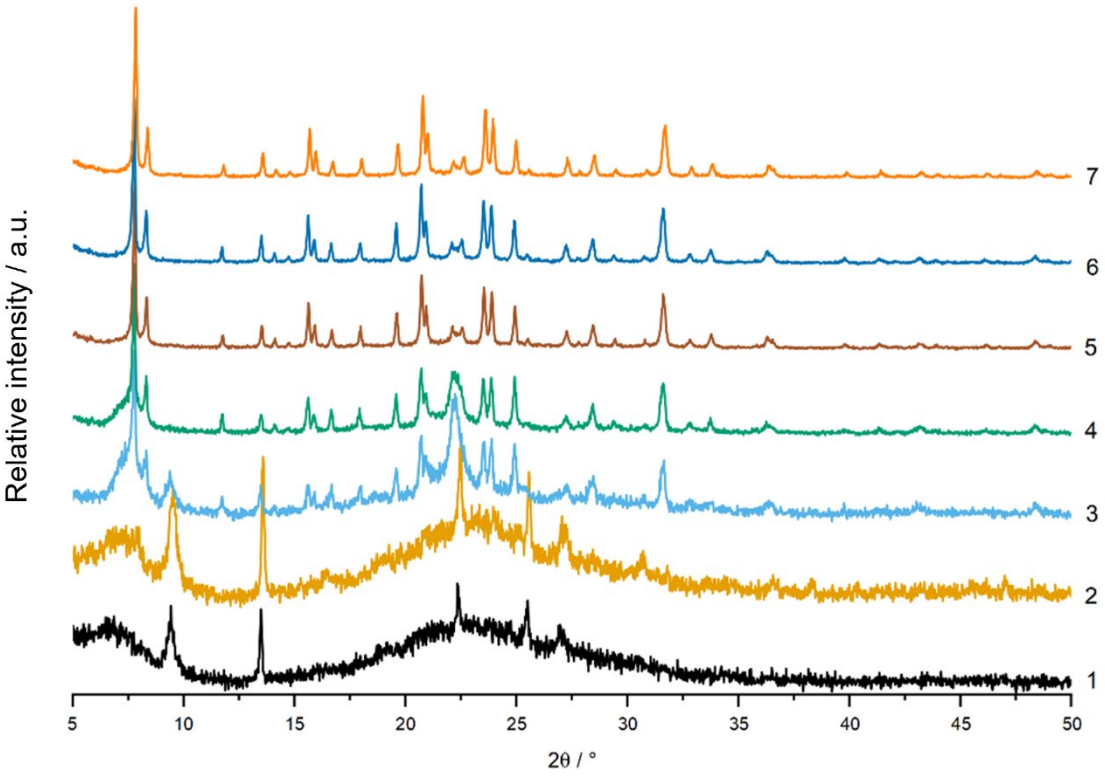

Figure 3.10 PXRD patterns of solids recovered from a CDM type synthesis, carried out as a batch preparation on a 1500 mL scale, with sampling every 24 hours.

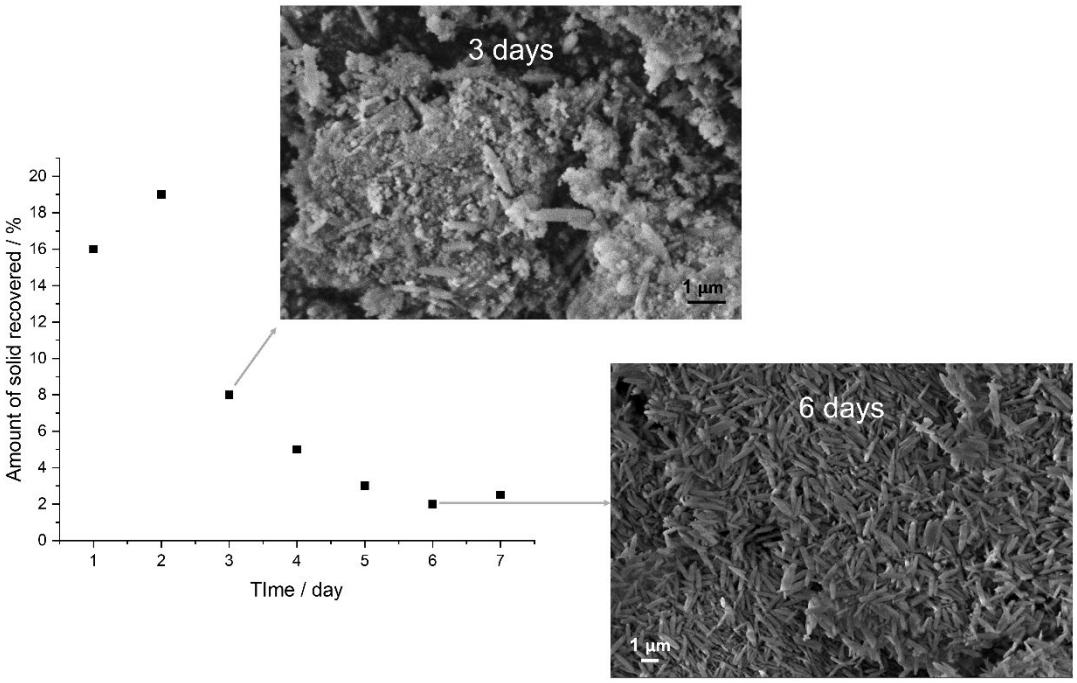

Figure 3.11 Amount of solid recovered from the samples collected throughout the crystallisation kinetics study expressed as percentage from the total mass discharged. (Overlapped) SEM images of the solids recovered after 3 days and 6 days of heating.

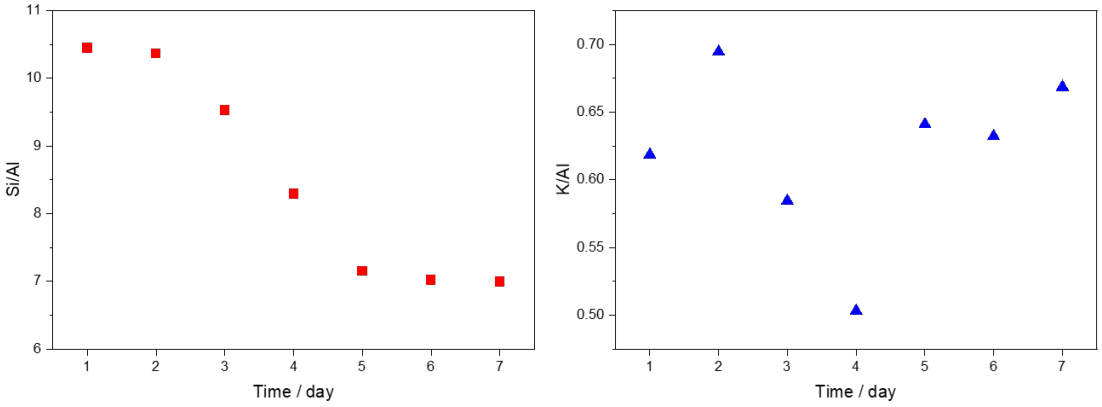

Figure 3.12 Evolution of Si/Al ratio (left) and K/Al ratio (right) in the solid products recovered from the crystallisation kinetics study.

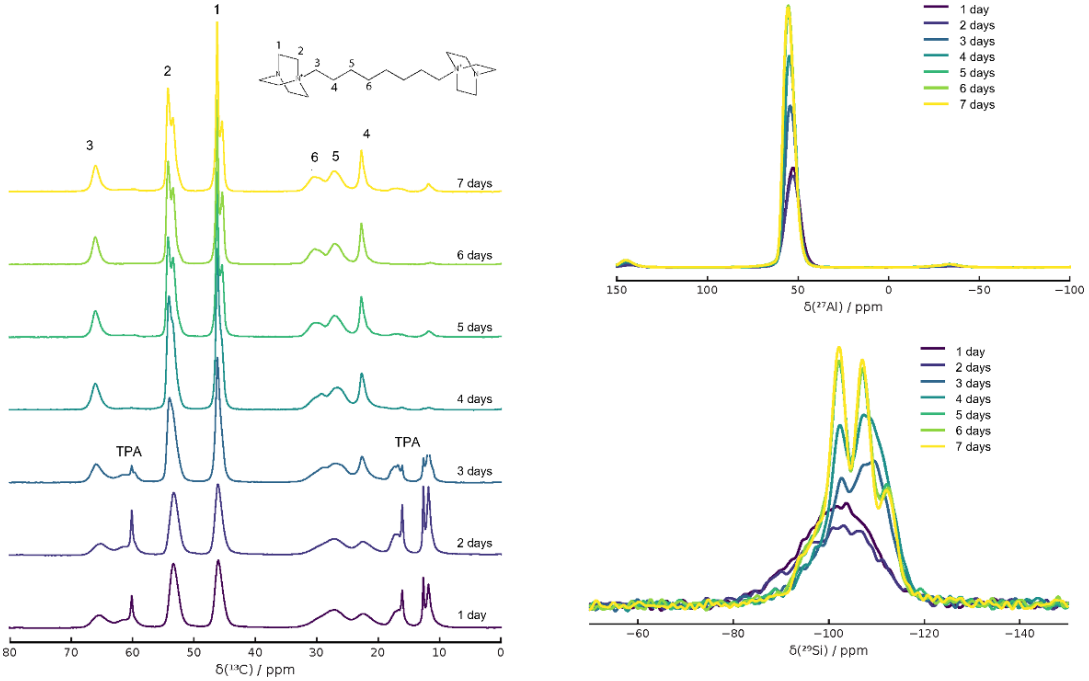

Figure 3.13 ^{13}C CP (left), ^{27}Al (top right), and ^{29}Si (bottom right) solid–state MAS NMR spectra collected from the solids recovered during the crystallisation study. (Figure adapted from internal an internal JM report by Jonathan Bradley, re–used with permission).

Analysis and post–synthetic modification of as–prepared STA-30

The ^{13}C, ^{29}Si and ^{27}Al MAS NMR spectra of as–prepared STA-30 (Si/Al = 7.0) are shown in Figure 3.14. ^{13}C CP MAS NMR spectra show that the diDABCO-C8^{2+} molecule is included intact while no significant amount of TPA$^+$ is present. The small peak at 11 ppm might indicate that the bulk sample contained trace amounts of TPA$^+$ (the other peaks expected around 16 ppm and 60 ppm were not observed) but the low concentrations ruled out TPA$^+$ as a template. Hence, diDABCO-C8^{2+} acts as the template while the TPAOH added in the first step of the preparation acts only as a mineraliser. The assignment of peaks in the ^{13}C spectrum was based on 2D NMR spectroscopy experiments carried out on (diDABCO-C8)Br_2 in a D_2O solution (Appendix Figure 3.2). The splitting of the resonances of C atoms in the DABCO units (at 46 ppm and 54 ppm) indicates that the end groups on the diDABCO-C8^{2+} are not in equivalent chemical environments within the framework. This splitting is not observed in the ^{13}C NMR spectrum of the molecule in solution (Appendix Figure 3.2). The other spectra confirm the identity of the material as an aluminosilicate zeolite through the characteristic shifts for $Si(OSi)_n(OAl)_{4-n}$ environments in the ^{29}Si MAS NMR spectrum and the characteristic peak due to tetrahedrally coordinated Al in the ^{27}Al MAS NMR spectrum. Deconvolution

of the ^{29}Si MAS NMR spectrum and use of Löwenstein's rule to calculate the Si/Al ratio of the material leads to a value much smaller (3.0) than the one determined by EDS or XRF (7.0), which has been previously observed for related frameworks, such as OFF, where the chemical shift of ^{29}Si in crystallographically distinct T–sites is significantly different.[40] Further investigation into the appropriate method for deconvoluting the ^{29}Si peaks was carried out on the activated material, as described later.

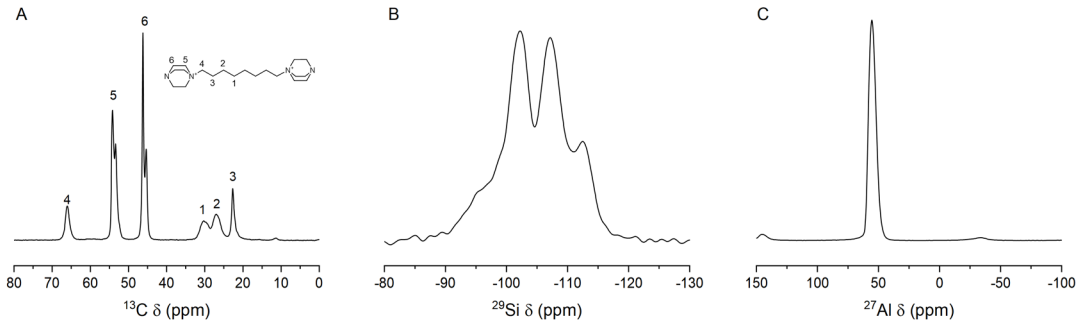

Figure 3.14 Solid–state MAS NMR data from an as–prepared STA-30 sample: ^{13}C CP (A), ^{29}Si (B) and ^{27}Al NMR spectra (C).

To prepare porous forms of STA-30, the organic template was removed by calcination under the following conditions: 823 K /12 h in air, on the basis of the TGA (Figure 3.15) to remove all organic matter. The weight loss in the TGA curve is deconvoluted in the next chapter.

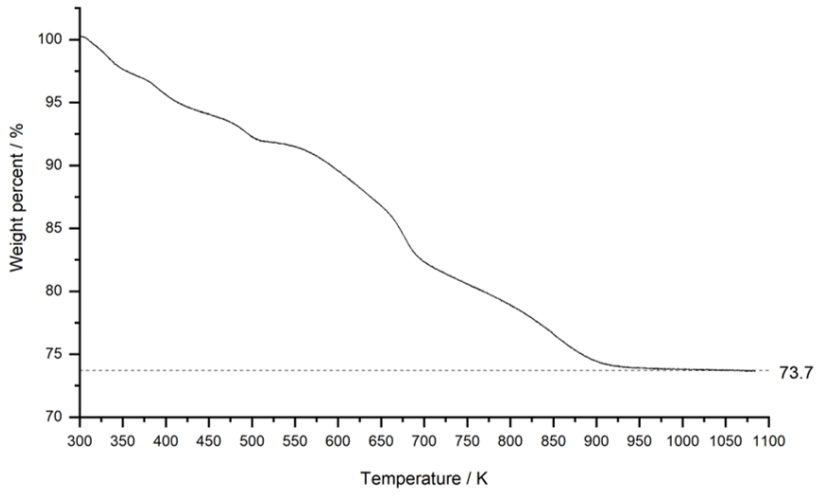

Figure 3.15 Weight loss of an STA-30 sample heated from RT to 1073 K.

The calcined samples were ion–exchanged with the 0.1 M NH_4Cl solution in a 100 mL g^{-1} ratio at room temperature (RT) to remove extra–framework cations. During the first

ion exchange, solid was collected after 1, 2 and 3 h, filtered and washed with deionised water, and analysed by EDS. As it can be seen in Figure 3.16, the equilibrium was reached after 1 h of stirring at RT. After 3 h, the remaining sample was completely washed and dried. This sample was then exchanged twice more by stirring the zeolite in fresh batches of NH_4Cl solution. The EDS analysis of these samples show that subsequent ion exchanges have little effect on the K^+ content. These samples were then split into two batches, each batch being subjected to a further two ion exchanges carried out at 333 K and 363 K. The two graphs at the bottom of the figure below show that neither temperature had any significant effect on the K^+ content meaning that the remaining K^+ cations in the framework cannot be removed through this procedure, regardless of the Si/Al ratio of the material. Thus, through this type of ion–exchange, the K^+ content of the zeolite could be reduced from ~0.7 K/Al ratio to ~0.3 K/Al. Subsequently, the exchanged sample was deammoniated to the 'activated' form.

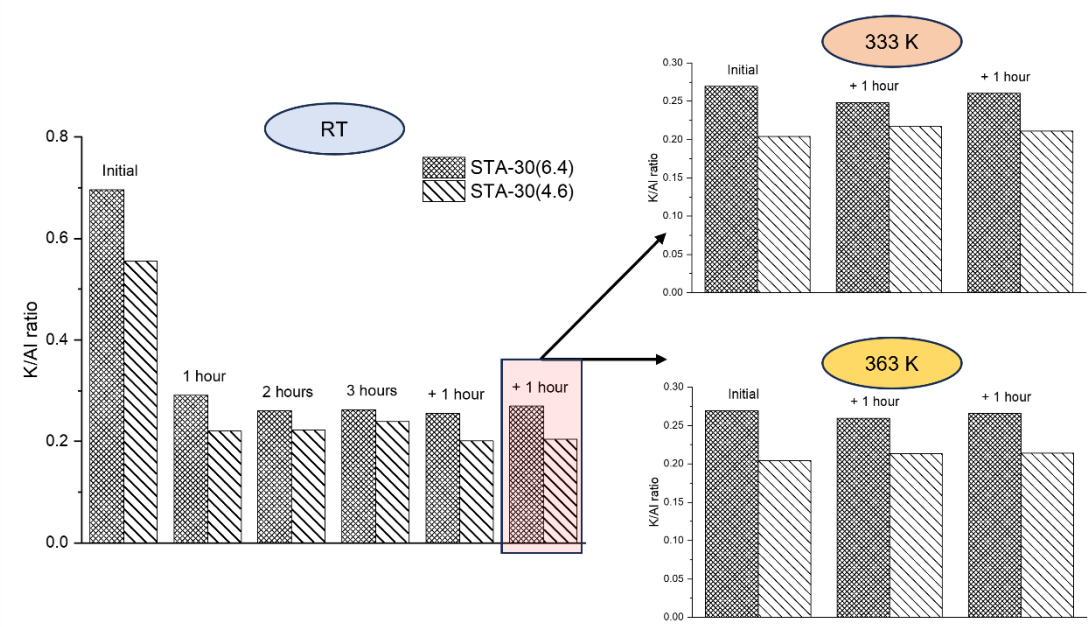

Figure 3.16 Plots showing the K/Al ratio throughout ion exchange of two calcined STA-30 samples of different Si/Al ratios with a solution of 1 M NH_4Cl at various temperatures.

Figure 3.17 shows that there are some changes in intensity of the peaks between the PXRD patterns of the as–prepared, calcined, and activated materials, which is to be expected due to the variation in the guest species in the cavities and pores of the zeolite. Nevertheless, there is no loss in crystallinity, indicating that the H,K-form of STA-30 is thermally stable.

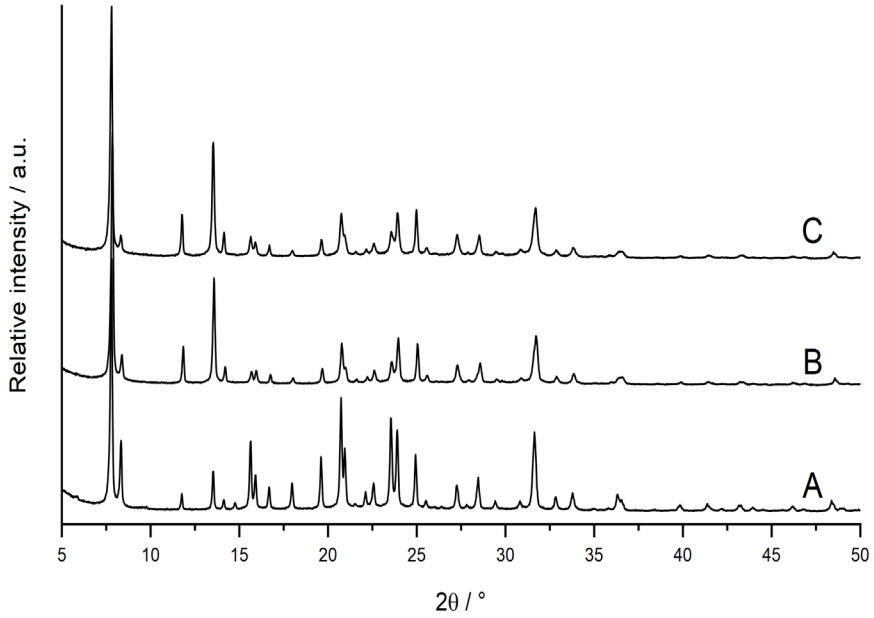

Figure 3.17 PXRD patterns of as–prepared (A), calcined (B) and activated (C) STA-30.

Crystal structure of STA-30

The crystal structures of the calcined and activated forms, both dehydrated, were determined by Rietveld refinement, using as a starting model an energy–minimised all–silica form of the SWY framework, in space group $P6_3/mmc$. K^+ cation locations and fractional occupancies were refined, to give good final fits to the observed patterns (Figure 3.18). Details of the refinements are given in Table 3.3 and representations of the framework and cation sites shown in Figure 3.19. Structural parameters can be found in Appendix Table 3.1.

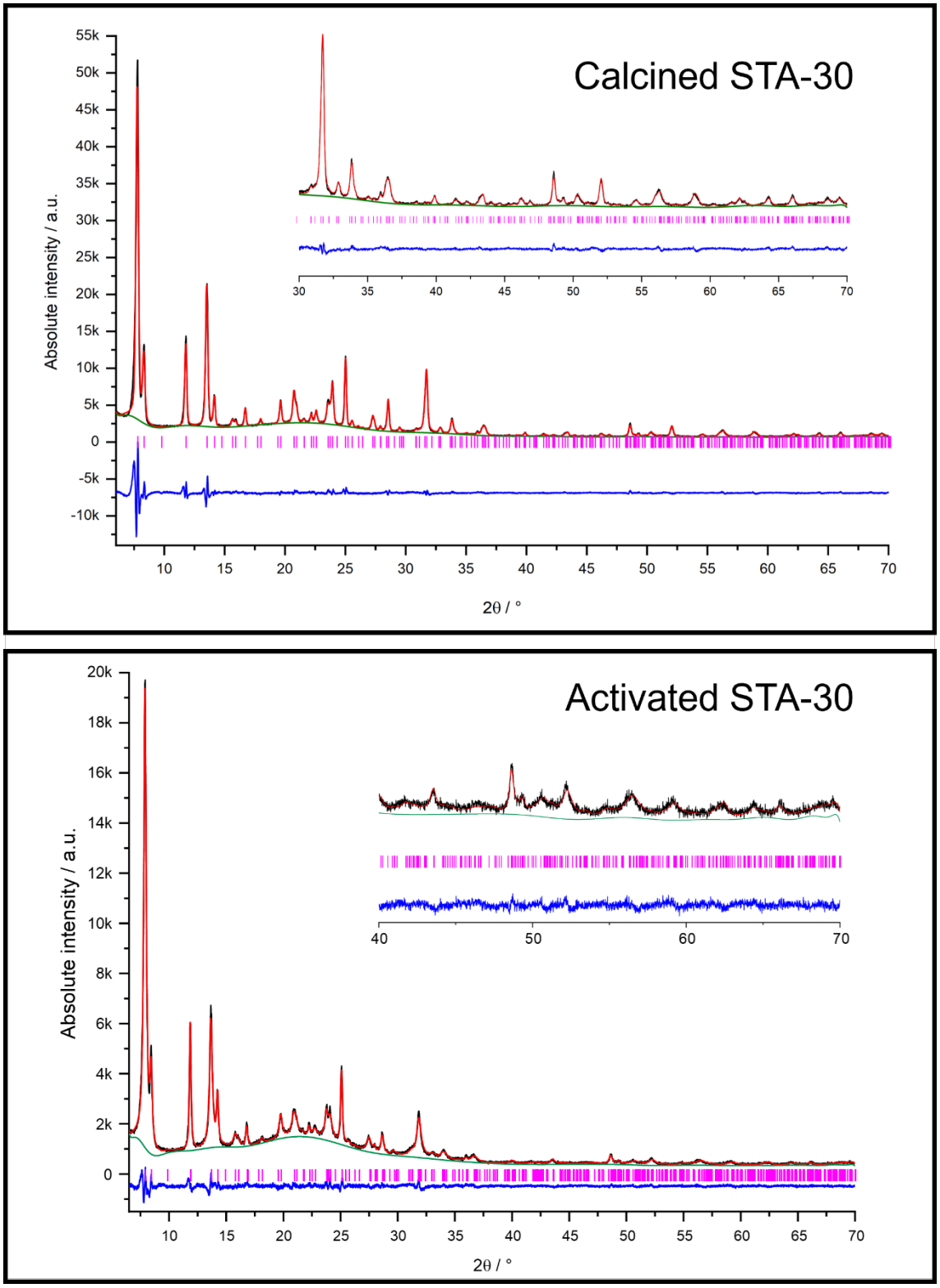

Figure 3.18 Rietveld fit for dehydrated calcined STA-30 (top) and dehydrated activated STA-30 (bottom), including experimental (black) and calculated (red) PXRD patterns, fitted background (green) and difference between the observed and calculated patterns (blue) and positions of calculated reflections (pink).

Table 3.3 Parameters and results of Rietveld refinement performed on STA-30 materials.

Sample	**Calcined, dehydrated**	**Activated, dehydrated**
Expected chemical composition	$H_{3.0}K_{6.1}Al_{9.1}Si_{62.9}O_{144}$	$H_{6.0}K_{3.0}Al_{9.0}Si_{63.0}O_{144}$
Data collection		
Temperature	298 K	298 K
X–Ray source	Cu X–ray tube	Cu X–ray tube
Diffractometer	STOE	STOE
Wavelength / Å	1.54056	1.54056
Unit cell		
Chemical formula	$K_{6.1}Al_{9.1}Si_{62.9}O_{144}$	$K_{2.7}Al_{9.0}Si_{63.0}O_{144}$
Crystal system	Hexagonal	Hexagonal
Space group	*P*6$_3$/*mmc*	*P*6$_3$/*mmc*
a / Å	13.0647(6)	12.9922(9)
b / Å	13.0647(6)	12.9922(9)
c / Å	29.9577(10)	29.9624(12)
Rietveld refinement		
Refined region / *2θ*°	6.0–70.0	6.5–70.0
Background	Chebyshev 24 terms	Chebyshev 30 terms
R_{wp} / %	7.56	4.71
R_p / %	5.10	3.67

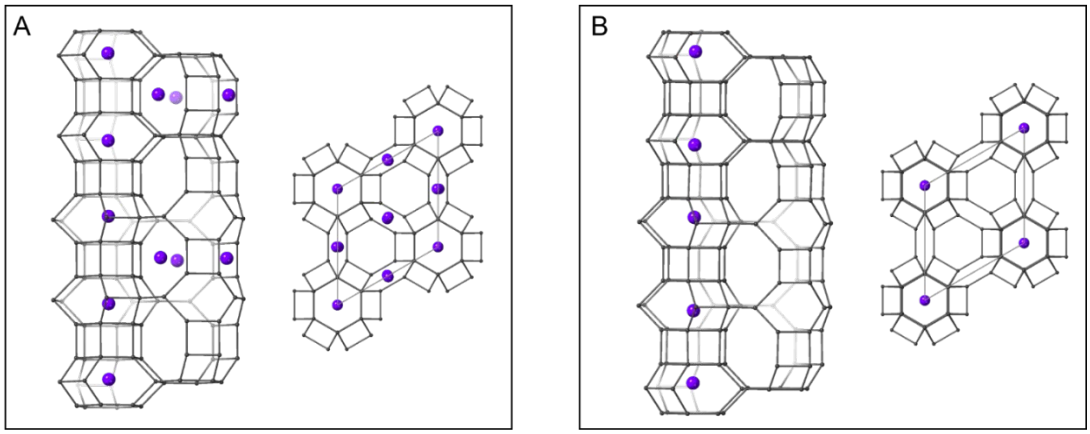

Figure 3.19 Schematic representation of the structures of dehydrated calcined (A) and activated (B) STA-30, represented with T–T connections and all possible positions for the K^+ cations (purple). O atoms omitted for clarity.

The refinements confirm the structure type of both calcined and activated STA-30 as SWY. Figure 3.20 shows that the framework contains a column of *can* cages connected by *d6r* units. Additionally, each *swy* cage is connected to other *gme* cages through 8Rs in a 'boat' configuration (Figure 3.20), and to other *swy* cages through 8Rs in a 'chair' configuration (top and bottom of *swy* cage in Figure 3.20). The 'boat' configuration is characterised by 2 mirror planes, whereas the 'chair' configuration is characterised by a mirror plane and an inversion plane. In calcined STA-30, K^+ cations were located in *can* cages and also in 8R sites between the *gme* cages and *swy* cages (boat–shaped), while the 8R sites between *swy* cages (chair–shaped) were not occupied. This is portrayed in Figure 3.21A–B. The ordering of the K^+ into one of the two types of 8R sites could be due to better coordination in the 'boat' 8R configuration rather than the 'chair' configuration but will also have the effect of minimising cation–cation repulsion. The refinement of the K^+ loading, coupled with the synthetic work described above, shows that the synthesis of a stable STA-30 material depends on the templating of the *can* cages and the occupation of some of the 8R sites, revealing a strong connection between the extra–framework cations and the framework structure. However, it is possible to remove the K^+ cations in these sites without affecting the structure of the material, as shown by the intact *swy* cage in Figure 3.21C.

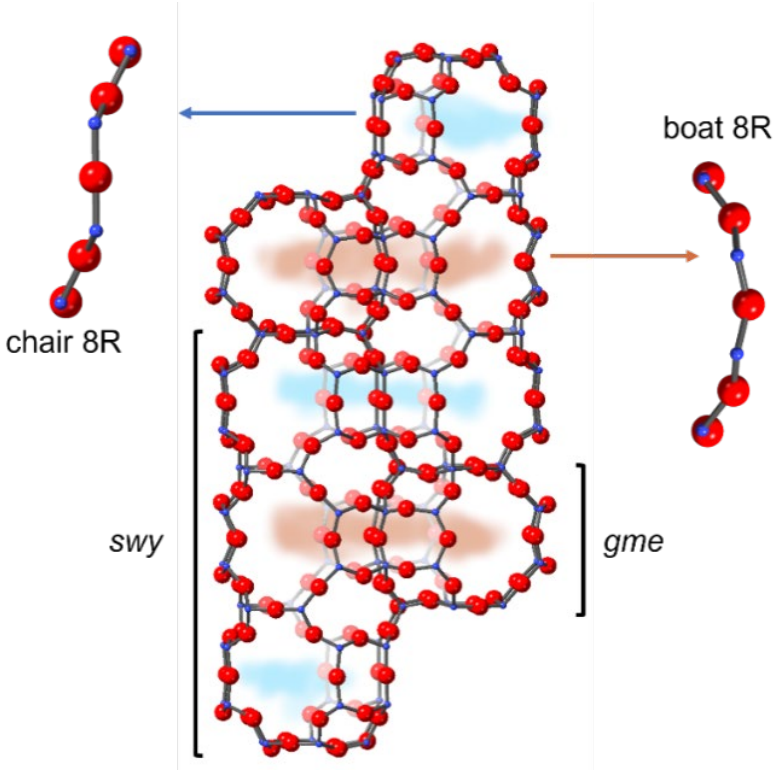

Figure 3.20 The *swy* and *gme* cages in the framework structure of activated STA-30 material drawn with T–O connections (T atoms – blue, O atoms – red) and showing the connectivity between the cages (blue shading *swy*–*swy* connectivity through 'chair' 8R and brown shading *swy*–*gme* connectivity through 'boat' 8R), the projections across the openings of which are given in the Figure.

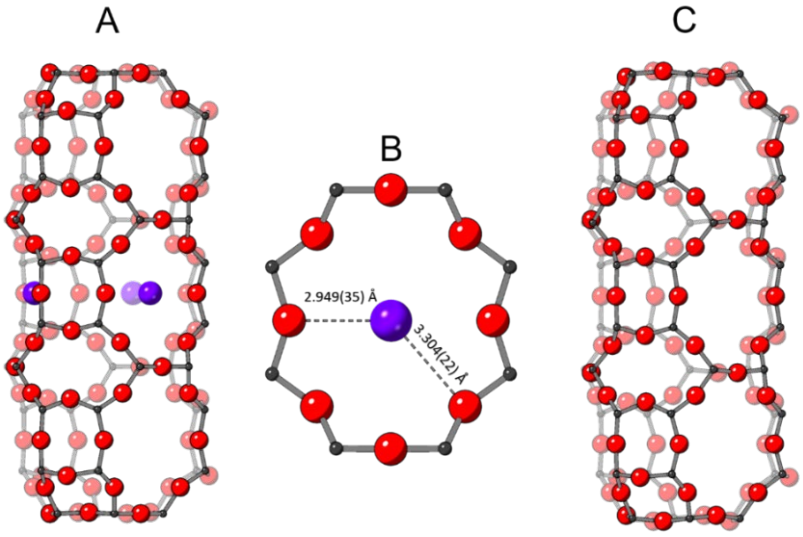

Figure 3.21 The *swy* cage of calcined STA-30 with the K^+ cation in the boat–shaped 8–ring (A), showed with K–O distances (B) and the *swy* cage of activated STA-30 (C).

In the activated form, there were no K^+ cations in the 8R sites, while the *can* cages remained ~75% occupied. This indicates that while the K^+ cations in the 8R windows

were completely removed by ion exchange with NH_4^+, those in *can* cages could not be removed even if the ion exchange was performed at elevated temperatures (up to 363 K) for many hours. This suggests that, under these conditions at least, the K^+ ions could not escape from the *can* cages because that would require migration through the puckered 6Rs.

The structure of the as–prepared form was also refined, but in this case, it was not possible to dehydrate the solid fully without partially decomposing the template, because the presence of the organic molecule prevented diffusion of water molecules out of the structure at temperatures below that at which the template would start to react. The diDABCO-C8^{2+} molecule was included within the *swy* cages in an energy–minimised location in the starting model, and its occupancy allowed to refine. It was found that this had to be capped at a value of 2 molecules/unit cell. K^+ cations were refined at the locations observed in the calcined material, and additional scattering refined as O atoms of water (or OH^- groups). Some details remained unresolved and some peaks (~5.8° and ~9.8°) are not fitted well due to the challenges described above. Nonetheless, the profile fit, and the similarity of unit cell parameters (Table 3.4 and Figure 3.22, structural parameters in Appendix Table 3.2) indicate the framework structure of this form is the same as that of the calcined form.

Table 3.4 Parameters and results of Rietveld refinement performed on as–prepared STA-30.

Sample	**As–prepared, dehydrated**
Expected chemical composition*	$(diDABCO\text{-}C8)_{1.5}K_{6.4}Al_{8.9}Si_{63.1}O_{144}$
Data collection	
Temperature	298 K
X–Ray source	Cu X–ray tube
Diffractometer	STOE
Wavelength / Å	1.54056
Unit cell	
Chemical formula	$(C_{20}N_4H_{40})_{2.0}K_{7.3}Al_{8.9}Si_{63.1}O_{145}$
Crystal system	Hexagonal

Space group	$P6_3/mmc$
a / Å	13.0702(4)
b / Å	13.0702(4)
c / Å	30.0210(8)
Rietveld refinement	
Refined region / *2θ*°	4.5–70.0
Background	Chebyshev 24 terms
R_{wp} / %	6.73
R_p / %	5.25

*The diDABCO-C8^{2+} expected content was determined by calculating the difference between the K and Al content of the calcined material.

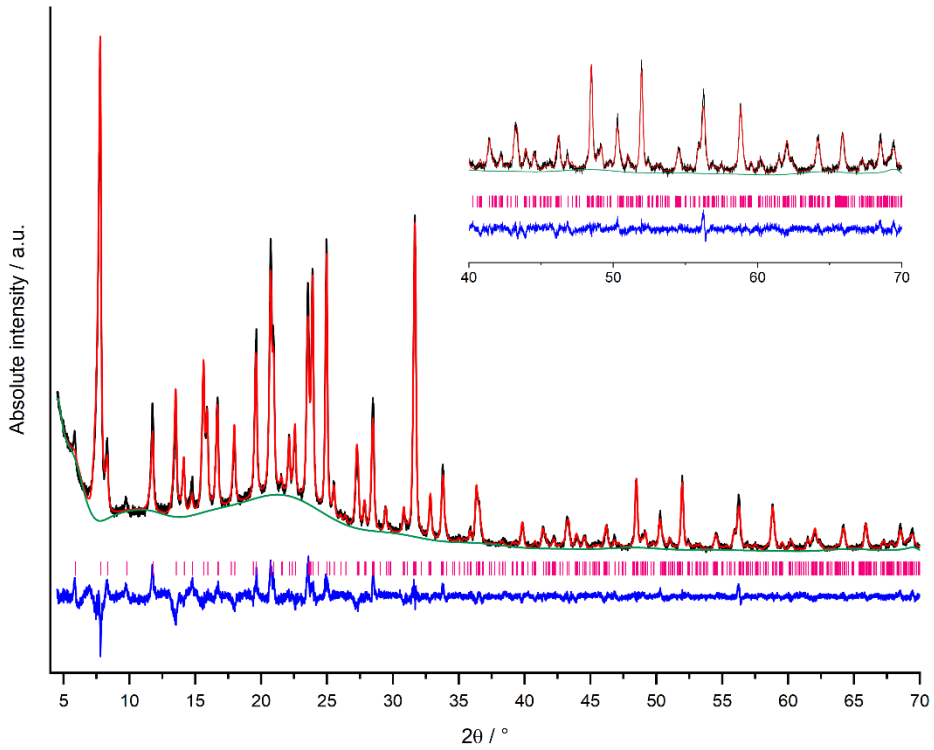

Figure 3.22 Rietveld profile fit for dehydrated as–prepared STA-30, including the experimental (black) and calculated (red) PXRD patterns, the fitted background (green) and the difference between the observed and calculated patterns (blue). Peak positions are indicated by pink tickmarks.

As a complementary structural method, the activated form was investigated by electron microscopy. SAED patterns of the activated material were collected along the [100] direction (Figure 3.23) which show that there is no disorder in the 12–layer stacking sequence in STA-30 since there is no streaking.[41] High–resolution STEM images (processed with an ABSF filter) along the same zone axis, Figure 3.23, further confirmed these findings, showing the ordered SWY framework of STA-30 at atomic resolution. A closer observation of the 12–layer stacking sequence is shown inset. These images are also consistent with the SWY topology, as shown by the unbroken columns of *can*/*d6r* units and the strict alternation along the *c*–axis of double combined *can* and *d6r* building units with different orientations along the *b*–axis.

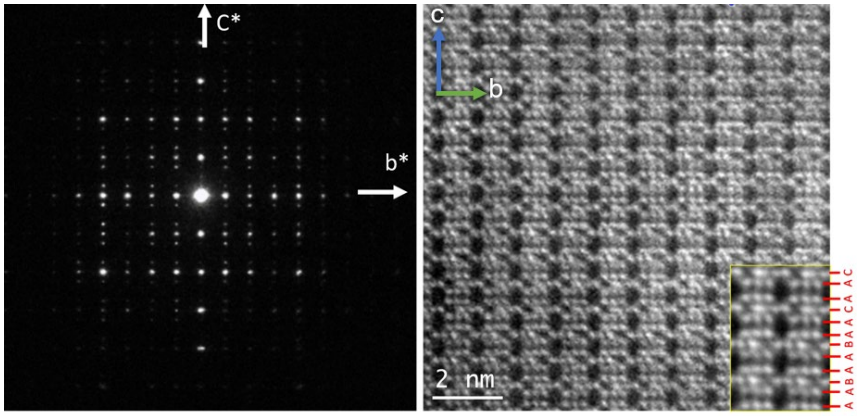

Figure 3.23 (Left) SAED pattern of STA-30 down the [100] direction and (right) C_s–corrected STEM–ADF image of the framework of STA-30 with arrangement of *can* cages highlighted. A closer observation of the framework is shown inset, where the stacking sequence is marked. The image was processed by application of an ABSF filter. Images collected and processed by Prof. Alvaro Mayoral.

Solid–state NMR spectroscopy of activated STA-30

The ^{27}Al MAS NMR spectra of the hydrated activated material shows two well–defined resonances at –2.0 ppm and –3.1 ppm, chemical shifts associated with octahedrally–coordinated Al, as well as the major peak at 57.8 ppm due to the expected tetrahedrally–coordinated framework Al (Figure 3.24A). The narrow lineshape of the 'octahedral' signals, as well as the absence of any five–fold coordinated signals, argues against these being from extra–framework Al (EFAL) typically observed after hydrothermal treatment, or steaming. It is increasingly becoming apparent that sharp resonances in H-forms of zeolites are more likely to be due to octahedral framework species, formed reversibly from tetrahedral framework Al by the incorporation of water molecules into their coordination shell.[42–44] These species are reported to revert to tetrahedral coordination if the H-zeolites are converted to the ammonium form.[43] Therefore, to investigate whether

the octahedral Al in hydrated K,H-STA-30 can also be converted back to tetrahedral species, a sample was ion exchanged into the ammonium form. ^{27}Al NMR spectra of this sample (Figure 3.24A) show that the two sharp upfield resonances disappear, strongly suggesting that the coordination of the Al species reverts to tetrahedral. The observation of two distinct signals suggests that these are octahedral framework Al species in different crystallographic sites in the zeolite framework. It is worth noting that there is a very small broad peak around -2.7 ppm present in the ^{27}Al NMR spectrum of the NH_4^+–exchanged sample that can be correlated to a similar feature in the ^{27}Al NMR spectrum of the H-form that overlaps with the sharp peaks. This may indicate the presence of a very small amount of EFAL.

^{1}H MAS NMR spectra from a dehydrated sample of the activated form of the material (Figure 3.24B) gives peaks at 4 ppm and 1.7 ppm. The signal at 4 ppm is assigned, based on previous studies, to Brønsted hydroxyls while the strong signal at 1.7 ppm is similar to previous observations on zeolite Beta and by analogy is assigned as silanol groups, $(SiO)_3SiOH$, indicating an appreciable number of defects in the structure.[45–47]

^{1}H MAS NMR spectra of the NH_4–exchanged form of activated STA-30 (Figure 3.24B) showed that the Brønsted hydroxyls are removed (as expected) and replaced with ammonium protons (peaks at 6.3 ppm and 6.7 ppm), while the defect hydroxyl groups remain. It was possible to investigate the nature of the 1.7 ppm ^{1}H signal further by ^{1}H–^{29}Si HETCOR spectroscopy on the ammonium–exchanged STA-30 (Figure 3.25). While the ammonium protons correlate with all the framework Si signals, the hydroxyl protons correlate with a ^{29}Si signal at −102 ppm, which can be attributed to silanol ^{29}Si, $(SiO)_3{}^{29}\underline{Si}OH$.

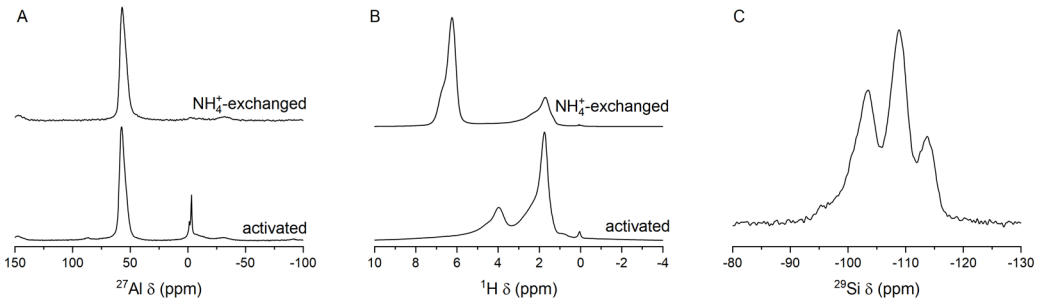

Figure 3.24 Solid–state MAS NMR data of activated STA-30: (A) ^{27}Al NMR spectra of hydrated activated (H,K-) and NH_4^+–forms, (B) ^{1}H NMR spectra, dehydrated activated and NH_4^+–forms and (C) ^{29}Si NMR spectrum, hydrated H,K-STA-30.

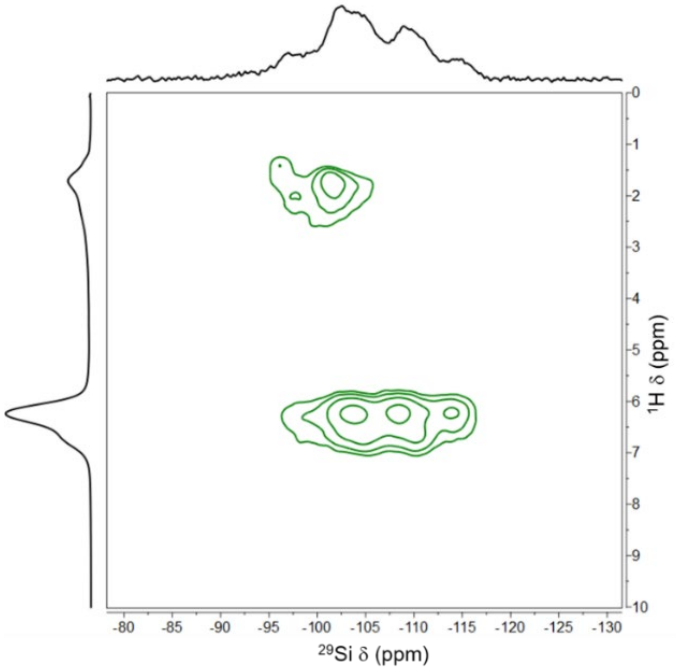

Figure 3.25 ^{1}H–^{29}Si HETCOR spectrum of the NH_4^+–exchanged STA-30.

Knowing both the crystal structure and the defect structure of STA-30 it was then possible to analyse the ^{29}Si spectrum of activated STA-30 (Figure 3.24C). NMR–DFT calculations carried out on an all–silica SWY structural model revealed that the ^{29}Si chemical shift of one of the three crystallographically distinct sites (all of which have the same multiplicity, 24) is expected to be nearly 7 ppm different from the other two, which are magnetically very similar. Resonances are predicted at −115.7 ppm (site T_1) and −109.0 ppm (sites T_2 and T_3) in a ratio of 1:2 (Figure 3.26). Similar differences in ^{29}Si chemical shift are measured (and predicted) for the zeolites offretite and omega (mazzite), for example.[40] Assuming (i) that the ^{29}Si spectrum is composed of two sets of Q^4 peaks of the form $(Si(OSi)_n(OAl)_{4-n}$, n = 0, 1 and 2), one set from each 'group' of similar T–sites, in the ratio 1 (upfield): 2 (downfield), and (ii) that there is a resonance for Q^3 $^{29}SiOH(OSi)_3$ at −100 ppm, it was possible to deconvolute the spectrum and derive a SiO_2/Al_2O_3 of 13±1, close to the value measured by XRF (14.1) (Figure 3.27).

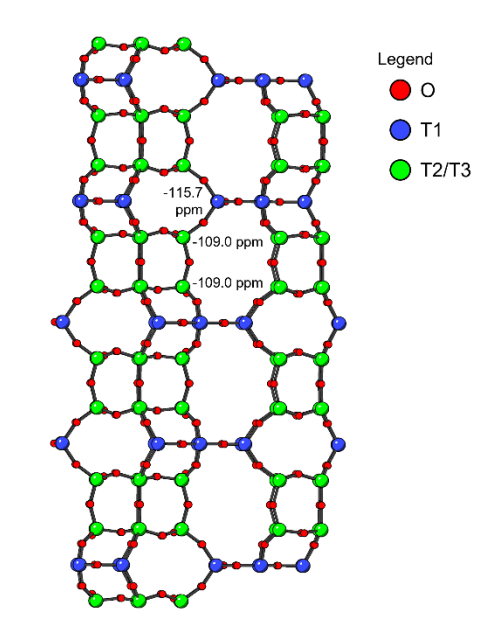

Figure 3.26 The three unique T sites in a silica SWY framework, labelled with the associated ^{29}Si peak shifts simulated from CASTEP NMR calculations ($\delta_{GIPAW} = \sigma_{ref} - \sigma_{GIPAW}$, σ_{ref} = 328).

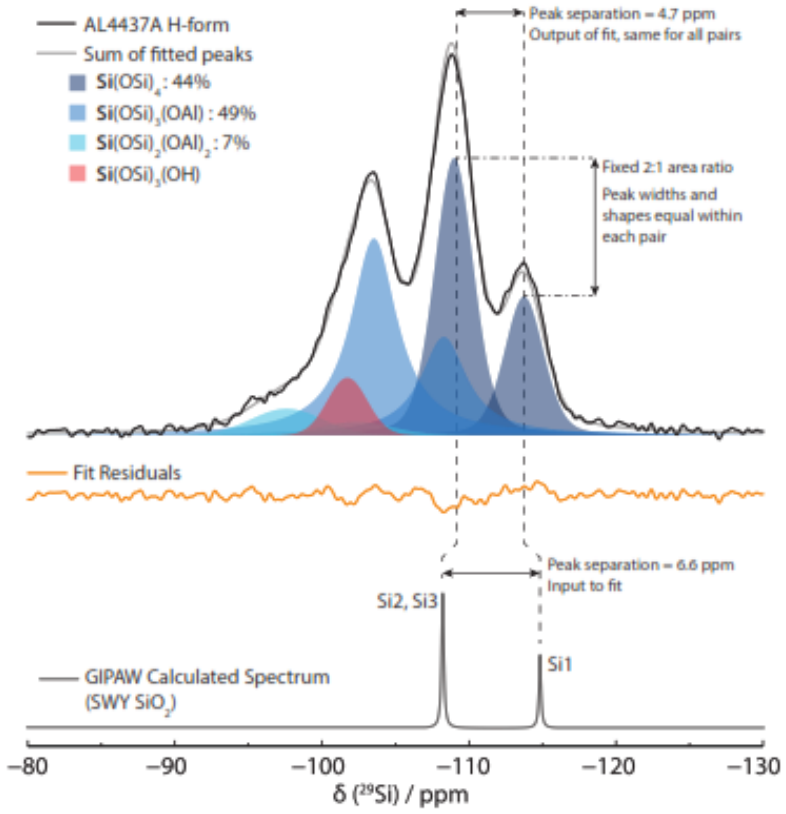

Figure 3.27 ^{29}Si MAS NMR spectrum with the peak assignment and fit, along with the simulated ^{29}Si NMR spectrum obtained from NMR–DFT calculations on the ideal SWY silicate framework, where Si*n* denotes a T site according to the coordinates provided on the IZA database.[10] Deconvolution performed by Jonathan Bradley.

Physical properties of activated STA-30

STA-30 was found to be microporous, exhibiting a type I isotherm when adsorbing N_2 at 77 K (Figure 3.28). The micropore volume was calculated to be 0.31 $cm^3\ g^{-1}$ assuming that the pores were fully filled at p/p_0 = 0.1. This is larger than the micropore volume reported by Łukaszuk *et al.* for aluminosilicate materials with the closely–related OFF topology type (0.25 $cm^3\ g^{-1}$) although that sample also possessed 0.05 $cm^3\ g^{-1}$ of mesopore volume.[39] H,K-STA-30 also had a larger micropore volume than H,K-ERI (0.25 $cm^3\ g^{-1}$) that was used as a benchmark in this study. The inset for $p/p_0 < 0.1$ also shows the N_2 adsorption isotherm of H,K-ERI follows a more predictable shape for a Type I isotherm. This unexpectedly higher pore volume than erionite is addressed via analysis of Ar isotherms in Chapter 4.

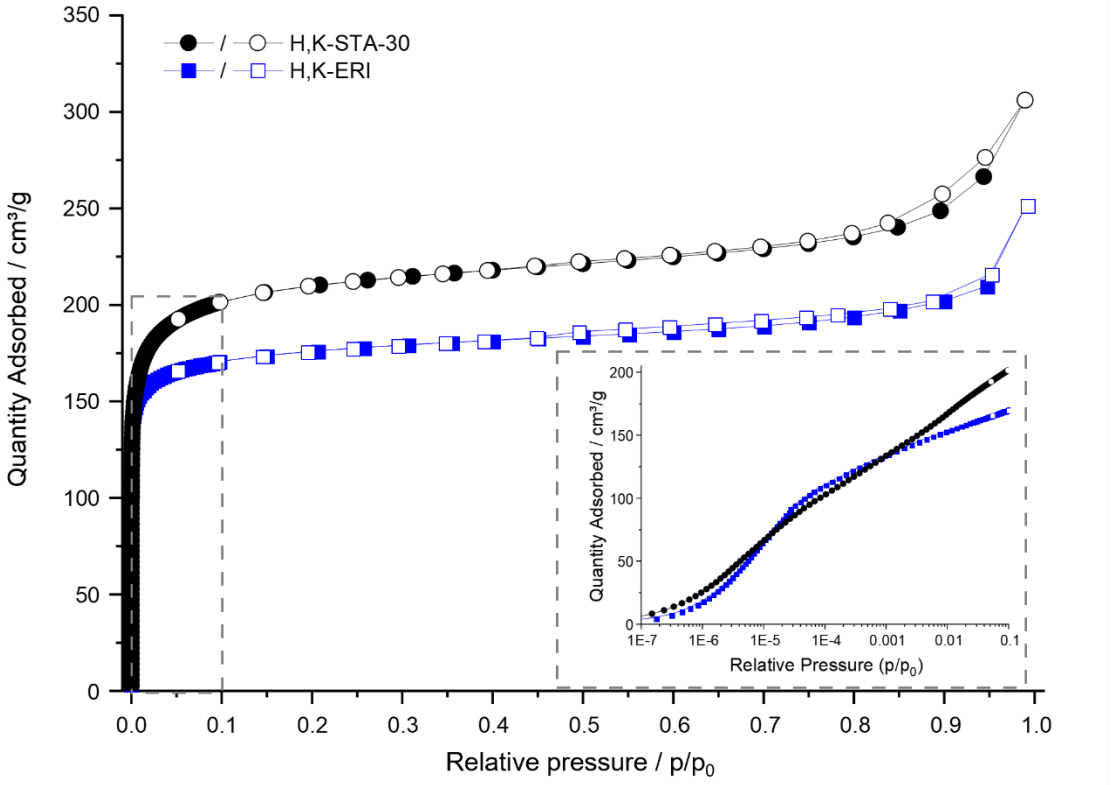

Figure 3.28 N_2 adsorption at 77 K isotherm measured on the activated H,K-STA-30 and H,K-ERI, shown with an insert focused on the 0 – 0.1 range plotted on a log scale.

SCR Catalysis

Small pore zeolites, particularly those with *d6r* units in the ABC-6 family, have been used successfully as commercial catalysts in NO_x abatement technology. Erionite is a zeolite in the ABC-6 family that has shown promising performance due to its high activity and

hydrothermal stability.[48,49] Therefore, STA-30 samples with Si/Al ratios of 5.8 and 6.3 (Samples 5 and 9 in Table 3.2) were synthesized, calcined, and activated according to the methods described and the benchmark synthetic erionite sample of similar Si/Al ratio and morphology was prepared and activated as well. The materials were loaded with 3.33 wt.% Cu cations in extra–framework ion exchange positions as described (Cu-STA-30(5.8), Cu-STA-30(6.3) and Cu-ERI(6.1)). These samples were then investigated as catalysts in NH_3–mediated NO_x reduction to probe the applicability of the aluminosilicate STA-30. Further details on sample preparation and catalyst testing are available in the Experimental section.

The results of the SCR tests are given in Figure 3.29. Typically, diesel vehicles are calibrated to operate with exhaust gases in the temperature range of 523 – 773 K: previous studies have indicated that the activity of Cu-SSZ-13 for this reaction increases rapidly as temperature increases from 450 to 575 K under similar conditions.[50]

Both STA-30 samples exhibited good catalytic activity, achieving greater than 90% NO_x conversion across the entire target operating window (523 – 773 K). Additionally, during cold start conditions, it is beneficial for NO_x abatement catalysts to exhibit low light–off temperatures. A useful metric for quantifying light–off temperature is the T_{50} value, which is the temperature at which 50% NO_x conversion is reached. The Cu-ERI(6.1), Cu-STA-30(6.3), and Cu-STA-30(5.8) samples achieved T_{50} values of about 450, 460, and 470 K, respectively. This might be explained by the Cu:Al ratios of these samples. As reported in a number of studies, Cu:Al ratios approach an ideal value of ~0.5 for Cu-exchanged zeolites utilized as SCR catalysts.[51,52] In Cu-STA-30(5.8) the Cu:Al ratio was 0.22 but taking the K cations in the *can* cages into account, the ratio of Cu: residual framework charge (Al minus K) = 0.31. For Cu-STA-30(6.3) the corresponding ratios are 0.23 and 0.34, a little closer to the optimum value.

The N_2O selectivity values of the Cu–loaded STA-30 catalysts were also evaluated (Figure 3.29B). N_2O is an unwanted by–product of NH_3–mediated NO_x reduction. In emissions control systems for diesel vehicles, it is highly desirable to minimize the production of N_2O because it is a particularly potent greenhouse gas. While increasing the Cu:Al ratio gave a positive effect on NO_x light–off temperature, there is a penalty in N_2O selectivity. Peak N_2O selectivity is increased from 2.5% to 3.5% when the Si/Al ratio of STA-30 Si/Al ratio is increased from 5.8 to 6.3. A comparison of the ERI reference to STA-30, however, demonstrates that the framework topology of the zeolite can have an impact on N_2O selectivity. The Cu-ERI(6.1) sample exhibited a lower N_2O selectivity at

2.5% relative to the Cu-STA-30(6.3) sample and an equivalent N_2O selectivity to the Cu-STA-30(5.8) sample. These effects demonstrate how zeolite topology, Al content, and Cu content are all factors in NO_x abatement technology and must be tuned for optimal performance.

These preliminary NH_3–SCR tests indicate Cu-STA-30 exhibits promising activity as an SCR catalyst. As demonstrated for the CHA zeolite as an SCR catalyst, the Cu:Al ratio affects both low temperature NO_x conversion and N_2O selectivity across the entire temperature range.[51–53] The aluminosilicate zeolite STA-30 therefore warrants further investigation and optimization as a NH_3–SCR catalyst.

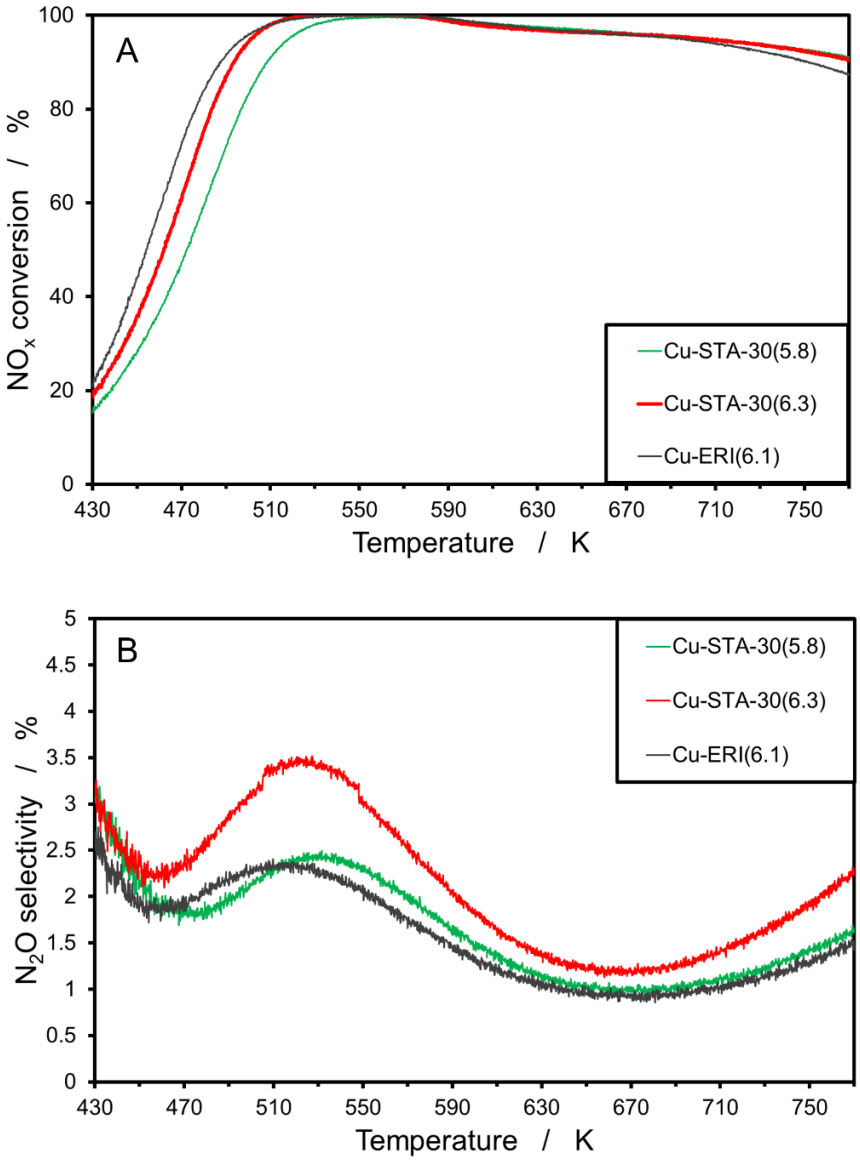

Figure 3.29 NH_3–SCR light-off curves (A) and N_2O yield plots (B) for Cu-STA-30(5.8), Cu-STA-30(6.3) and Cu-ERI(6.1) fresh samples, which all have a loading of 3.33 wt.% Cu cations.

However, the 'aged' data presented in Figure 3.30 indicates that all samples tested have poor NO_x conversion after aging. This implies that the Cu-STA-30 samples have poor stability, which might be due to the large amount of SiOH groups observed in the solid–state NMR spectra (Figure 3.24). The Cu-ERI sample showed similar instability, albeit with a slightly higher NO_x conversion that the STA-30 samples. Thus, further investigation is required into all these samples to explain the lack of stability upon aging and understand how it could be improved. This will be the subject of the next chapter.

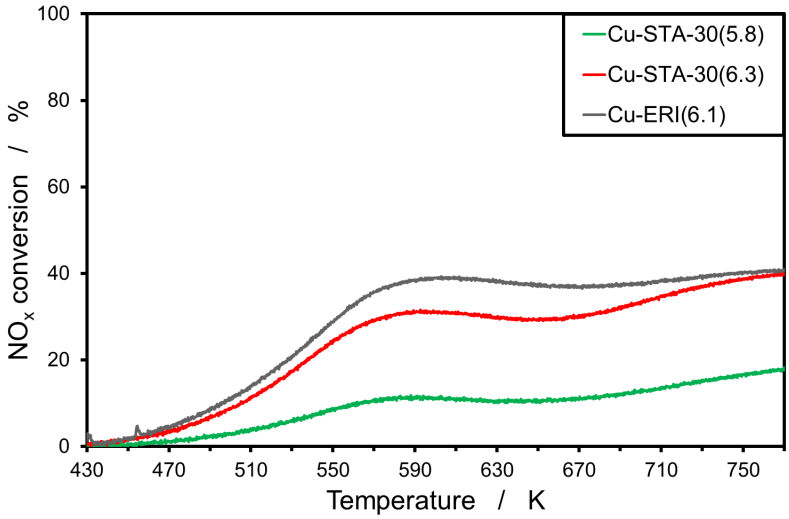

Figure 3.30 Aged data – NH_3–SCR light–off curves and N_2O yield plots for Cu-STA-30(5.8), Cu-STA-30(6.3) and Cu-ERI(6.1) samples, which all have a loading of 3.33 wt.% Cu cations and then aged at 1023 K, 80 h in 10% water.

MTO Catalysis

STA-30 was also examined as a catalyst for the MTO reaction, for which small pore zeolites are known to be active and selective.[2] In addition to the H,K-ERI benchmark sample prepared for comparison with STA-30, the activity of these materials as MTO catalysts was also compared to an SSZ-13 (aluminosilicate CHA) sample of similar Si/Al provided by JM. As previously mentioned, both SAPO and aluminosilicate CHA are considered standards for MTO catalysis.[2]

According to the mass spectrometry (MS) data collected from the three samples (Figure 3.31), both H,K-ERI (6.1) and H,K-STA-30 (6.9) are active as MTO catalysts at 623 K since mass traces corresponding to C_2–C_4 products are observed. However, compared to H-SSZ-13 (6.5), the onset of deactivation is much earlier for both ERI and STA-30. This is evidenced by a rapid increase in the methanol trace, indicating lower conversion and in the dimethyl ether (DME) trace, corresponding to a higher selectivity to DME than

to hydrocarbon products. This is only observed after about 100 min reaction time for SSZ-13 (6.5), but starts occurring after 20 min for H,K-ERI (6.1) and H,K-STA-30 (6.9).

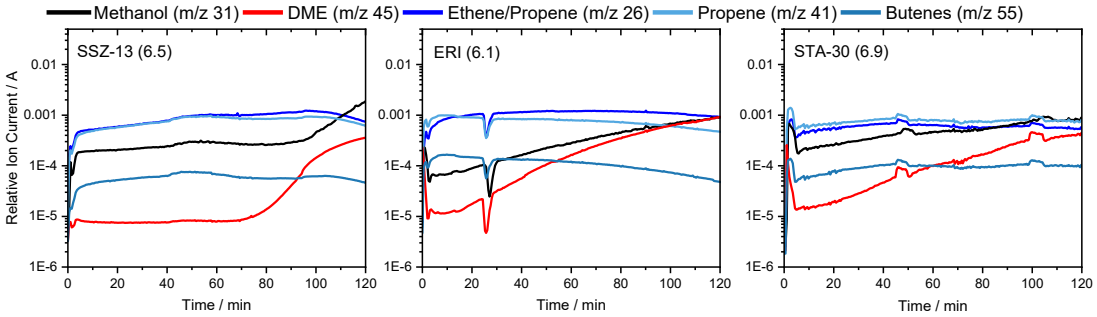

Figure 3.31 Mass traces of methanol and reaction products at 623 K from activated forms of SSZ-13 (6.5), ERI (6.1) and STA-30 (6.9), monitored by MS as mass–to–charge (m/z) ratio. (The sudden drops and humps in the data are due to a faulty syringe.)

For a better understanding of the activity of the three different samples, operando UV–Vis spectra were collected during the reaction. This allowed the observation of various hydrocarbon species inside the zeolite. The identification of the various peaks was based on previous studies by Borodina *et al*. and Dai *et al*.[54,55] The most remarkable difference between SSZ-13 and STA-30 is the fact that naphthalenes/trienyl species (~440 nm) are no longer predominant over the larger polyaromatics in the latter. In fact, the ratio of polyenes to larger polyaromatic species decreases in the order SSZ-13 > ERI > STA-30. This decreasing ratio is in line with the increasing size of the largest cage in the CHA, ERI and SWY topologies (Figure 3.33). A previous study by Lezcano–Gonzalez *et al.* has demonstrated that extended polyenes act as the precursors for deactivating species in SSZ-13, by producing naphthalenes and polyaromatics which block the *cha* cage.[56] Thus, the different distribution of these species among the three samples could indicate that increasing the cage size of the catalyst could lead to differences in the behaviour of the hydrocarbon pool. This means that naphthalenes could act as active species in the larger *eri* and *swy* cages while larger polyaromatics would deactivate the catalyst by blocking the cages. Further studies on the activity of STA-30 materials as catalysts for the MTO reaction are being carried out by our collaborators at UCL.

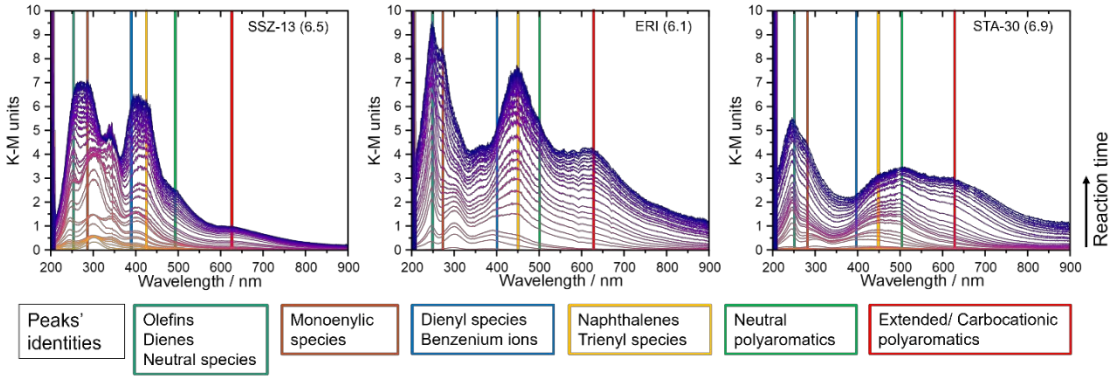

Figure 3.32 Operando UV–Vis spectra collected during conversion of methanol at 623 K over activated SSZ-13 (6.5), ERI (6.1) and STA-30 (6.9), with peaks labelled in different colours corresponding to the legend below the collections of spectra.

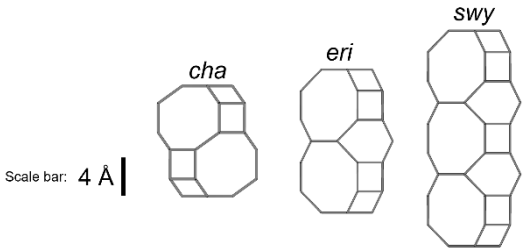

Figure 3.33 Large cage structures for the CHA, ERI and SWY topologies (drawn to scale).

Conclusion

An aluminosilicate zeolite with the SWY topology type (STA-30) has been prepared for the first time, via a designed synthesis involving the selection of organic template by modelling and judicious use of inorganic cations. While the organic alkylammonium diDABCO-C8 dication gives an optimal fit to the *swy* cage (the longest observed in an ordered ABC-6 type zeolite) the K^+ cation favours crystallisation of zeolites that contain *can* cages. The synthesis was tuned to increase the framework Si/Al and optimise stability and modified to permit economical scale up.

Rietveld refinement against PXRD data established that STA-30 has the SWY framework in as–prepared, calcined and activated forms. Selected area diffraction and C_s–corrected STEM imaging confirmed the 12–layer stacking sequence repeat AABAABAACAAC and showed that it is maintained fault–free over extended distances. Parallel columns of alternating *d6r*s and *can* cages run along the *c*–axis in the framework. Between these are alternating *swy* and *gme* cages, connected via 8R windows, which comprise the pore space. In the as–prepared form, diDABCO-C8 cations occupy the *swy* cages, but can be removed by calcination to leave the framework intact. K^+ cations are located in the *can*

cages, from which they cannot be removed by ammonium ion exchange, and also 8R windows of the *gme* cages, from which they can.

The calcined, ammonium–exchanged and then deammoniated K,H-form exhibits Brønsted acid sites and defect silanol protons. Upon rehydration of the acid form of the zeolite, a significant fraction of the framework Al transforms from tetrahedral to octahedral, giving two well resolved narrow resonances in the ^{27}Al NMR spectra. These are interpreted to be octahedral framework Al cations ($Al(OSi)_4(OH_2)_2$) in crystallographically–distinct T–sites (the first time this resolution between octahedral framework sites has been reported): their coordination can be reversibly transformed to tetrahedral by ammonium ion exchange.

The dehydrated K,H-STA-30 shows a microporous volume of 0.31 $cm^3\ g^{-1}$, which indicates the acid form of the zeolite is stable and the pore space, connected via 8R windows, is fully accessible. It is therefore a candidate for conversions known to be catalysed by small pore zeolites: Cu–loaded STA-30 shows appreciable activity for deNOx and K,H-STA-30 is an activate catalyst in the MTO reaction. We therefore consider this route to successful designed synthesis, as a high Si/Al zeolite, of a topology type known previously but as an silicoaluminophosphate, is a promising approach for further catalyst discovery.

Nevertheless, there are a number of aspects of the study described in this Chapter that warrant further investigation. Firstly, the influence of the use of the CDM approach on the properties of the zeolite synthesised should be considered. In relation to this, the design of new routes to STA-30 would aid in the systematic study of synthetic parameters on the final zeolite material produced. Secondly, additional investigations are necessary to explain the unusual increased porosity of STA-30 compared to ERI. Finally, more evidence is necessary to explain the amount of silanol groups observed in the H-forms of STA-30 zeolites. All of these aspects will be explored in the next chapter.

References

1 M. Moliner, C. Martínez and A. Corma, *Chem Mater*, 2014, **26**, 246–258.

2 M. Dusselier and M. E. Davis, *Chem Rev*, 2018, **118**, 5265–5329.

3 P. Tian, Y. Wei, M. Ye and Z. Liu, *ACS Catal*, 2015, **5**, 1922–1938.

4 M. A. Deimund, L. Harrison, J. D. Lunn, Y. Liu, A. Malek, R. Shayib and M. E. Davis, *ACS Catal*, 2016, **6**, 542–550.

5 J. H. Kwak, R. G. Tonkyn, D. H. Kim, J. Szanyi and C. H. F. Peden, *J Catal*, 2010, **275**, 187–190.

6 A. M. Beale, F. Gao, I. Lezcano-Gonzalez, C. H. F. Peden and J. Szanyi, *Chem Soc Rev*, 2015, **44**, 7371–7405.

7 M. Moliner, C. Franch, E. Palomares, M. Grill and A. Corma, *Chem Comm*, 2012, **48**, 8264–8266.

8 Y. Shan, W. Shan, X. Shi, J. Du, Y. Yu and H. He, *Appl Catal B*, 2020, **264**, 118511.

9 P. G. Blakeman, E. M. Burkholder, H.-Y. Chen, J. E. Collier, J. M. Fedeyko, H. Jobson and R. R. Rajaram, *Catal Today*, 2014, **231**, 56–63.

10 IZA database, http://www.iza-structure.org/databases/, (accessed 30 June 2023).

11 H. Lee, W. Choi, H. J. Choi and S. B. Hong, *ACS Mater Lett*, 2020, 981–985.

12 Y. Li, X. Li, J. Liu, F. Duan and J. Yu, *Nat Commun*, 2015, **6**, 8328.

13 B. M. Lok, C. A. Messina, R. L. Patton, R. T. Gajek, T. R. Cannan and E. M. Flanigen, *J Am Chem Soc*, 1984, **106**, 6092–6093.

14 D. W. Fickel, E. D'Addio, J. A. Lauterbach and R. F. Lobo, *Appl Catal B*, 2011, **102**, 441–448.

15 A. Wang, Y. Chen, E. D. Walter, N. M. Washton, D. Mei, T. Varga, Y. Wang, J. Szanyi, Y. Wang, C. H. F. Peden and F. Gao, *Nat Commun*, 2019, **10**, 1–10.

16 S. T. Wilson, R. W. Broach, C. S. Blackwell, C. A. Bateman, N. K. McGuire and R. M. Kirchner, *Microporous Mesoporous Mater*, 1999, **28**, 125–137.

17 US Pat., US 4508837A, 1985.

18 J. M. Bennett, R. M. Kirchner and S. T. Wilson, in *Zeolites: Facts, Figures, Future Part A - Proceedings of the 8th International Zeolite Conference*, eds. P. A. Jacobs and R. A. van Santen, Elsevier, 1989, vol. 49, pp. 731–739.

19 US Pat., US 10,343,927 B2, 2019.

20 A. Turrina, R. Garcia, A. E. Watts, H. F. Greer, J. Bradley, W. Zhou, P. A. Cox, M. D. Shannon, A. Mayoral, J. L. Casci and P. A. Wright, *Chem Mater*, 2017, **29**, 2180–2190.

21 M. W. Deem, R. Pophale, P. A. Cheeseman and D. J. Earl, *J Phys Chem C*, 2009, **113**, 21353–21360.

22 G. Sastre, A. Cantin, M. J. Diaz-Cabañas and A. Corma, *Chem Mater*, 2005, **17**, 545–552.

23 M. Gálvez-Llompart, A. Cantín, F. Rey and G. Sastre, *Z Kristallogr Cryst Mater*, 2019, **234**, 451–460.

24 E. D. Kuznetsova, O. A. Blatova and V. A. Blatov, *Chem Mater*, 2018, **30**, 2829–2837.

25 A. Turrina, R. Garcia, P. A. Cox, J. L. Casci and P. A. Wright, *Chem Mater*, 2016, **28**, 4998–5012.

26 R. Simancas, D. Dari, N. Velamazan, M. T. Navarro, A. Cantin, J. L. Jorda, G. Sastre, A. Corma and F. Rey, *Science*, 2010, **330**, 1219–1222.

27 J. E. Schmidt, M. W. Deem and M. E. Davis, *Angew Chem Int Ed*, 2014, **53**, 8372–8374.

28 C. Shi, L. Li, L. Yang and Y. Li, *Chin Chem Lett*, 2020, **31**, 1951–1955.

29 X. Hong, W. Chen, G. Zhang, Q. Wu, C. Lei, Q. Zhu, X. Meng, S. Han, A. Zheng, Y. Ma, A. N. Parvulescu, U. Müller, W. Zhang, T. Yokoi, X. Bao, B. Marler, D. E. De Vos, U. Kolb and F. S. Xiao, *J Am Chem Soc*, 2019, **141**, 18318–18324.

30 R. Castañeda, A. Corma, V. Fornés, F. Rey and J. Rius, *J Am Chem Soc*, 2003, **125**, 7820–7821.

31 A. Cantín, A. Corma, M. J. Diaz-Cabanas, J. L. Jordá and M. Moliner, *J Am Chem Soc*, 2006, **128**, 4216–4217.

32 D. Jo and S. B. Hong, *Angew Chem Int Ed*, 2019, **58**, 13845–13848.

33 J. Shin, D. Jo and S. B. Hong, *Acc Chem Res*, 2019, **52**, 1419–1427.

34 P. Guo, J. Shin, A. G. Greenaway, J. G. Min, J. Su, H. J. Choi, L. Liu, P. A. Cox, S. B. Hong, P. A. Wright and X. Zou, *Nature*, 2015, **524**, 74–78.

35 J. Shin, H. Xu, S. Seo, P. Guo, J. G. Min, J. Cho, P. A. Wright, X. Zou and S. B. Hong, *Angew Chem Int Ed*, 2016, **55**, 4928–4932.

36 J. Zhu, Z. Liu, K. Iyoki, C. Anand, K. Yoshida, Y. Sasaki, S. Sukenaga, M. Ando, H. Shibata, T. Okubo and T. Wakihara, *Chem Comm*, 2017, **53**, 6796–6799.

37 S. L. Burkett and M. E. Davis, *Chem Mater*, 1995, **7**, 920–928.

38 M. A. Miller, G. J. Lewis, J. G. Moscoso, S. Koster, F. Modica, M. G. Gatter and L. T. Nemeth, *Stud Surf Sci Catal*, 2007, **170**, 487–492.

39 K. A. Łukaszuk, D. Rojo-Gama, S. Øien-Ødegaard, A. Lazzarini, G. Berlier, S. Bordiga, K. P. Lillerud, U. Olsbye, P. Beato, L. F. Lundegaard and S. Svelle, *Catal Sci Technol*, 2017, **7**, 5435–5447.

40 C. A. Fyfe, G. C. Gobbi, G. J. Kennedy, J. D. Graham, R. S. Ozubko, W. J. Murphy, A. Bothner-By, J. Dadok and A. S. Chesnick, *Zeolites*, 1985, **5**, 179–183.

41 J. M. Cowley, in *Diffraction Physics*, Elsevier, 1995, pp. 257–285.

42 B. H. Wouters, T.-H. Chen and P. J. Grobet, *J Am Chem Soc*, 1998, **120**, 11419–11425.

43 M. Ravi, V. L. Sushkevich and J. A. van Bokhoven, *J Phys Chem C*, 2019, **123**, 15139–15144.

44 M. Ravi, V. L. Sushkevich and J. A. van Bokhoven, *Nat Mater*, 2020, **19**, 1047–1056.

45 A. A. Gabrienko, I. G. Danilova, S. S. Arzumanov, A. V Toktarev, D. Freude and A. G. Stepanov, *Microporous Mesoporous Mater*, 2010, **131**, 210–216.

46 M. Hunger, S. Ernst, S. Steuernagel and J. Weitkamp, *Microporous Materials*, 1996, **6**, 349–353.

47 A. G. Stepanov, eds. B. F. Sels and L. M. B. T.-Z. and Z.-L. M. Kustov, Elsevier, Amsterdam, 2016, pp. 137–188.

48 N. Martín, C. Paris, P. N. R. Vennestrøm, J. R. Thøgersen, M. Moliner and A. Corma, *Appl Catal B*, 2017, **217**, 125–136.

49 J. Zhu, Z. Liu, L. Xu, T. Ohnishi, Y. Yanaba, M. Ogura, T. Wakihara and T. Okubo, *J Catal*, 2020, **391**, 346–356.

50 J. H. Kwak, D. Tran, J. Szanyi, C. H. F. Peden and J. H. Lee, *Catal Letters*, 2012, **142**, 295–301.

51 F. Gao, N. M. Washton, Y. Wang, M. Kollár, J. Szanyi and C. H. F. Peden, *J Catal*, 2015, **331**, 25–38.

52 T. Ryu, H. Kim and S. B. Hong, *Appl Catal B*, 2019, **245**, 513–521.

53 F. Gao, E. D. Walter, M. Kollar, Y. Wang, J. Szanyi and C. H. F. Peden, *J Catal*, 2014, **319**, 1–14.

54 E. Borodina, F. Meirer, I. Lezcano-González, M. Mokhtar, A. M. Asiri, S. A. Al-Thabaiti, S. N. Basahel, J. Ruiz-Martinez and B. M. Weckhuysen, *ACS Catal*, 2015, **5**, 992–1003.

55 W. Dai, C. Wang, M. Dyballa, G. Wu, N. Guan, L. Li, Z. Xie and M. Hunger, *ACS Catal*, 2015, **5**, 317–326.

56 I. Lezcano-Gonzalez, E. Campbell, A. E. J. Hoffman, M. Bocus, I. V. Sazanovich, M. Towrie, M. Agote-Aran, E. K. Gibson, A. Greenaway, K. De Wispelaere, V. Van Speybroeck and A. M. Beale, *Nat Mater*, 2020, **19**, 1081–1087.

Chapter 4

Different synthetic routes to STA-30 and their influence on the zeolite product

Disclaimer: Some of the syntheses discussed in this chapter have been published as examples in the US 2022/0333519 A1 patent pending publication (authors: Ruxandra Georgiana Chitac, Nicholas McNamara, Alessandro Turrina, Paul Anthony Wright).[1] The examples have been written by myself, and the application for the patent was submitted in collaboration with the industrial sponsor for this work, Johnson Matthey. The characterisation data, along with some of the data on the specific synthetic routes will also constitute the main text and supporting information of a publication entitled 'Synthetic Control of Defect Structure and Hierarchical Microporosity in Aluminosilicate Zeolite SWY', authored by Ruxandra G. Chitac, Vladimir L. Zholobenko, Robin S. Fletcher, Emma Softley, Jonathan Bradley, Alvaro Mayoral, Alessandro Turrina, and Paul A. Wright (J. Am. Chem. Soc. 2023, 145, 40, 22097–22114).

Introduction

In the previous chapter, it was described how the synthesis of aluminosilicate SWY (STA-30) was designed through the cooperation between relevant literature surveys and computational modelling. While the synthesis was repeatable, reproducible, and scalable, the STA-30 zeolite obtained possessed a large amount of silanols (SiOH), which was greater than the amount of Brønsted acid sites. This was not reflected in poor crystallinity of the material or the stability of the activated form. However, during the NH_3–SCR testing, it was found that the lower hydrothermal stability of the zeolite caused it to have poor performance after aging. This effect is most likely due to the large amount of SiOH and, while this is not beneficial for this specific application, there is an increased interest in the potential of structures with large amounts of silanols.[2] Hence, it would be of interest to learn how to control this property of STA-30 from multiple perspectives.

In other studies in the literature on aluminosilicate ERI, it was shown that the CDM ERI also possessed a high concentration of defects, which lowered its hydrothermal stability. However, an 'ultrafast seeded' approach led to less defects and better stability.[3,4] Since

the initial STA-30 zeolite was prepared through a CDM type approach, it was useful to study whether there was an intrinsic effect of the synthetic approach that caused the formation of the large amount of silanols in aluminosilicate SWY or if any other component of the gel was causing this. Thus, more routes to STA-30 had to be designed so that each approach made use of similar starting materials and gel compositions, to allow for a systematic study of the root cause of the formation of the silanols. For this, it was explored how the zeolite STA-30 can be prepared through approaches other than CDM, namely a more conventional hydrothermal approach with no aging of the gel and also through interzeolite conversion, making use of zeolite Y as the Al source. Furthermore, the effect of other SDAs in the CDM approach and their impact on the properties of the STA-30 zeolite crystallised was also investigated. Selected samples were characterised fully through adsorption measurements, solid–state NMR spectroscopy, FTIR spectroscopy and STEM–ADF images. This shines a light on the key components of the synthesis that affect the defect structure in STA-30 zeolites.

Experimental considerations

CDM–type syntheses

In these syntheses, the aluminosilicate gel was prepared in TPAOH aq. sol. 40% by mixing it with an aluminium source and silica source. The gel was aged at 368 K for 20 hours in a PTFE lined stainless–steel autoclave. Any additional SDAs (organic or inorganic templates) were added to the gel by dissolving them in DI H_2O, unless specified otherwise. The gel was then heated at 403–413 K under autogenous pressure in a stainless–steel autoclave, with tumbling at 60 rpm, unless mentioned otherwise. This type of syntheses will be referred to as ‘CDM syntheses’ in the discussion since the aluminosilicate gel, prepared in a solution of the hydroxide form of a low–charge density organic molecule, was aged before the addition of ‘crystallisation’ SDAs.

Hydrothermal syntheses

The gel components in this type of approach were similar to those used in CDM syntheses, with two main exceptions. The mineraliser was not necessarily a low-charge density organic molecule, but it could also be a solution of the hydroxide form of the OSDA. Another key difference was the fact that the gel was not aged before heating it up to 403–413 K, with tumbling at 60 rpm, unless mentioned otherwise. Instead, the alumina and silica sources were dissolved in the mineraliser and mixed for at least 2 hours before the addition of any SDAs, either as solids or in solution. Syntheses that

involved no aging step will be referred to as 'hydrothermal syntheses' for distinction from other approaches that require additional steps apart from mixing all the reactants.

Partial Interzeolite Conversion (IZC)

Similarly to the previously described approach, the alumina and silica sources were mixed in a solution of the hydroxide form of the OSDA, rather than in a tetraalkylammonium hydroxide solution. The alumina source was a form of commercially available zeolite Y (FAU), called CBV 712, which was provided by JM. However, the silica originated from both CBV 712 and additional Ludox HS-40. The syntheses were carried in stainless–steel autoclaves at 433 K, with tumbling at 60 rpm, unless mentioned otherwise.

The syntheses were carried out in 50 mL or 125 mL stainless steel autoclaves, as well as Parr Stainless Steel 1.5 L autoclaves that were sealed and equipped with a double pitched blade type impeller, mixing the synthesis gel at 300 rpm. The scales will be referred to as small, medium and large, respectively.

Post–synthetic modification

All products were recovered by centrifugation and washed with DI H_2O until a neutral pH was achieved. The OSDAs were removed by calcination in air at temperatures up to 823 K to obtain the 'calcined' forms of materials. The zeolites were activated by stirring them with 10% NH_4Cl or 1 M NH_4Cl aq. sol. in proportion of 1 g zeolite / 100 mL solution, for 2 hours at 75°C. The procedure was repeated 5 times, replacing the NH_4Cl solution between runs. The zeolite was heated again in air at temperatures up to 823 K. This form of the zeolite will be referred to as 'H-form' or 'activated'. Other routes of activation explored in this work will be described in the results and discussion relevant section.

Results and discussion

Further CDM syntheses

In the previous chapter, it was outlined which modifications could be made to a gel consisting of TXAOH as mineraliser (X = Ethyl, Propyl or Butyl), aluminium isopropoxide or aluminium hydroxide as Al sources, Ludox HS-40 as Si source, and KOH, along with (diDABCO-C*n*)Br_2 (*n* = 7–10) as SDAs for the crystallisation of STA-30. The general gel composition used in the previous chapter was 0.03–0.05 Al_2O_3 : 1.0 SiO_2 : 0.09–0.13 (diDABCO_C8)Br_2 : 0.06–0.12 KOH : 0.4 TXAOH : 20 H_2O. In this section, some further

variations to this gel composition will be discussed for assessing how some changes in the SDAs can impact the properties of the product.

Other Inorganic SDAs: Li, Cs, Sr

Gel composition for Li/Sr experiments: 0.4 TPAOH : 0.04 Al_2O_3 : 1.00 SiO_2 : 0.05 KOH : 0.06 $Sr(NO_3)_2$ or $LiNO_3$: 0.03 (diDABCO-C8)$(OH)_2$: 0.1 (diDABCO-C8)Br_2 : 20.3 H_2O.

The addition of both Li^+ or Sr^{2+}, alongside K^+, led to the crystallisation of STA-30. The increased background in the PXRD patterns (Figure 4.1) is due to some undissolved silica that appears in the SEM images as well. The images also show that these cations do not have a large impact on the morphology of the crystallites, as both zeolites exhibit the usual rice–grain shaped crystallites observed for diDABCO-C8 templated STA-30 (Appendix Figure A4.1). Most notably, the Sr^{2+} and the Li^+ appear to be incorporated into the materials, as EDS reveals lower levels of K^+ in both samples and the presence of Sr^{2+} (data in Table 4.1). Due to its light element nature, it is not possible to identify Li by EDS, but it is implied that it is found as an extra–framework cation due to decreased levels of K^+, compared to other diDABCO-C8-STA-30 samples that contained ~0.6–0.7 K/Al.

Gel composition for Cs experiments: 0.4 TPAOH : 0.04–0.06 Al_2O_3 : 1.00 SiO_2 : *a* KOH : *b* CsOH : 0.1 (diDABCO-C8)Br_2 : 20.2–20.4 H_2O. $a + b = 0.08$, apart from the synthesis where Cs : K = 1 : 0.5, where $a + b = 0.12$.

CsOH was easier to incorporate into the gel from a solubility standpoint, so a study of the Cs : K ratio was undertaken to understand whether Cs^+ could be templating *can* cages instead of K^+, as had been previously possible in zeolite CAN[5]. However, it was found that the synthesis must contain more K^+ than Cs^+ to crystallise pure STA-30, otherwise the products are dense phases, amorphous materials or potentially aluminosilicate EAB (Figure 4.1, right). All STA-30 products contained lower levels of K^+ and Cs^+ was also present, as shown by EDS. In some of the syntheses, it was found that spherical crystallites could form, which was a novel crystallite shape for STA-30 (Appendix Figure A4.1). Despite the fact that the incorporation of Cs^+ as extra–framework cations was successful, it was found that upon ion–exchange with NH_4Cl, it was possible to remove them and retain the expected K^+ levels that have been previously demonstrated to template the *can* cages of the SWY framework. This observation and the inability of Cs^+ to crystallise STA-30 when it was the dominant ISDA component in

the gel, led to the conclusion that this is not a viable route for the inclusion of Cs^+ in the *can* cages.

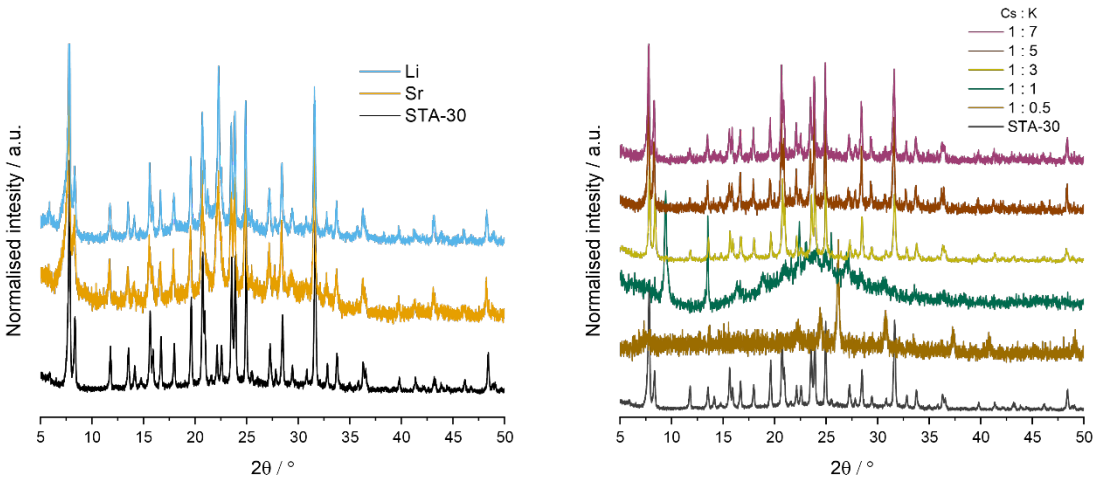

Figure 4.1 Comparison between STA-30 experimental pattern with other products synthesised from gels that contained K^+, as well as Sr^{2+} or Li^+ (left) and Cs^+ in various ratios (right).

Table 4.1 Compositional analysis by EDS of STA-30 samples prepared with Sr^{2+}, Li^+, and Cs^+, in addition to K^+.

Sample	Si/Al	K/Al	Others
Sr-STA-30	11.5	0.3	Sr/Al = 0.1
Li-STA-30	6.6	0.5	–
Cs-1:3-STA-30	5.8	0.4	Cs/Al = 0.2
Cs-1:5-STA-30	6.4	0.5	Cs/Al = 0.2
Cs-1:7-STA-30	6.1	0.5	Cs/Al = 0.2

Organic SDAs

IN–SITU SYNTHESIS OF OSDA

In the previous chapter, it was explored how the different lengths of the polymethylene chains connecting the bulky DABCO units affect the SDA capability of the organic molecule at a given gel composition. It had previously been reported for ERI[6] and tested in other parallel work on ERI in this project that it was possible to synthesise the OSDA *in–situ* in the CDM type approach by adding the OSDA precursors rather the salt or hydroxide form of the organic cation (see Chapter 5 for details). It was of interest to see if this approach can be extended to the synthesis of STA-30 without any impact on the

product crystallised from the gel, as the lack of need for the pre–synthesis of the OSDA implies cost reductions and a greener synthesis.

STA-30 syntheses with the precursors for (diDABCO-C8)Br_2 and (diDABCO-C10)Br_2 were attempted. The precursors DABCO, 1,8–dibromooctane or 1,10-dibromodecane were used in a gel composition with molar ratios 0.4 TPAOH : 0.04 Al_2O_3 : 1.00 SiO_2 : 0.1 KOH : 0.25/0.29 DABCO : 0.12/0.14 1,8–dibromooctane/1,10-dibromodecane: 20.4 H_2O. The syntheses were successful, based on the PXRD patterns of the products (Figures 4.2 and 4.3), even in the case of diDABCO-C10-STA-30 which was shown to be a less effective OSDA for STA-30. The as–made products formed from the *in–situ* OSDA resembled those obtained from pre–synthesised OSDA, showing that this is a viable route for zeolite synthesis. Furthermore, the crystal morphology and the stability of the material was not impacted negatively, and the composition did not change: EDS indicated Si/Al of 6.4–6.6 and K/Al = 0.7. It is thought that the reaction between the OSDA precursors occurs as the temperature of the gel increases and the immiscible dibromoalkane is more likely to react with the dissolved DABCO.

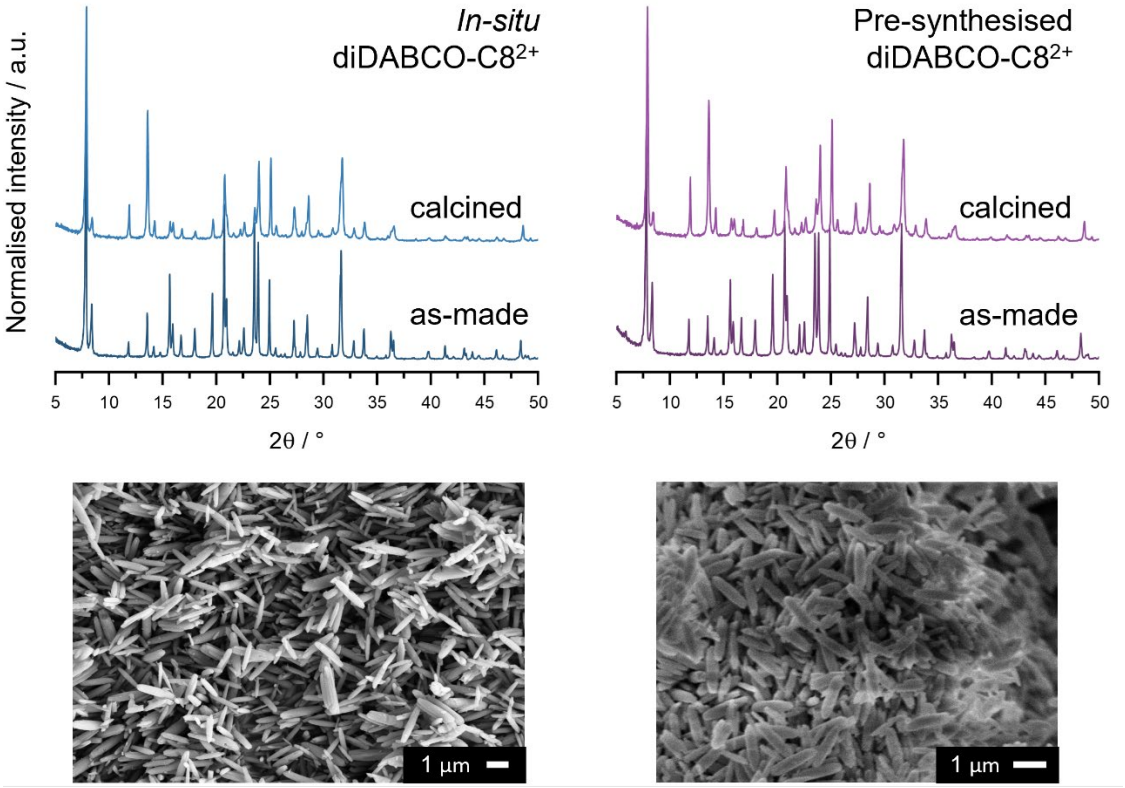

Figure 4.2 PXRD patterns of STA-30 zeolites in as–made and calcined forms synthesised from diDABCO-C8^{2+} precursors and pre-synthesised OSDA (top). SEM images of the STA-30 samples from both routes (bottom).

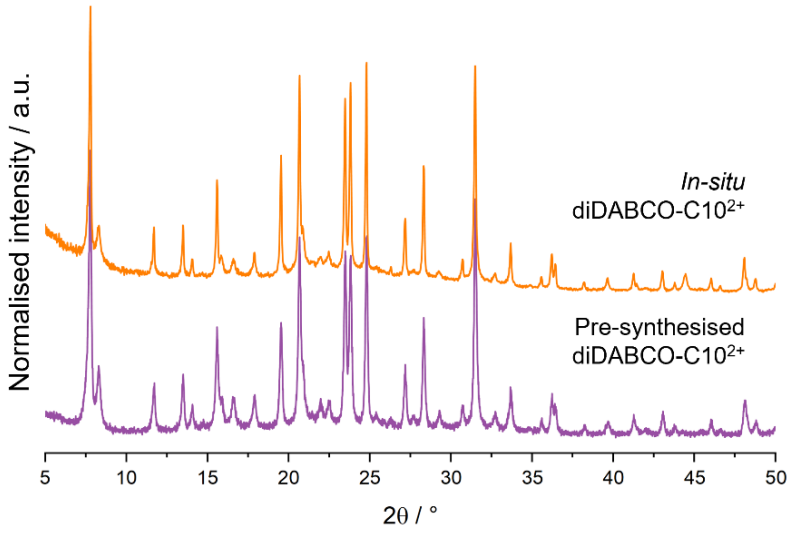

Figure 4.3 PXRD patterns of STA-30 zeolites synthesised from diDABCO-C10^{2+} precursors and pre–synthesised cations.

BEYOND DIDABCO BASED OSDAS

In the exploration of possible causes for increased level of SiOH defects, it was of interest to find an alternative to the DABCO–based OSDA to study the impact of the lone pair of the terminal N on the defect content of the zeolite. A closely related molecule to DABCO is quinuclidine (abbreviated Quin), which has a C–H group replacing one of the N in the DABCO unit (Figure 4.4). Thus, (diQuin-C8)Br_2 was synthesised (Appendix Figure A4.2 for details) and used as the crystallisation OSDA in CDM type syntheses. Computational modelling showed that the diQuin-C8^{2+} molecule would be a good fit in the *swy* cage of the SWY topology, as can be seen in Figure 4.5. However, the predicted binding energy was slightly less favourable for two cations of diQuin-C8^{2+} (-92.05 kJ mol^{-1}) compared to two cations of diDABCO-C8^{2+} (-95.39 kJ mol^{-1}) loaded into the SWY framework.

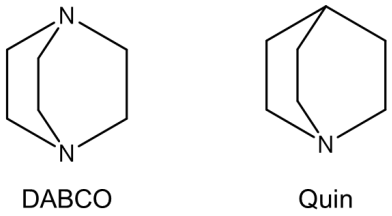

Figure 4.4 Comparison of 1,4-diazabicyclo[2.2.2]octane (DABCO) and quinuclidine (Quin) molecules.

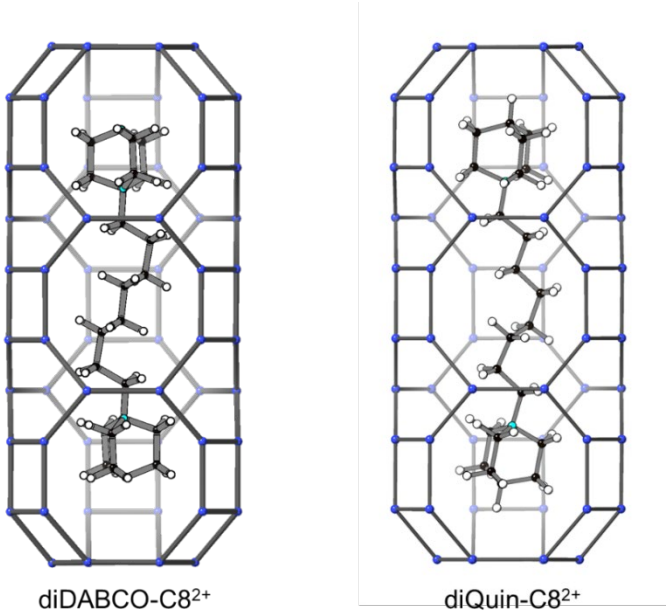

Figure 4.5 Fit of diDABCO-C8^{2+} and diQuin-C8^{2+} into a *swy* cage, cut–out from a SWY unit cell which was loaded with 2 OSDA and geometry optimised using COMPASS II.

Nevertheless, the incorporation of the (diQuin-C8)Br_2 into the synthetic conditions used for the preparation of diDABCO-C8-STA-30 was achieved without the need for further optimisation, leading to the crystallisation of phase pure crystalline STA-30 (Figure 4.6, left). At KOH levels in the gel around those routinely used for STA-30 (~0.1 KOH / SiO_2 mol), the crystallite morphology of diQuin-C8-STA-30 resembled rounded cylinders ~1 µm long and 0.4–0.5 µm wide (Figure 4.6, red frame on the right), which is a slightly different morphology from the rice grain crystals of diDABCO-C8-STA-30 that were more tapered. Doubling the K^+ levels in the gel had the effect of changing the morphology of diQuin-C8-STA-30 to hexagonal prisms 1–2.5 µm in length (L) and 0.3–0.9 µm in width (W), maintaining an aspect ratio of 3–5 L/W (Figure 4.6, blue frame on the right). The crystallisation of STA-30 in this shape is in line with its hexagonal symmetry. Conversely, when the same levels of K^+ were trialled in the CDM synthesis of diDABCO-C8-STA-30, needle like crystals (Appendix Figure A4.3) were obtained, which proves again the increased drive for the crystal growth in the *c* direction, but at the same time it shows that the small difference in OSDA has a large impact on the crystallisation of the zeolite.

The amount of K^+ also influenced the composition in terms of Al and K contents in the product STA-30. Thus, the lower alkalinity in the gel (0.1 KOH / SiO_2 mol) led to a higher Si/Al (6.2) and a lower K/Al (0.6) in the diQuin-C8-STA-30, compared to Si/Al=5.7 and K/Al=0.8 in the zeolite crystallised from the higher alkalinity gel. For ease of reference, the products of syntheses gels with KOH/ SiO_2=0.1 will be referred to as lowK-diQuin-

C8-STA-30 and the products of syntheses gels with KOH/ SiO_2=0.2 will be referred to as highK-diQuin-C8-STA-30.

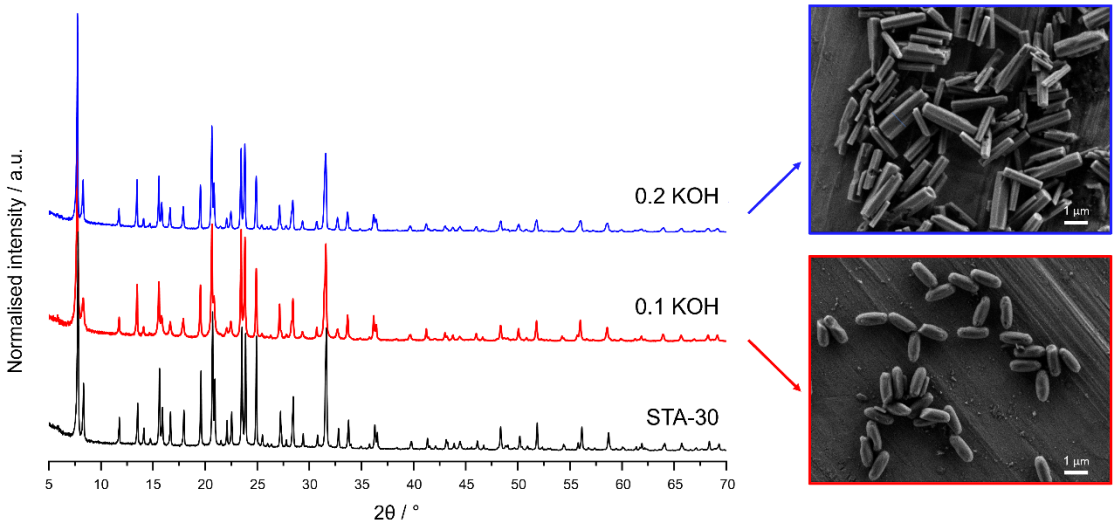

Figure 4.6 PXRD patterns (red and blue) of as–prepared zeolites synthesised from the gel composition 0.4 TPAOH : 0.05 Al_2O_3 : 1.0 SiO_2 : 0.16 (diQuin-C8)Br_2 : *x* KOH : 20 H_2O, where *x* is annotated on the figure. The patterns are compared to a PXRD pattern of STA-30 synthesised with diDABCO-$C8^{2+}$.

Further studies were conducted to understand how the change in OSDA impacted the STA-30 zeolite synthesised. Activating both lowK- and highK-diQuin-C8-STA-30 through ion–exchange with 10% NH_4Cl aq. sol. at 358 K led to stable crystalline activated forms with similar final K/Al levels (0.2) to those obtained in H-forms of diDABCO-C8-STA-30. The PXRD patterns of the materials through different stages of the activating procedure are presented in Figure 4.7. Some differences can be noticed between the two series of patterns, mainly in the background of the PXRD patterns and the peak widths. LowK-diQuin-C8-STA-30 patterns present both an increased background and broader peaks compared to the highK- counterpart. This indicates that the highK-diQuin-C8-STA-30 possesses a greater degree of crystallinity, which motivated continuing the in–depth characterisation of this diQuin-C8-STA-30. Furthermore, no significant differences are observed in their adsorption behaviour (Figure 4.8), which shows that the OSDA plays a stronger role than K/Al in directing the type of microporosity found in STA-30 zeolites, as will be discussed later in this chapter.

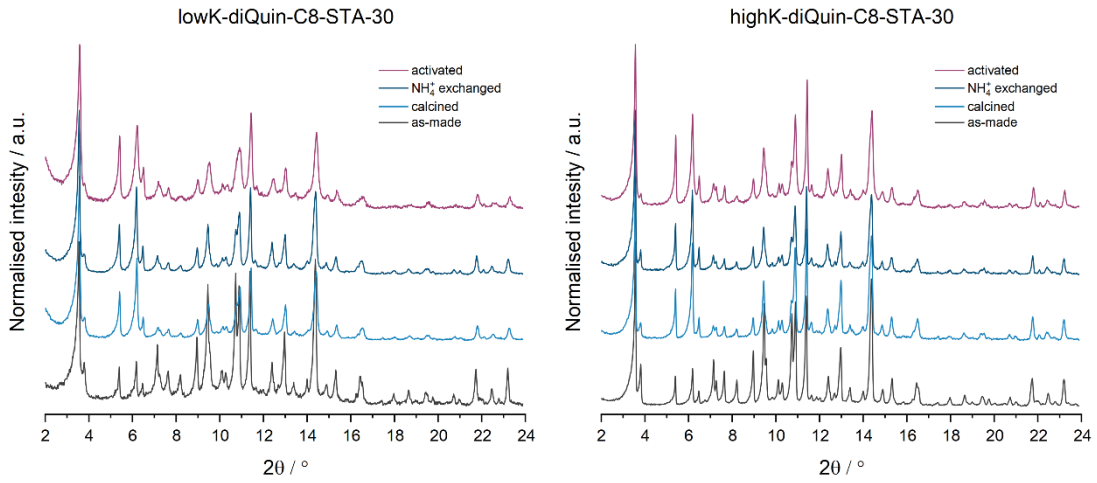

Figure 4.7 Comparison of PXRD patterns of lowK- and high-K-diQuin-C8-STA-30 in as–made, calcined, NH_4^+, and activated forms. The patters were collected with Mo $K_{\alpha1}$ radiation.

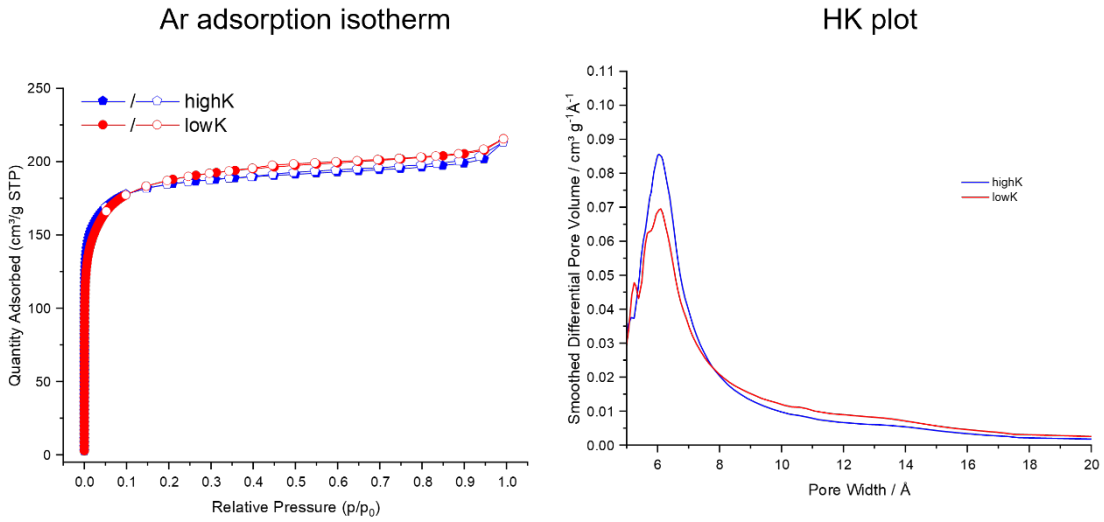

Figure 4.8 (Left) Ar adsorption isotherms at 87 K collected on the highK– and lowK–diQuin-C8-STA-30 activated zeolites. (Right) HK plots derived from the Ar adsorption data.

The inclusion of diQuin-C8^{2+} into the framework was confirmed by ^{13}C CP MAS NMR spectroscopy, which is shown in Figure 4.9 along with the assignments of the corresponding C environments in the OSDA. It is clear that no TPA$^+$ is present in this as–made material due to the lack of characteristic peaks at 10–16 ppm or 60 ppm. This confirms the role of TPAOH as mineraliser in the synthesis, rather than OSDA. Notably, there is no splitting in any of the peaks in this spectrum, which again sets diQuin-C8-STA-30 apart from diDABCO-C8-STA-30 again. This will be further explored in the 'Characterisation of selected samples' section of this chapter.

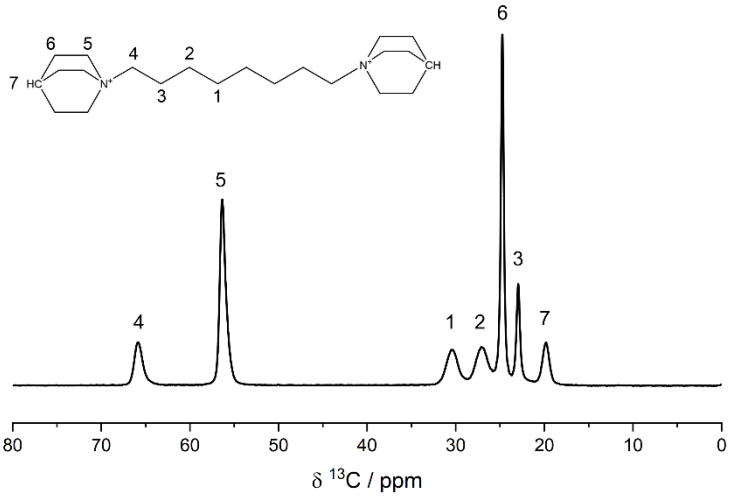

Figure 4.9 ^{13}C CP MAS NMR spectrum of diQuin-C8-STA-30.

The amount of (diQuin-C8)Br_2 could also be reduced to 0.06 (diQuin-C8)Br_2 / mol SiO_2 without impacting the physicochemical properties of the zeolite crystallised based on PXRD, EDS and SEM analysis. This was desirable because of the increased cost per g of OSDA (reagents cost ~£27 / g of (diQuin-C8)Br_2 and ~£1 / g of (diDABCO-C8)Br_2 for the preparation of the two OSDAs on a small scale in–house).[7] All syntheses were tested for repeatability and it was found that STA-30 zeolites of the same phase purity and composition could be prepared, which proves that this is a viable route to a new type of STA-30.

Hydrothermal syntheses

As mentioned in the introduction to this chapter, it was desirable to design new synthetic pathways for STA-30 beyond CDM to assess whether the intricacies introduced by the low–charge density/high–charge density balance and the aging of the aluminosilicate gel were involved in the development of the silanols observed.

The aging step was removed from the preparation of the synthesis mixture normally used in the CDM approach. The aluminosilicate gel was allowed to stir for a few hours before the addition of SDAs instead. Both TPAOH and (diDABCO-C8)$(OH)_2$ were tested as mineralisers, while maintaining the hydroxyl levels constant. The PXRD patterns below (Figure 4.10) show that it is not necessary to age the aluminosilicate gel to obtain STA-30, which is an indication that the CDM step is not the key feature that enables the crystallisation of SWY from these components. Also, these experiments proved again that TPAOH played no role in the structure direction of SWY, but merely acted as a

mineraliser since replacing it had no impact on the phase obtained. Even the composition was unaffected, with the zeolites obtained having Si/Al of 6.3–6.5 and K/Al 0.5–0.6. Although this confirms that the CDM step is not required, the PXRD patterns exhibit a slight amorphous background, which indicates that, under the same conditions or even after longer crystallisation times, the 'hydrothermal' approach is not as effective at crystallising purely crystalline STA-30 zeolites.

It was of interest to remove the effect of TPAOH as a factor from the assessment of gel components that might impact the amount of SiOH in the final product, so further studies on the hydrothermal approach focused on the use of (diDABCO-C8)$(OH)_2$ as a mineraliser. The stability of the activated form was satisfactory (Figure 4.11) so further studies into the optimisation of the synthesis were undertaken. Ultimately, the goal was to find the optimal parameters for scale–up, so the gel composition was adjusted for the use of $Al(OH)_3$ which meant the increase of Al_2O_3 content to 0.06 Al_2O_3 / 1 mol SiO_2 to compensate for the lower reactivity observed previously. It was found that this was a highly effective approach and the synthesis could be performed on a large scale. The complete characterisation of the zeolite synthesised in this manner will be discussed later in the chapter.

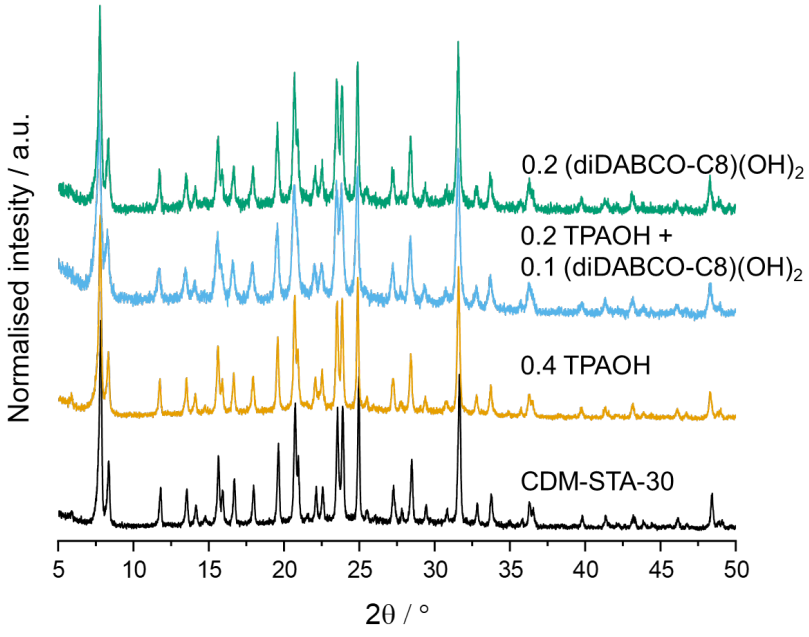

Figure 4.10 PXRD patterns of zeolite products from hydrothermal syntheses (with no aging step) with different mineraliser. The gel composition was *x* TPAOH : *y* (diDABCO-C8)$(OH)_2$: 0.04 Al_2O_3 : 1.0 SiO_2 : 0.1 (diDABCO-C8)Br_2 : 0.1 KOH : 21 H_2O (crystallised at 408–413 K for 5 days with tumbling at 60 rpm).

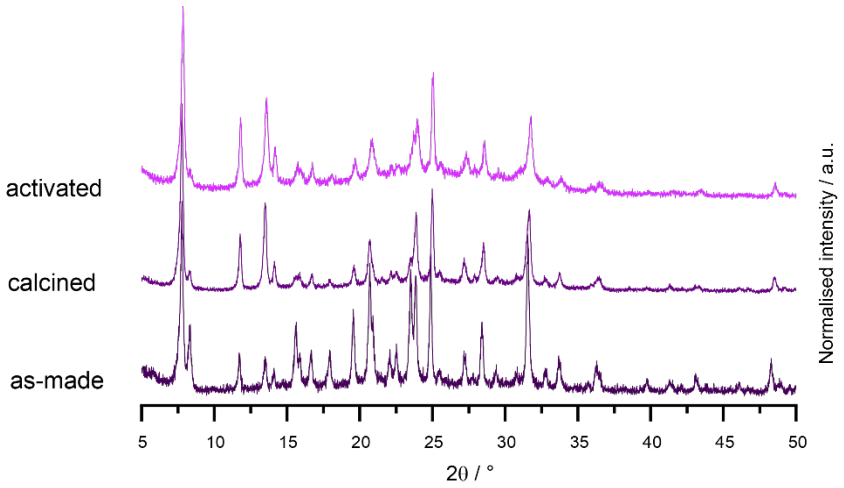

Figure 4.11 PXRD patterns of diDABCO-C8-STA-30 zeolite prepared through a hydrothermal approach in as–made, calcined and activated forms.

Crystallisation kinetics of CDM vs. hydrothermal syntheses

During the optimisation process for the CDM and hydrothermal approaches, another parameter considered was the minimum amount of time necessary for the crystallisation of STA-30 to maximise efficiency. While in general, 5 days were allowed for crystallisation to account for variations in the gel components that might slow down the reaction, for scaling–up purposes it was beneficial to know how fast different approaches are.

For CDM, the crystallisation was monitored over 5 days, at 408 K, for the gel composition 0.4 TPAOH : 0.04 Al_2O_3 : 1.00 SiO_2 : 0.07 KOH : 0.13 (diDABCO-C8)Br_2 : 20.3 H_2O, in which either Al(O-*i*-Pr)$_3$ or $Al(OH)_3$ were used as the Al sources. The collections of PXRD patterns in Figure 4.12 show that the crystallisation is complete after 48 hours for STA-30 zeolites prepared with Al(O-*i*-Pr)$_3$ and it is complete after 72 hours for the zeolites prepared from $Al(OH)_3$. Once the PXRD showed a fully crystalline STA-30, the yields and compositions (Si, Al and K) remained constant.

On the other hand, for the conventional hydrothermal preparation, the crystallisation was slower. The products were amorphous even after 72 hours at 408 K and the crystallisation was complete only after 120 hours (PXRD patterns in Figure 4.13). This shows that even if the two approaches yield zeolite STA-30, the CDM approach occurs faster than the conventional hydrothermal one. This is most likely due to the presence of precursor species in the aged CDM solution that can interact more readily with SDAs and lead to faster nucleation. More details about the influence of the CDM step will be discussed in Chapter 6.

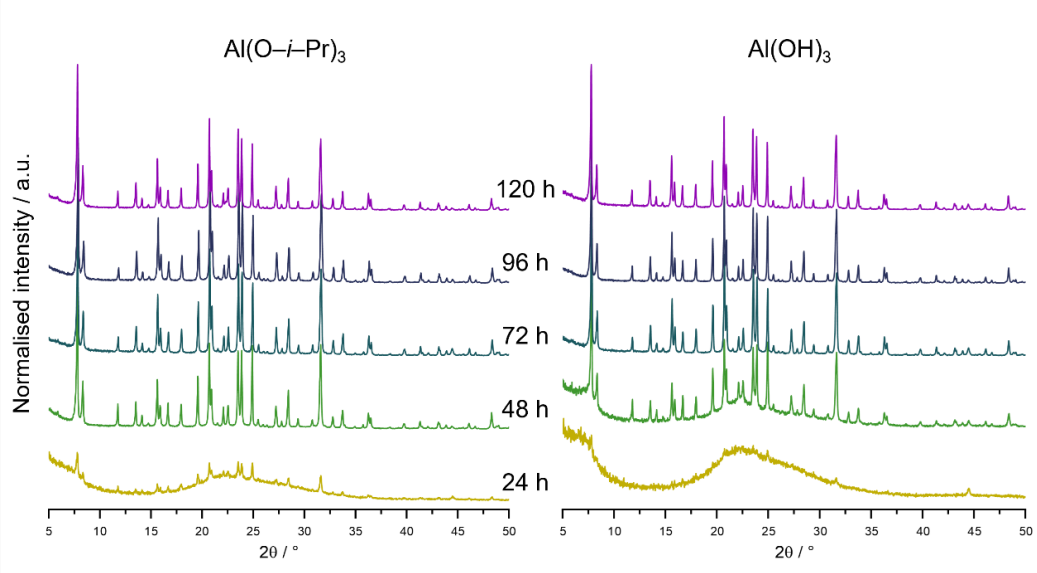

Figure 4.12 PXRD patterns of solids collected between 24 hours and 120 hours from CDM type syntheses, where Al isopropoxide (left) or Al hydroxide (right) were used as the Al source.

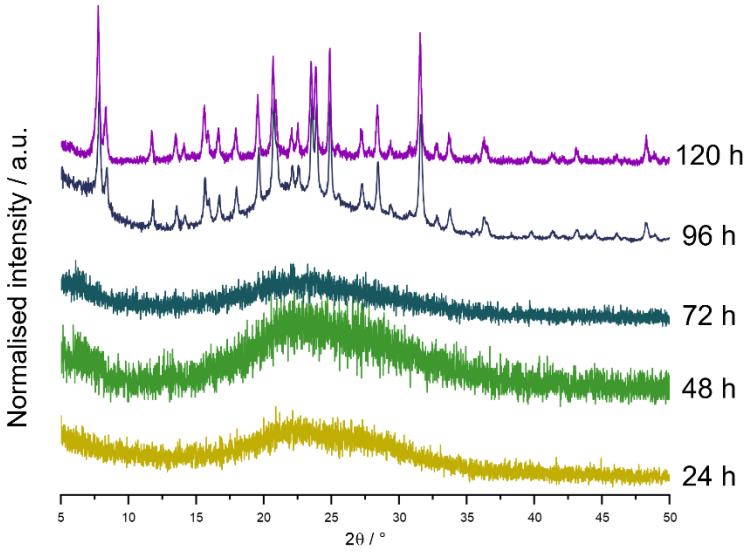

Figure 4.13 PXRD patterns of solids collected between 24 hours and 120 hours from hydrothermal (no aging) syntheses.

Partial IZC syntheses

The use of zeolite Y (aluminosilicate FAU) as the Al source has been widely applied in zeolite synthesis and it provides various advantages over the use of non–zeolitic Al and Si sources. Some of the advantages consist of faster syntheses times, use of different OSDAs or the access to new Si/Al ranges in the crystallised product.[8] Thus, it was of

interest to understand how this route could be applied to the synthesis of STA–30 and what impact it would have on the properties of the zeolite product.

The synthesis design started with the gel composition used in the 'hydrothermal' approach with the use of the 20% aq. sol. of (diDABCO-C8)$(OH)_2$ as the mineraliser. The Al source was chosen to be CBV 712, which is a commercial form of zeolite Y with Si/Al of 6, in NH_4^+–form, available through Zeolyst (measured PXRD pattern and crystallite morphology in Appendix Figure A4.4). This was chosen as only a small amount of Ludox HS-40 had to be added to achieve similar Si/Al ratios in the gel as found in the other CDM or hydrothermal gel compositions. Since CBV 712 is not the sole source of framework cations in the synthesis, the approach was called 'partial IZC' rather than simply 'IZC'. The only other gel components that were found to require optimisation were the levels of K^+ and the synthesis temperature.

The PXRD patterns of a selection of the syntheses attempts during the optimisation process can be found in Figure 4.14. In terms of synthesis temperature, it was found that the IZC process is more effective at higher crystallisation temperatures. As it can be seen in the PXRD pattern of the sample synthesised at 408 K, zeolite Y was not fully dissolved in the synthesis, which is apparent because of the peak at 6.3°. Increasing the temperature to 418 K improved the dissolution, but impurities of zeolite beta were obtained even after a prolonged synthesis period. Increasing the temperature to 433 K accelerated the complete crystallisation of STA-30, bringing the synthesis times down to 2 days, which proves the usefulness of the method in terms of speed over the conventional hydrothermal approach. The beta (*BEA, broad peak ~7° and sharp peak ~22.5°) impurities could be removed by increasing the level of KOH above 0.20 KOH / 1 mol SiO_2 in the gel.

The SEM images of the STA-30 zeolites synthesised via this partial IZC route revealed a new morphology for this type of zeolite. The shape of the crystallites is the same as that of matchsticks 1–3 μm long (Figure 4.15), that are bunched up together and seem to be growing radially from the centre of the crystals. In terms of composition, the Si/Al ratio is that found in other STA-30 zeolites (6–7). The incorporated K^+ levels matched those measured in other as–made diDABCO-C8-STA-30 zeolites.

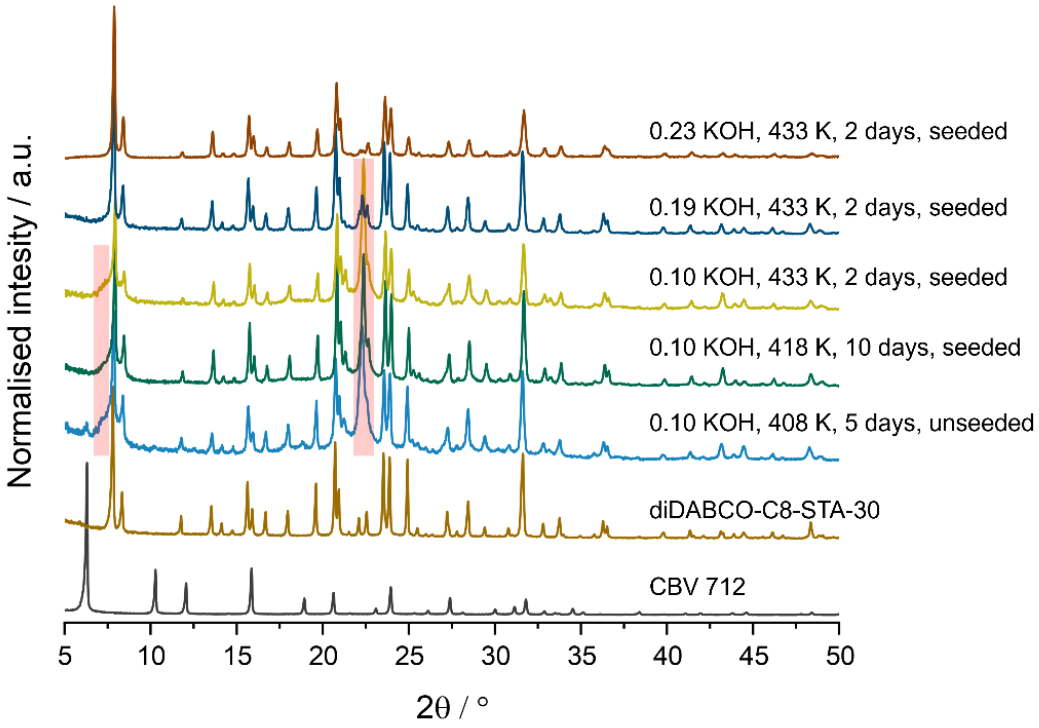

Figure 4.14 PXRD patterns of products of partial IZC syntheses showing the evolution of the development of optimal gel composition and crystallisation conditions. These products are compared with the PXRD pattern of a CDM STA-30 sample (black). The gel composition used was 0.2 (diDABCO-C8)$(OH)_2$: 0.06 Al_2O_3 : 1.0 SiO_2 : 0.08 (diDABCO-C8)Br_2 : x KOH : 22 H_2O. Impurities are highlighted with red areas.

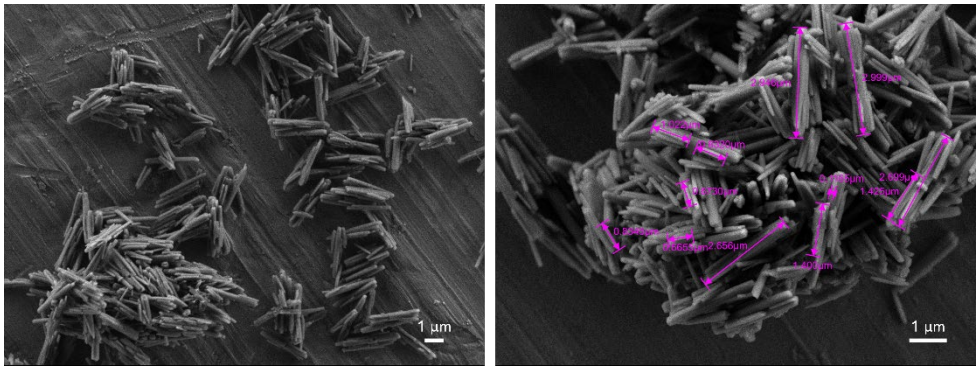

Figure 4.15 SEM images of the zeolite diDABCO-C8-STA-30 synthesised through the optimised partial IZC synthesis.

The optimised synthesis was reproducible on larger scales (tested up to 1.5 L), achieving similar crystallite morphologies and compositions every time. It was also possible to activate the STA-30 zeolite prepared this way and remove the extra–framework cations outside the *can* cages through ion-exchange at 348 K. The PXRD patterns for the medium scale as–prepared material and its activated counterpart can be found in Figure

4.16. The complete characterisation of the STA-30 zeolite prepared this way can be found later in this chapter.

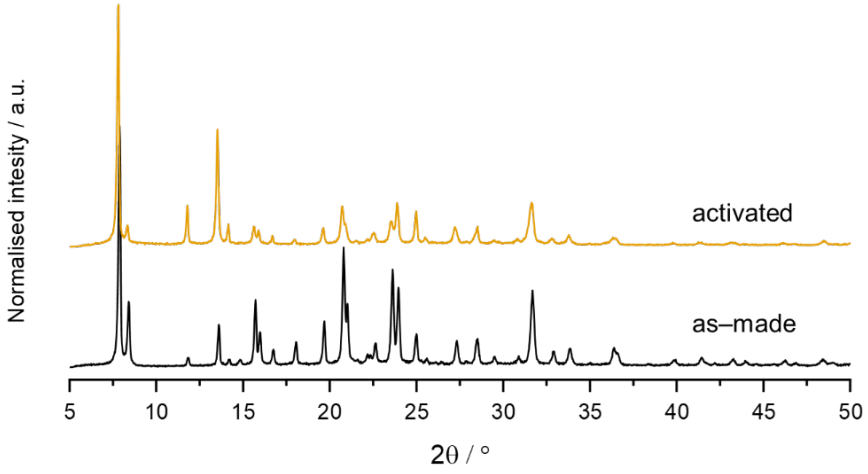

Figure 4.16 PXRD pattens of as–prepared and activated diDABCO-C8-STA-30 prepared through partial IZC at medium scale.

Effect of seeding

Seeding was found to be essential for obtaining STA-30 in the designed gel, without any impurities. Without any seeds, the crystallisation of STA-30 is not favoured and other phases are obtained, their type depending on the K^+ content in the gel. The PXRD patterns below (Figure 4.17) show that either zeolite beta[9] or sanidine (potassium feldspar)[10] crystallise instead, at the two K^+ levels tested.

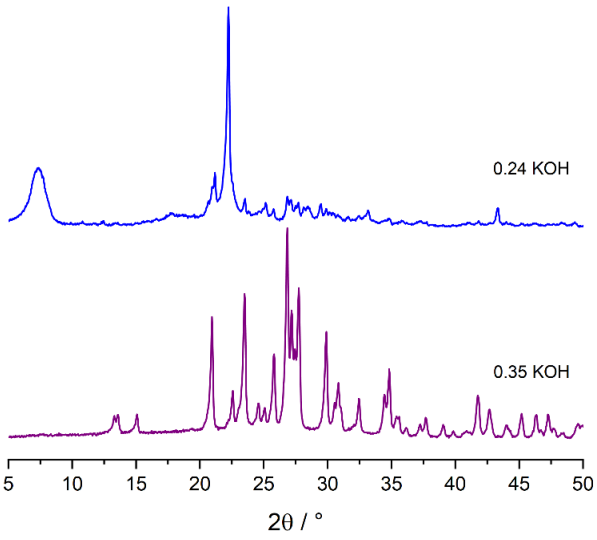

Figure 4.17 PXRD patterns of materials obtained from un–seeded partial IZC syntheses at 433 K, with the gel composition 0.2 $(diDABCO\text{-}C8)(OH)_2$: 0.06 Al_2O_3 : 1.0 SiO_2 : 0.08 $(diDABCO\text{-}C8)Br_2$: 0.24/0.35 KOH : 22 H_2O.

Various as–made zeolites were also tested to analyse whether the crystallite shape of the STA-30 product can be controlled through the morphology of the seeds. The PXRD patterns of the seeds are compared with the products that they led to when introduced in 7.5 wt.% proportion in the (diDABCO-C8)$(OH)_2$ CBV 712/Ludox HS-40 gel. An interesting observation is the fact that diQuin-C8-STA-30 zeolite (red patterns in Figure 4.18) seem to not act as effective seeds under the same conditions as the diDABCO-C8-STA-30 zeolites. Even though STA-30 is obtained, other phases are present as well and the SEM images reveal 3 different types of crystals (Figure 4.19, 1st image). Further work would be required to design a gel suitable for this type of seeds. A possible explanation could be the smaller number of defects in this sample (characterisation discussed later in the chapter). However, a faulted zeolite SWY synthesised with diQuin-$C6^{2+}$ (blue patterns) leads to the crystallisation of pure STA-30 with the same matchstick morphology (Figure 4.19, 2nd image). The CsK-STA-30 (green patterns) leads to pure STA-30, but the crystals possess both the spherical morphology of the seeds and (mainly) the matchstick crystallite morphology (Figure 4.19, 3rd image). It was interesting to observe that aluminosilicate ERI (purple patterns) could also serve as effective seeds in the synthesis of STA-30, which is a different topology. Thus, if the role of the seed is to provide some building blocks during crystallisation, it is enough for the seed and the product to only have some building units in common, *can* and *d6r* in this case. It is more important for the gel to be able to break down the seeds and for the SDAs present to be able to template the new desired topology.

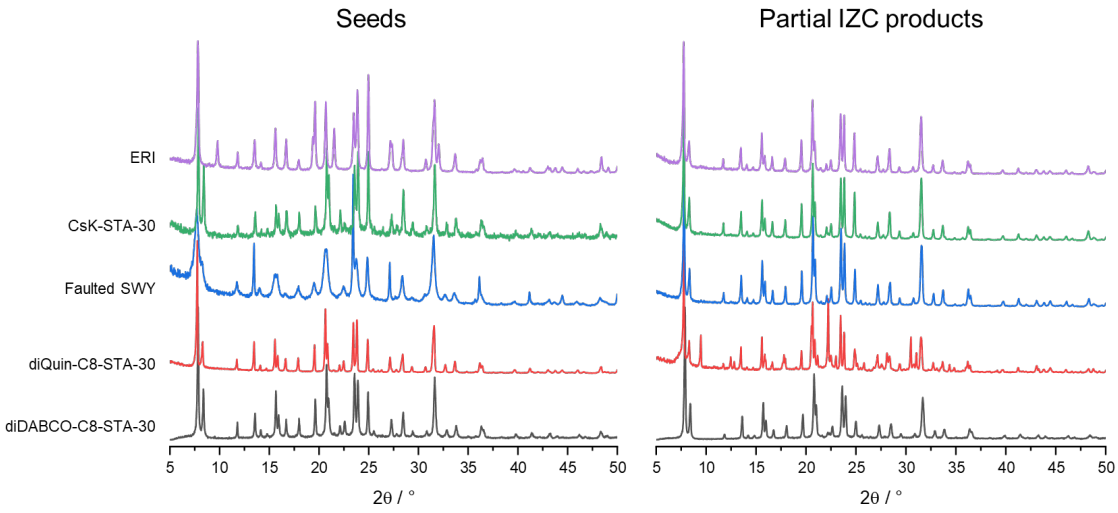

Figure 4.18 PXRD patterns of different seeds (left) used in the partial IZC approach (gel composition: 0.2 (diDABCO-C8)$(OH)_2$: 0.06 Al_2O_3 : 1.0 SiO_2 : 0.07 (diDABCO-C8)Br_2 : 0.25 KOH : 22 H_2O), and the product of the syntheses (right).

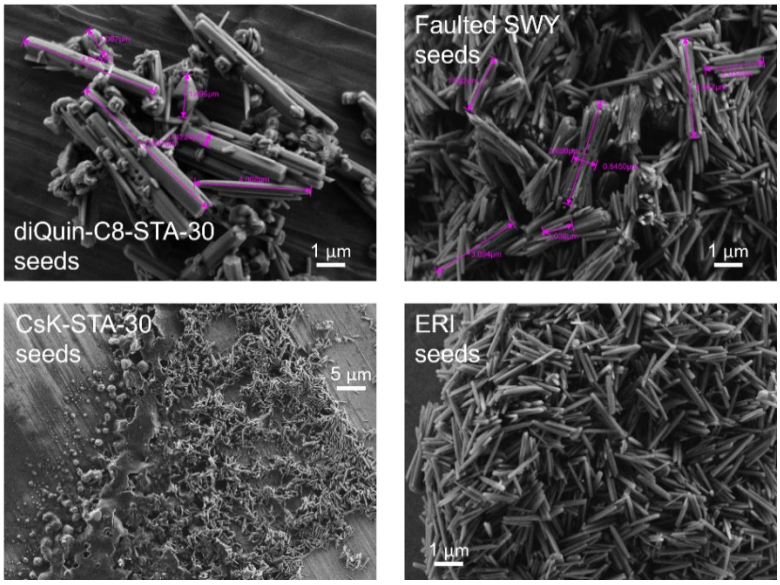

Figure 4.19 SEM images of materials synthesised through a partial IZC approach with different seeds.

Crystallisation kinetics of partial IZC

As other studies have shown, the synthesis time for crystallisation of STA-30 can be reduced by using a zeolitic source for T atoms. This is most likely due to the presence of precursor species that trigger the nucleation events much faster compared to 'conventional' gels.[8]

A closer look at the evolution of the solid product (Figure 4.20) after shorter amounts of heating shows that the commercial zeolite Y dissolves once the gel is heated under autogenous pressure. After only 2 hours at the crystallisation temperature, the FAU phase is no longer present and there is an increasing amount of zeolite STA-30. While there are only small amounts of impurities after 4 hours, the synthesis appears to be complete after 24 hours. The yields and composition also remain constant after 24 hours. (Figure 4.21)

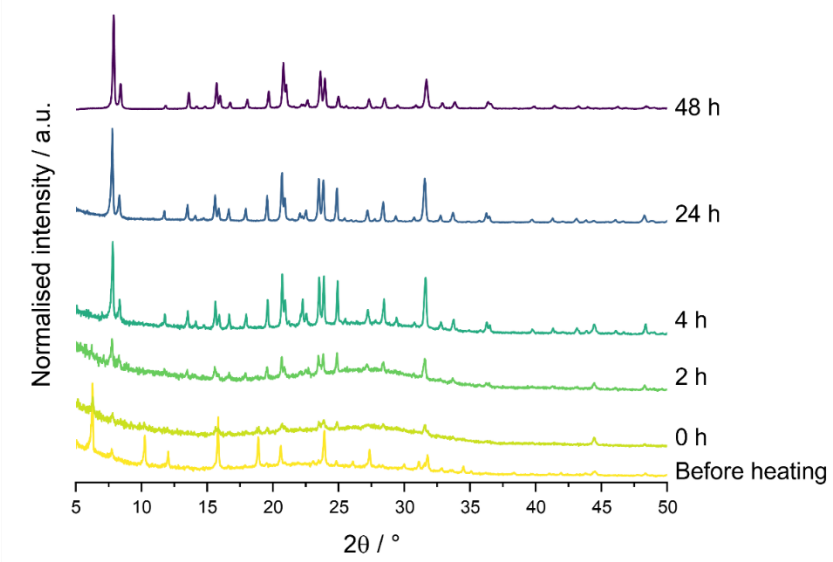

Figure 4.20 PXRD patterns of solids recovered from the partial IZC zeolite syntheses after variable durations of time at 433 K (gel composition: 0.2 (diDABCO-C8)$(OH)_2$: 0.06 Al_2O_3 : 1.0 SiO_2 : 0.07 (diDABCO-C8)Br_2 : 0.25 KOH : 22 H_2O).

The data points collected at the early stages of the synthesis (0–4 h in the graphs below) show that as soon as a high temperature is reached inside the autoclave, the dissolution of a large proportion of the seeds and zeolite Y occurs, leaving behind a more Al and K rich solid, which agrees with other studies on the dissolution stage during IZC.[8] The yields and compositional data show that nucleation and crystallisation occur within a few hours and more time steps would be required to discern clearer boundaries between stages. However, this designed synthesis provides the fastest route to zeolite STA-30 templated by diDABCO-$C8^{2+}$.

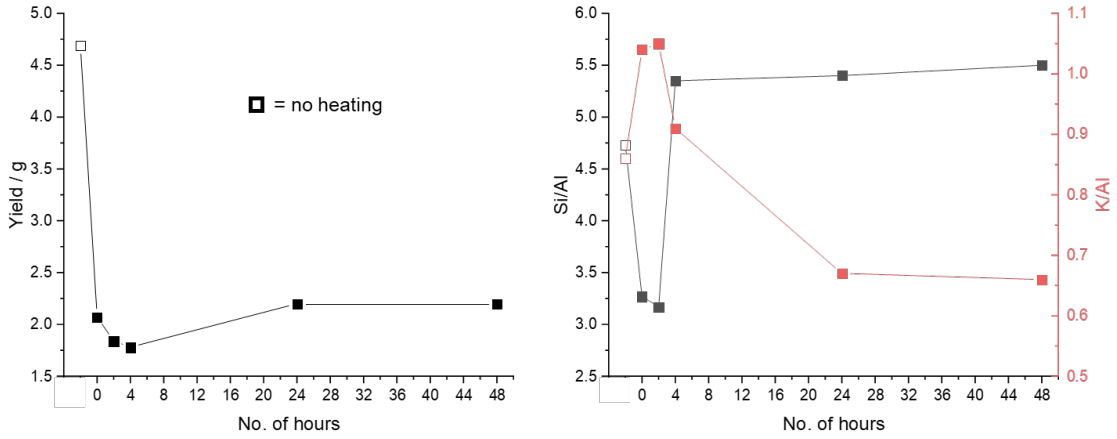

Figure 4.21 Amounts of solid recovered from crystallisation kinetics study of STA-30 through the partial IZC route (left) and the Si, Al and K composition of the solids (right).

Characterisation of selected samples

Selection of samples, their synthesis, and composition

Five different samples prepared through the main synthetic pathways to STA-30 have been analysed in depth using various techniques to test their microporosity, acidity and SiOH defect content. The pathways chosen to test the impact of the synthetic parameters on STA-30 were the CDM approach using TPAOH as mineraliser, the hydrothermal approach and the partial IZC approach, with the latter two using (diDABCO-C8)$(OH)_2$ as mineraliser. In the case of the CDM approach, the impact of different Al sources was also studied. Four samples were prepared with diDABCO-C8^{2+} as OSDA, and the fifth was prepared through a CDM type approach with diQuin-C8^{2+} as OSDA. The samples were coded based on their mineraliser source and Al source, apart from the diQuin-C8^{2+} sample. The codes are explained in Table 4.2.

The gel compositions are detailed in Table 4.3. It can be seen that there are minimal differences in molar contents of components. Higher amounts of K^+ were used in the case of OSDA_Y so as to avoid the crystallisation of secondary phases, while in the case of TPA_diQuin-C8, this was done to crystallise hexagonal prismatic crystallites.

Table 4.2 Codes for STA-30 zeolites analysed in–depth, with details on the synthesis approach, mineraliser, Al source and OSDA used.

Sample	Synthesis approach	Mineraliser	Al source	OSDA
TPA_AliPr	CDM	TPA^+	$Al(O\text{-}i\text{-}Pr)_3$	diDABCO-C8^{2+}
TPA_AlOH	CDM	TPA^+	$Al(OH)_3$	diDABCO-C8^{2+}
OSDA_AlOH	Hydro-thermal	(diDABCO-C8)$^{2+}$	$Al(OH)_3$	diDABCO-C8^{2+}
OSDA_Y	Partial IZC, seeded	(diDABCO-C8)$^{2+}$	CBV 712	diDABCO-C8^{2+}
TPA_diQuin-C8	CDM	TPA^+	$Al(O\text{-}i\text{-}Pr)_3$	diQuin-C8^{2+}

The scales at which these samples were prepared are different, which means that the mixing was different (tumbling at 60 rpm for PTFE–lined stainless steel autoclaves, mixing with a double pitched blade impeller for large scale). TPA_AliPr, TPA_AlOH and OSDA_AlOH were prepared on a 1500 mL scale, while OSDA_Y and TPA_diQuin-C8

samples were prepared in PTFE–lined stainless steel autoclaves with the volume of 125 mL and 50 mL, respectively. The crystallisation temperature for all syntheses was 408 K, apart from OSDA_Y which was crystallised at 433 K for the most optimal results.

The last two columns in the table below also show how the yields (either calculated with respect to full consumption of Al or wt.% Si reacted) are correlated with the method used and the Al source. Thus, the largest yield is for samples synthesised through a CDM approach with Al(O-*i*-Pr)$_3$ as Al source, regardless of OSDA or scale, followed by OSDA_AlOH, OSDA_Y and TPA_AlOH. The fact that the OSDA_AlOH has a better yield than TPA_AlOH shows that the mineraliser has an impact on the efficiency of the Al source in reacting with the Al. In this case, the higher charged diDABCO-C8^{2+} could aid the dissolution of Al(OH)$_3$ more effectively than the lower charge TPA$^+$. However, it is worth noting that the efficiency of Si incorporation is similar in all samples prepared through a CDM type approach, and it is much lower for the sample prepared with the hydrothermal approach with Al(OH)$_3$ and Ludox as T atom sources. The partial IZC approach has a lower Si incorporation efficiency compared to CDM, but it is still higher than the traditional hydrothermal approach.

Table 4.3 Gel compositions and yields of Si incorporated into the STA-30 zeolites synthesised through the various approaches studied in–depth.

Sample code	Molar ratio to SiO_2 in the gel[a]					Yield / %	Si used / %
	Mine-raliser	Al_2O_3	KOH	(OSDA)Br_2[b]	H_2O		
TPA_AliPr	0.4	0.04	0.09	0.06	20	100	49
TPA_AlOH	0.4	0.04	0.08	0.13	20	48	44
OSDA_AlOH	0.2	0.06	0.08	0.07	25	77	18
OSDA_Y[c]	0.2	0.06	0.23	0.07	21	75	37
TPA_diQuin-C8	0.4	0.05	0.19	0.06–0.16[d]	20	100	48

[a] All molar quantities as ratio to 1.0 SiO_2. [b] OSDA was diDABCO-C8^{2+}, unless specified otherwise. [c] TPA_AliPr or TPA_AlOH type samples were used as seeds, 7.5 wt.% calculated with respect to SiO_2 content. [d] OSDA used for this sample was diQuin-C8^{2+}.

The PXRD patterns of as–made and activated samples, along with their SEM images can be found in the Appendix Figure A4.5. The crystallite shapes and sizes are those discussed previously for each type of route, but they are summarised in Table 4.4 for ease of discussion, along with the Si/Al and K/Al ratios. The TGA data (Figure 4.22)

shows that for the samples prepared with diDABCO-C8^{2+}, the dry zeolite makes up a smaller proportion of the sample, compared to diQuin-C8^{2+}, which implies that the quantity of OSDA and H_2O is larger in the former.

Table 4.4 Characterisation of the five selected STA-30 samples, in terms of crystallite morphology and composition (*value measured on the activated form).

Sample code	Crystal Morphology	Size range / μm	Si/Al	K/Al
TPA_AliPr	Rice grain	0.8–1.4	5.9	0.6
TPA_AlOH	Rice grain	0.8–1.4	6.9	0.6
OSDA_AlOH	Rice grain	0.3–1.0	6.5	0.5
OSDA_Y	Match–stick rods	2.0–3.0	6.0*	0.6
TPA_diQuin-C8	Hexagonal prisms	1.0–2.5	6.0	0.8

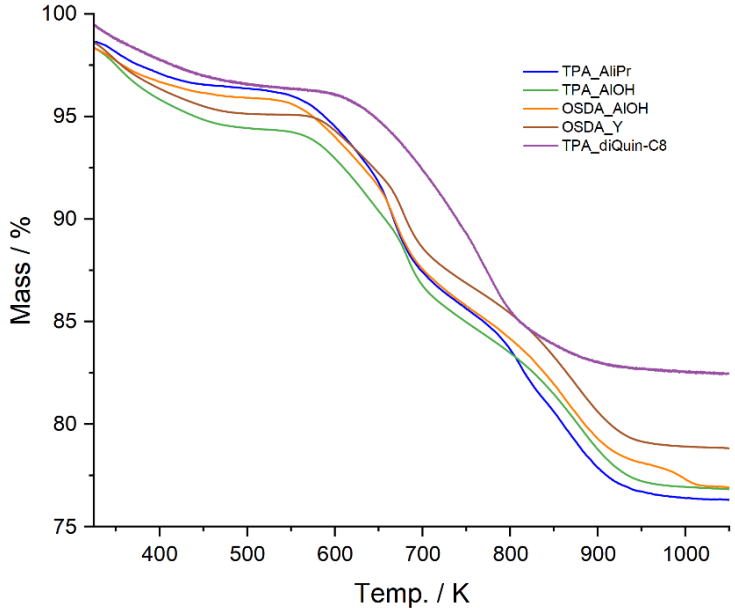

Figure 4.22 TGA mass loss curves of TPA_AliPr (blue), TPA_AlOH (green), OSDA_AlOH (orange), OSDA_Y (brown) and TPA_diQuin-C8 (purple).

CHN data (results in Table 4.5) measured on TPA_AliPr and TPA_diQuin-C8 confirm the observations made from TGA, showing that there is a smaller amount of OSDA in the STA-30 zeolite templated by diQuin-C8^{2+}. The C/N ratio from the CHN data match the identity of the OSDA used in the synthesis. The weight percentage of the mass loss due to OSDA was determined based on TGA and CHN results, which enable the calculation of the expected number of molecules of OSDA per unit cell of SWY. The results from TPA_diQuin-C8 show that all *swy* cages are expected to be templated by OSDA. The

calculated extra–framework cation amounts exceed those expected as (K^+ + 2 × diQuin-$C8^{2+}$)/Al is larger than 1, which indicates that there are potentially defects present in this sample. On the other hand, in the case of diDABCO-$C8^{2+}$, the calculated amount of OSDA per unit cell was 3, which exceeds the number of *swy* cages. This observation will be later explained through the additional features observed in diDABCO-C8-STA-30 zeolites.

Table 4.5 CHN results collected from two STA-30 samples synthesised through CDM with diDABCO-$C8^{2+}$ or diQuin-$C8^{2+}$ as OSDA, tabulated along with the calculated C/N ratio and amount of OSDA in one SWY unit cell calculated based on TGA results.

Sample	Formula OSDA	%C	%H	%N	C/N	Wt.% OSDA	OSDA / u.c.
TPA_AliPr	$C_{20}H_{40}N_4$	12.8	2.43	2.78	5.4	17.9	3
TPA_diQuin-C8	$C_{22}H_{42}N_2$	10.2	1.89	1.06	11.2	12.9	2

Impact of post–synthetic modification route

In addition to undergoing the classic ion–exchange procedure, TPA_AliPr was also activated by first being ion–exchanged with 1 M NH_4Cl solution until all accessible (outside the *can* cages) inorganic extra–framework cations were removed. It was found that the same 0.2 K/Al levels of exchange can be achieved despite the presence of the OSDA in the material, which is not removed either from the structure, based on the ^{13}C CP MAS NMR spectrum (Figure 4.23D) and TGA (Appendix Figure A4.6). This NH_4^+-exchanged sample was then calcined to remove both NH_3 and OSDA to obtain the H-form. This particular activated sample is denoted 'TPA_AliPr_EC' based on the fact that it was first exchanged (E) and then calcined (C).

Both activation routes yielded stable activated materials with similar microporosity, based on the crystallinity shown by their PXRD patterns and their Ar adsorption isotherms (Figure 4.23A and B). The Si environments are not impacted by the difference in activation route (^{29}Si NMR spectra, Figure 4.23C). However, the ^{27}Al NMR spectra show that the TPA_AliPr_EC sample contains more extra–framework Al compared to the sample activated through the 'conventional route'. Furthermore, there is no longer a clear set of peaks that can be attributed to framework octahedral Al, as is the case for the TPA_AliPr_H. The tetrahedral Al peak also broadens out for the TPA_AliPr_EC sample, which is another indication that there is a higher degree of disorder in this sample. The additional EFAl most likely leads to the blockage of some of the pores which explains the lower uptake observed in the Ar adsorption/desorption isotherms (Figure 4.23B). The

^{1}H NMR spectra show a relative decrease of ^{1}H from Si–O<u>H</u>–Al compared to Al<u>OH</u> and Si<u>OH</u> environments. The relative ratio of the different types of T–OH species is also reflected in the FTIR studies conducted on these samples (Figure 4.23D).

While repeatedly subjecting the zeolite to high temperatures during calcination events might seem detrimental to the structure, this study shows that the opposite effect occurs for this aluminosilicate zeolite templated by OSDAs. The initial calcination to remove the OSDA from cages leads to the formation of some Si–OH–Al groups that stabilise the calcined material. Then, the NH_4^+ that replaces K^+ in 8MRs of the calcined material confers further stabilisation to the Al atoms in the framework. Thus, the aluminosilicate framework has a better starting point for further loss of extra–frameworks cations and incorporation of more –OH groups. Consequently, all other STA-30 zeolites were activated through the [calcination]–[ion–exchange]–[calcination] route.

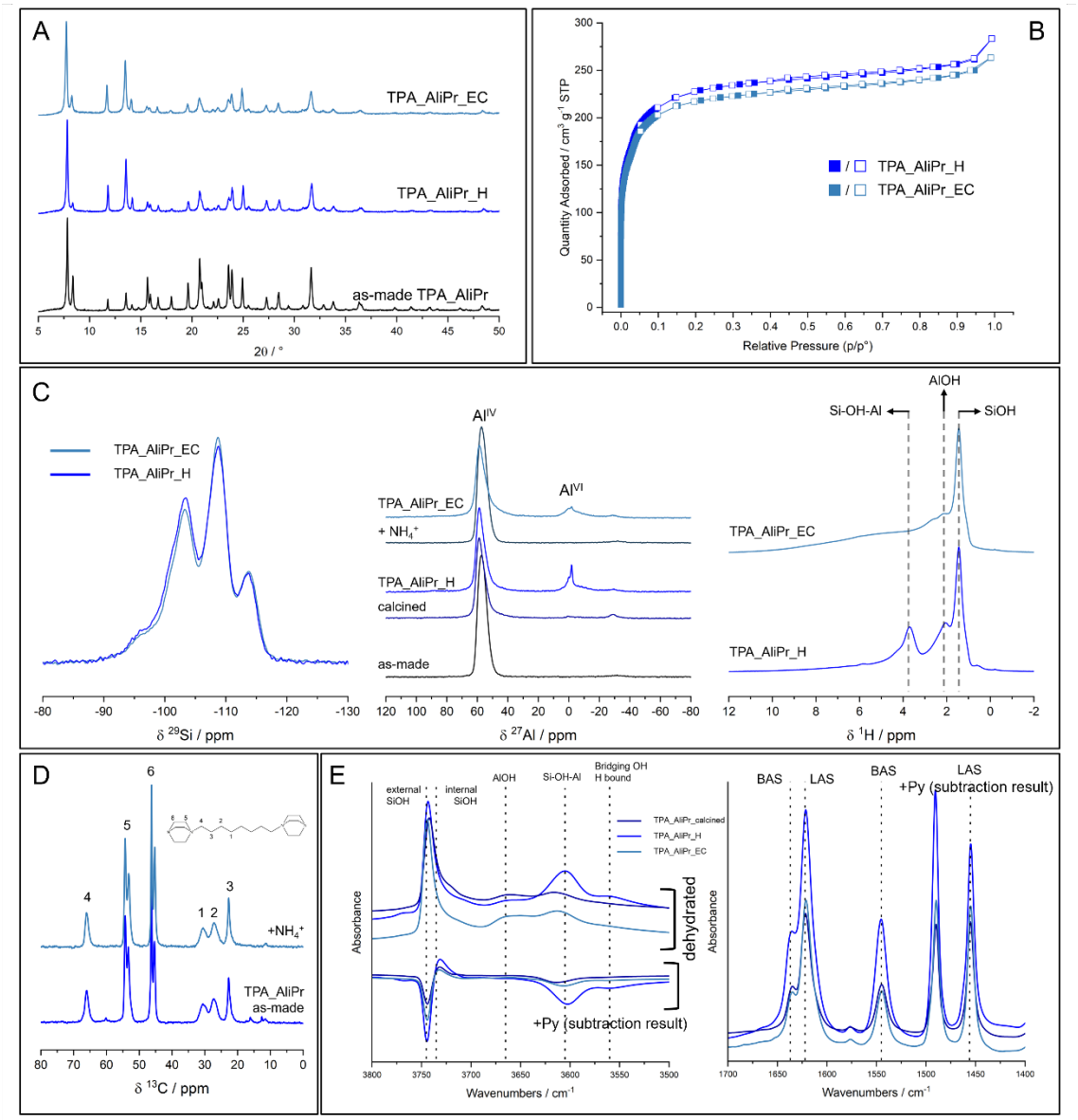

Figure 4.23 Characterisation of samples activated through different routes: (A) PXRD patterns; (B) Ar adsorption (whole symbols) and desorption (hollow symbols) isotherms at 88 K; (C) ^{29}Si (left), ^{27}Al (middle) and ^{1}H (right) MAS NMR spectra; (D) ^{13}C CP MAS NMR spectra; (E) FTIR spectra – SiOH region of spectra of dehydrated samples and difference spectra after pyridine adsorption at 473 K (left), BAS and LAS region of difference spectra after pyridine adsorption at 473 K (right).

Ar adsorption isotherms at 87 K

Ar adsorption was chosen as a technique for the characterisation of microporosity in STA-30 to eliminate any potential ambiguities introduced by the quadrupole moment of the N_2 molecules. The adsorption isotherms collected on activated samples (Figure 4.24), revealed that there are significant differences between the various STA-30 materials in terms of their microporosity. The activated STA-30 synthesised with (diQuin-

C8)Br_2 (TPA_diQuin-C8), has a lower uptake compared to the other activated samples (TPA_AliPr, TPA_AlOH, OSDA_AlOH and OSDA_Y — denoted diDABCO-C8_STA-30 as a group), which were synthesised with diDABCO-$C8^{2+}$. Another key difference is the step observed in the isotherms of diDABCO-C8_STA-30 materials around 0.05 p/p_0, which is better represented inset in Figure 4.24 on a log scale for relative pressure. TPA_diQuin-C8_H shows a typical Type I isotherm in the low relative pressure region, with no discernible step. These additional features in the isotherms indicate that there is an additional source of porosity in diDABCO-C8_STA-30 zeolites. This porosity is likely to be microporous considering that the isotherms overall still retain Type I shape, rather than Type IV, which is characteristic of a mesoporous material.

In the previous chapter, STA-30 was shown to have a higher N_2 uptake at 77 K compared to an aluminosilicate ERI material prepared in–house.[11] While some of the cages in the SWY and ERI frameworks are different, both materials should possess similar porosity as they are both 8MR ABC–6 topologies, with similar accessible volumes, so the difference could not be explained through accessible volume of the framework type. Indeed, the uptake of TPA_diQuin-C8_H is close to that of an activated aluminosilicate ERI sample prepared as a benchmark for comparison (Figure 4.25). The similarity between TPA_diQuin-C8_H and ERI_H further reinforces that the diDABCO-C8_STA-30 zeolites exhibit additional microporosity above that expected from their framework structure.

Additionally, there is some variation within the diDABCO-C8_STA-30 materials, which correlates with the range of crystal sizes and morphologies observed in the SEM images. While TPA_AliPr_H and TPA_AlOH_H show no large differences in micropore volume (Figure 4.24), OSDA_AlOH_H has a differently shaped isotherm caused by the greater external surface area and intercrystallite porosity arising from its smaller crystal size. Notably, the activated forms of the samples prepared in (diDABCO-C8)$(OH)_2$ as a mineraliser have smaller micropore volumes than TPA_AliPr_H or TPA_AlOH_H. The fact that the micropore volume can be controlled in STA-30 and the adsorption isotherm has the ideal shape predicted for the SWY topology in the case of the TPA_diQuin-C8 led to the conclusion that the increased Ar uptake is not due to a phase transition triggered at a specific pressure during the adsorption, but it is rather due to the presence of an additional feature that allows for the increased uptake.

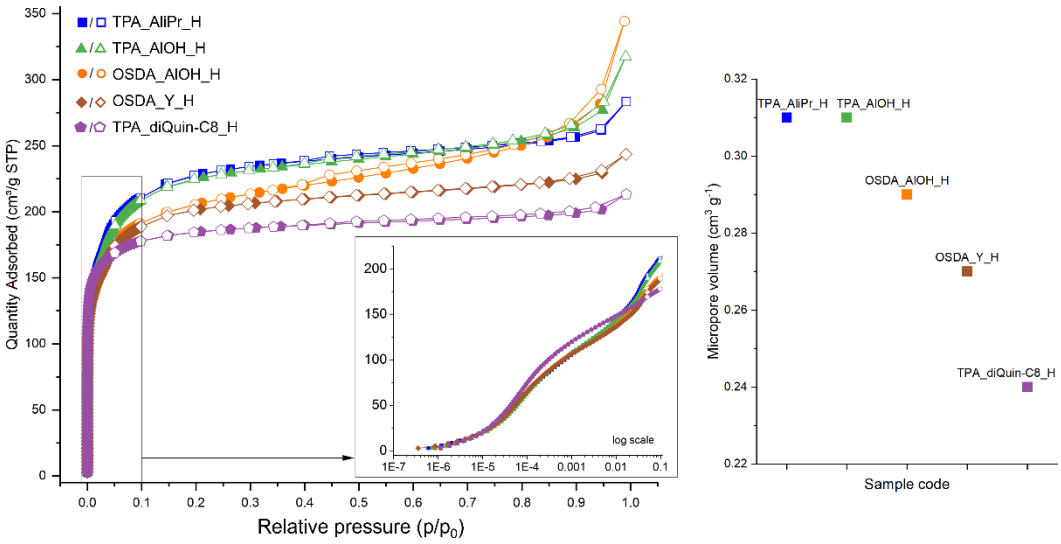

Figure 4.24 Ar adsorption/desorption isotherms at 87 K collected from activated forms of the 5 selected STA-30 zeolites with an insert showing the 10^{-7}–0.1 p/p_0 region in a logarithmic plot (left) and the micropore volumes determined at ~0.5 p/p_0 relative pressure (right).

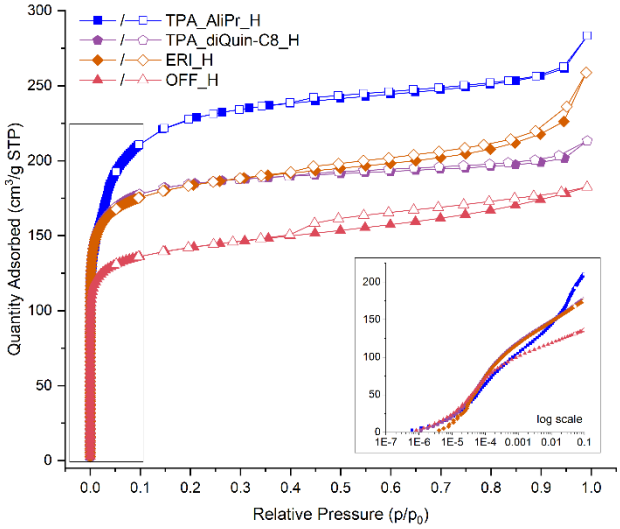

Figure 4.25 Ar adsorption/desorption isotherms measured at 87 K on the H–forms of TPA_AliPr, TPA_diQuin-C8, ERI and OFF (left, the insert shows an enlarged view of the 10^{-7}–0.1 p/p_0).

Based on all these observations, it became clear that additional microporosity can be created in STA-30 and that it can be controlled through choice of mineraliser and OSDA. This can be observed in the Horvath–Kawazoe (HK) plots as well (Figure 4.26, left), which show additional peaks in the 12–14 Å range for the activated diDABCO-C8_STA-30 materials. Furthermore, the intensity of the peak around 6–7 Å (from adsorption within the *swy* and *gme* cages, through 8MR windows) is lower for all activated diDABCO-C8_STA-30, compared to the activated TPA_diQuin-C8_H sample. DFT plots for pore–

size distributions derived from the same data (Figure 4.26, right) show a range of pore sizes (6–25 Å) for all samples, but TPA_diQuin-C8_H still has the highest pore volume correlated with the expected pore width for the SWY topology.

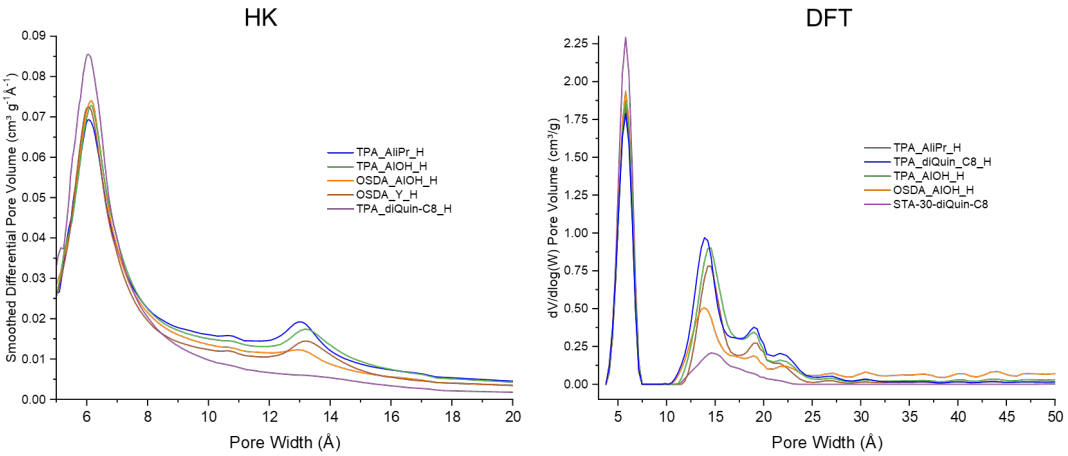

Figure 4.26 HK plots (left) and DFT plots (right) obtained from Ar adsorption isotherms at 87 K.

OSDA choice and larger microporosity

In order to further prove that the STA-30 sample synthesised with diQuin-C8^{2+} does not possess the additional microporosity, the calcined forms of a diDABCO-C8_STA-30 sample and a diQuin-C8_STA-30 sample were stirred with (diDABCO-C8)Br_2 10% aq. sol. Once the OSDA had been removed from the structure by calcination, it should not be able to enter the structure through the 8MR as the diDABCO-C8^{2+} cation is too large. However, it was found that it was possible to reintroduce ~1/3 of the initial amount of OSDA in a diDABCO-C8_STA-30 sample, but no diDABCO-C8^{2+} could enter the diQuin-C8_STA-30 sample, as shown in the TGA plots below (Figure 4.27). When this is correlated with the CHN analysis and the initial calculations of 3 diDABCO-C8^{2+}/unit cell, it is clear that this OSDA plays a role in the templating of the larger microporosity in addition to the templating of *swy* cages.

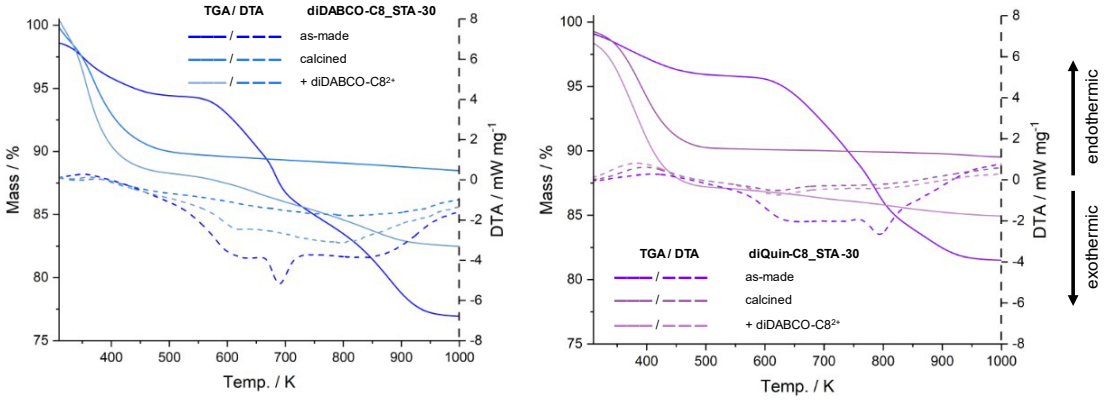

Figure 4.27 TGA mass loss (solid lines) and DTA curves (dashed lines) of as–made, calcined, and diDABCO-C8–exchanged forms of diDABCO-C8-STA-30 (left) and diQuin-C8-STA-30 (right).

The incorporation of the intact diDABCO-C8^{2+} was confirmed by ^{13}C CP MAS NMR spectra as well (Figure 4.28), which also clarified the fact that the splitting associated with the DABCO end groups of the OSDA observed in the as–made sample is due to the presence of diDABCO-C8^{2+} in two types of environments – the *swy* cage and the larger micropore. On the other hand, the ^{13}C NMR spectrum of diQuin-C8_STA-30 (Figure 4.9) did not show any splitting in any of its peaks, further confirming the singular role that diQuin-C8^{2+} cation plays in templating the *swy* cage in STA-30 zeolites. While there is a difference between the calcined diQuin-C8_STA-30 and the material that was mixed with the (diDABCO-C8)Br_2 solution in their TGA mass loss curves, it is most likely due to an increase in physisorbed H_2O from the repeated mixing with hot aqueous solutions of the OSDA salt. The DTA curves (dotted lines in Figure 4.27) show that there was no additional transformation taking place in the 'exchanged' diQuin-C8_STA-30 in the high temperature (> 500 K) region of the analysis, compared to the calcined form of diQuin-C8_STA-30. On the other hand, the additional mass loss in the exchanged diDABCO_STA-30 was shown to be due to a decomposition of the OSDA that re–entered the larger micropore feature, as evidenced by the similarities between the 'exchanged' diDABCO_STA-30 and the as–made form of the same material.

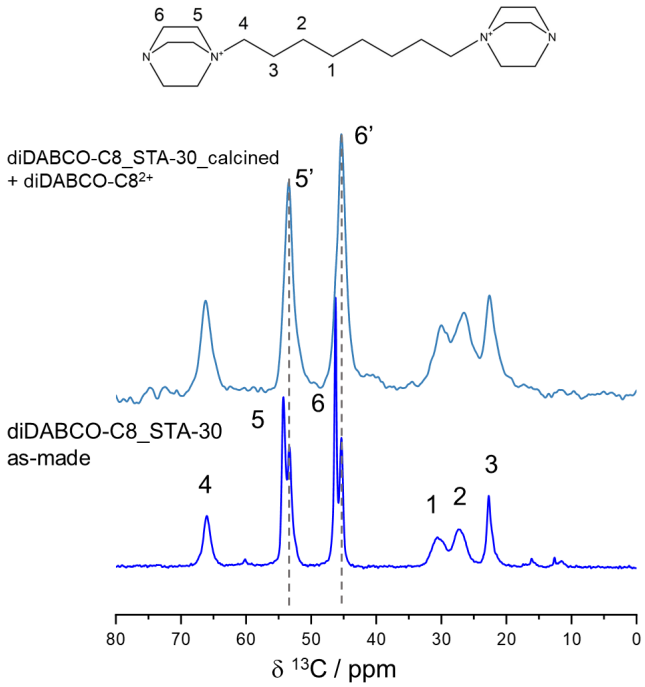

Figure 4.28 ^{13}C CP MAS NMR spectra of diDABCO-C8_STA-30 as–made compared with diDABCO-C8_STA-30 exchanged with a 10% aq. sol. of (diDABCO-C8)Br_2.

Solid–state MAS NMR and FTIR spectra

The findings from Ar adsorption in conjunction with ^{13}C NMR and TGA provided some insight into certain unusual features of STA-30. However, these techniques could not offer information on the materials' acidity and number of defects (SiOH). Consequently, all samples were also probed by further solid–state MAS NMR and FTIR spectroscopies.

The frameworks were characterised by ^{29}Si and ^{27}Al NMR spectroscopy. The ^{29}Si spectra (Figure 4.29, left) show that there are no major differences between the STA-30 samples in terms of the distribution of Al in the framework. It is important to note that the SWY topology contains two distinct magnetic environments ~7 ppm apart, among the 3 different T sites (all with multiplicity of 24) in a 2:1 ratio, as has been previously shown through CASTEP calculations.[11] Thus, every environment leads to 2 peaks in the ^{29}Si NMR spectra with intensity ratios 2:1. For all STA-30 samples studied, the following ^{29}Si secondary shell environments are present: $Si(OSi)_2(OAl)_2$ (-96 ppm, -100.9 ppm), $Si(OSi)_3(OAl)_1$ (-103.5 ppm, -108.4 ppm) and $Si(OSi)_4$ (-108.9 ppm, -113.8 ppm). Accounting for these, it was possible to calculate approximate Si/Al ratios that were in close agreement with XRF data (Table 4.6, deconvolution done by Jonathan Bradley). All activated samples contained SiOH groups as well, as can be seen in the ^{1}H NMR spectra, which will be discussed later (Figure 4.30A). These were expected to appear in

the ^{29}Si NMR spectrum as a broad peak around -102 ppm based on the ^{1}H–^{29}Si HETCOR described in the previous chapter.

The ^{27}Al NMR analysis of the activated samples (Figure 4.29, right) reveals that the frameworks of all materials are stable (peak due to tetrahedral Al, Al^{IV}, at 58 ppm is the most intense) and a minimal amount of extra–framework Al (EFAL) is created during activation in all samples (broad peak around 0 ppm). Furthermore, there are two sharp resonances at 0 ppm and -2 ppm, which have been observed previously to disappear upon ion exchange with NH^{4+}.[11] We speculate that these are reversibly coordinated framework octahedral species of the kind invoked in H–mordenite by Ravi *et al.*[12,13] Notably, the TPA_diQuin-C8_H spectrum stands out again, as the peaks assigned to octahedral framework Al are sharper. This shows that this particular feature of STA-30 zeolites is not related to the larger microporosity, but it is related to the framework topology.

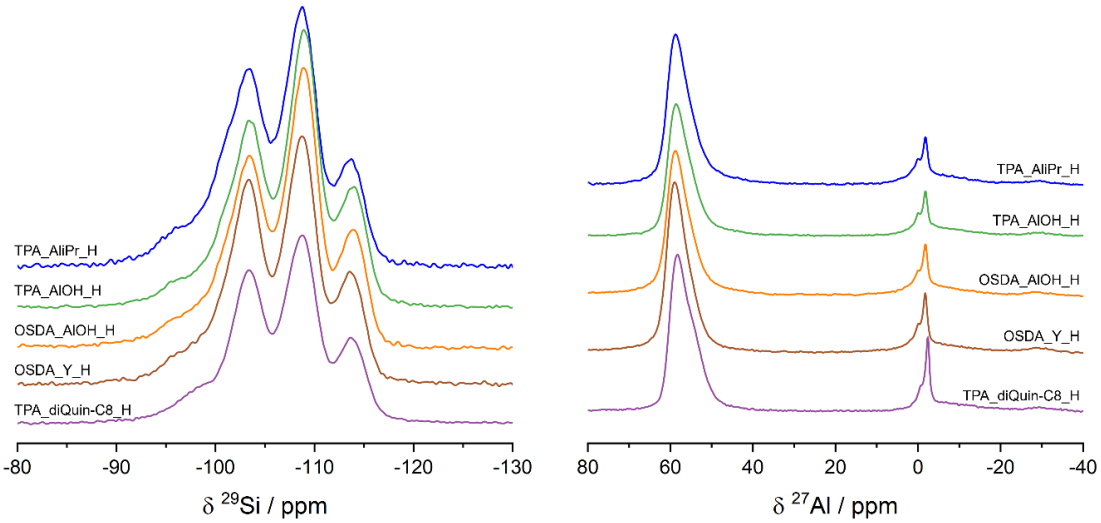

Figure 4.29 Overlapped ^{29}Si (left) and stacked ^{27}Al (right) MAS NMR spectra of activated samples.

Table 4.6 Comparison of silica–to–alumina ratio (SAR) in the products as determined by XRF or ^{29}Si MAS NMR spectra.

Sample	XRF Si/Al	NMR SAR
TPA_AliPr_H	12.0	13 ± 1
TPA_AlOH_H	14.1	15 ± 1
OSDA_AlOH_H	13.5	15 ± 1
OSDA_Y_H	12.0	13 ± 1
TPA_diQuin-C8_H	11.9	11.9 ± 0.7

The ^{1}H MAS NMR and FTIR spectra of the dehydrated samples (Figure 4.30) confirm that all samples possess a range of hydroxyl groups. Bridging Brønsted acidic OH groups give rise to a signal at ~3.8 ppm (Si–O<u>H</u>–Al) in the ^{1}H NMR spectra and a band at 3605 cm^{-1} (Si–OH–Al) in the FTIR spectra of all activated STA-30 zeolites.[14,15] These Si–OH–Al groups can be classified as 'isolated', but all samples also contain Si–OH–Al that are H–bonded, based on both the ^{1}H NMR spectrum (broad peak at 4.2 ppm) and the FTIR spectra (band at 3560 cm^{-1}).[15,16] AlOH species can be identified in all spectra based on the peak at ~2 ppm in ^{1}H NMR spectra and the band at 3665 cm^{-1} in the FTIR spectra.[16]

As described in the Introduction, understanding the high level of silanol SiOH observed previously in H,K–STA-30 was a key aim of this in–depth characterisation study. NMR and FTIR spectra (Figure 4.30) show that there is a large concentration of SiOH in most samples, apparent from the ratio of the Si–OH–Al and SiOH peak areas. Based on these spectra, TPA_diQuin-C8_H is the only sample that has a Si–OH–Al/SiOH ratio above 1, which means that the concentration of defects, quantified as silanols, was much lower when using diQuin-C8^{2+} as OSDA. Furthermore, the relative ratio of the Si–OH–Al/SiOH increases in the order TPA_AliPr_H ≈ TPA_AlOH_H < OSDA_AlOH_H < OSDA_Y_H, showing that the Al source does not play a significant role in the formation of SiOH, but that the mineraliser has an impact on the amount of defects present in the activated structures.

These observations are in line with the increase of the maximum uptake in the Ar adsorption isotherms and the consistent differences in silanol concentration between the diDABCO-C8_STA-30 materials and diQuin-C8_STA-30. Thus, it can be concluded that the presence of additional '1.3 nm' microporosity in STA-30 is linked to an increase in the amount of defects. In order to understand the nature of the porosity more fully, the samples were tested further with the use of a basic probe molecule, pyridine.

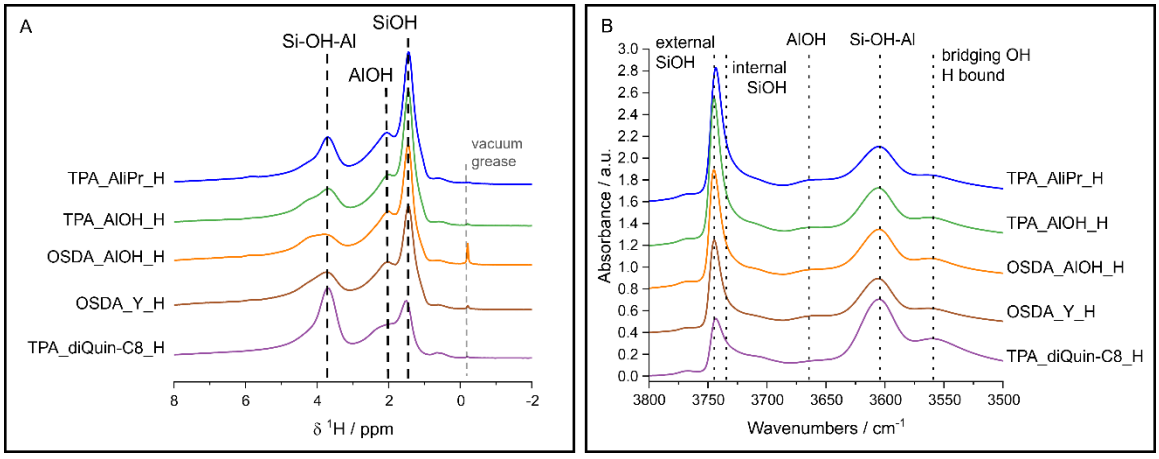

Figure 4.30 (A) Offset ^{1}H NMR spectra of activated samples and (B) offset FTIR spectra of activated samples. Absorbance values were normalised to the largest sample mass and offset for clarity.

Further characterisation of the hierarchical microporosity

Initially, NH_3–TPD monitored by FTIR was performed on TPA_AliPr_H, as a benchmark. This preliminary study showed that NH_3 was able to access all acid sites in STA-30 and that the acid sites present in STA-30 behaved as expected of a small–pore zeolite, with complete desorption of NH_3 from BAS around 673 K.[17] (Figure 4.31)

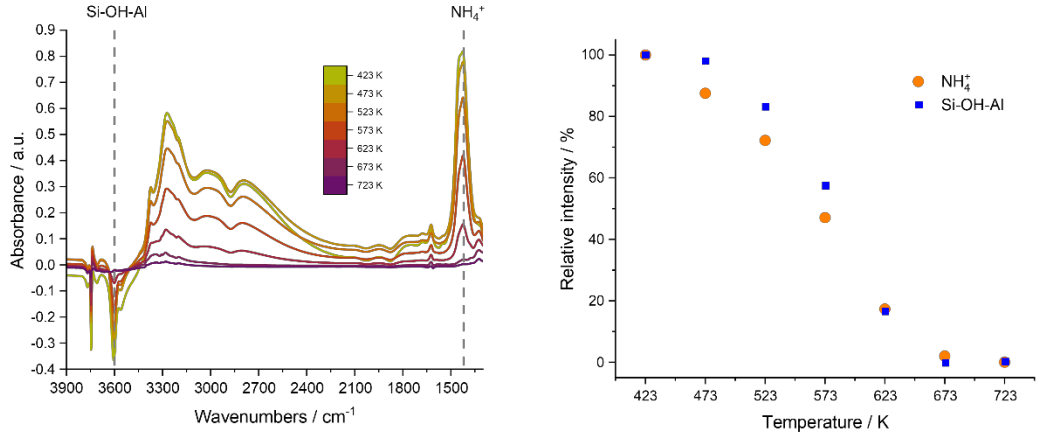

Figure 4.31 Difference FTIR spectra between the spectrum of dehydrated TPA_AliPr_H and spectra collected at temperatures between 423 K and 723 K after the structure had been loaded with NH_3 (left) and the variation of the intensity of the peaks that show the interaction between NH_3 and the zeolite acid sites.

Pyridine (Py) has been extensively used as a probe molecule in FTIR studies because it can interact with SiOH or Si–OH–Al (Brønsted acid sites) to form pyridinium cations (Py–H^+) and it can also coordinate to Lewis acid sites, such as various Al species in the zeolite.[15,18] This leads to distinctive bands associated with Brønsted acid sites (BAS) and

Lewis acid sites (LAS). The most straightforward way to visualise the interaction between Py and the accessible acid sites in the zeolite is by analysing the difference between the spectra collected from the dehydrated samples and the ones collected from the samples loaded with Py.

While it might seem counterintuitive to probe a small pore structure such as SWY with Py, a molecule that can only enter rings larger than 8 MR due to its kinetic diameter of 5.4 Å, there would still be interactions with the external SiOH on the crystal surface and potentially even with some of the acid sites that are 'exposed' in pore 'mouths'.[19] Indeed, in a parallel study on the small–pore aluminosilicate ERI, very little interaction between Py and the zeolite was observed. On the other hand, Py was shown to have high accessibility in the other 'close relative' OFF that possesses 12 MR channels in addition to the 8MR windows into *gme* cages. (Figure 4.33) However, the FTIR difference spectra (Figure 4.32) of most STA-30 samples selected for further characterisation show that many of the silanols are accessible to Py, and a large amount of the Si–OH–Al are accessible to Py, as evidenced by the negative peaks in the SiOH region (3800–3500 cm^{-1}) and the peaks in the Py region (1700–1400 cm^{-1}). This indicates that access to many of the acid sites of diDABCO-C8_STA-30 materials is possible via rings larger than 8 MR (accessibility values can be found in Table 4.7). The extinction coefficients for ZSM-5 (aluminosilicate MFI) were used in the quantification of the BAS and LAS concentrations.[18]

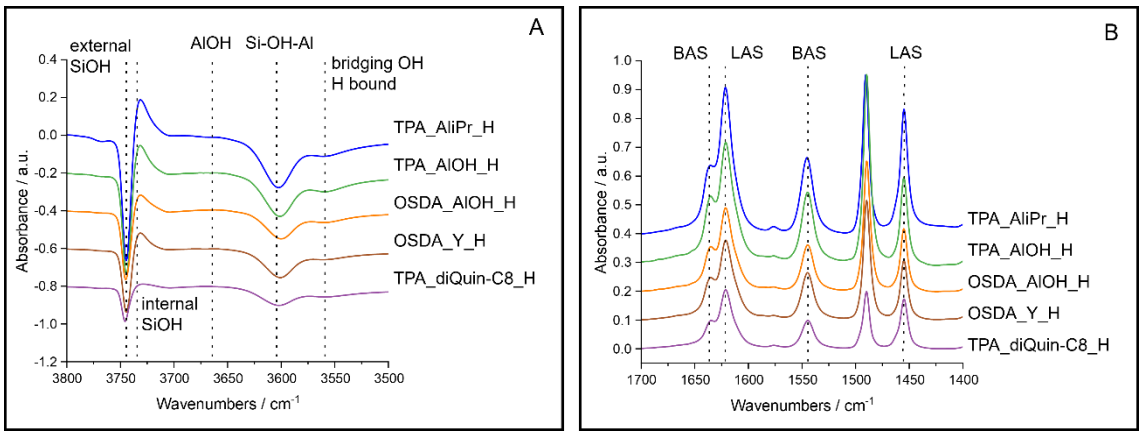

Figure 4.32 (A) Py accessibility probed by FTIR and presented as difference spectra between the spectrum of the dehydrated sample and the spectrum collected from pyridine adsorbed at 473 K – SiOH region and (B) Py region (right). Absorbance values were normalised to the largest sample mass and offset for clarity.

Table 4.7 Concentration of BAS and LAS accessible by Py in the various samples studied, as well as percentage of total Si–OH–Al accessible to Py based on FTIR studies.

Sample	BAS_{Py} (μmol g^{-1})	LAS_{Py} (μmol g^{-1})	%Total Si–OH–Al accessible to Py
TPA_AliPr_H	305	200	77
TPA_AlOH_H	275	135	68
OSDA_AlOH_H	180	100	47
OSDA_Y_H	185	95	46
TPA_diQuin-C8_H	110	85	17
ERI_H	25	20	7
OFF_H	285	115	50

The high concentration of silanols, and the correlation between their quantity and the additional microporosity (rather than with their crystallite size), suggests that many of them are present in the larger 'secondary' micropores and appear in the same place that external silanols are usually observed because they are not confined in narrower cages or channels. As an example of this, while the particle size of OSDA_AlOH_H is much smaller than that of OSDA_Y_H, and the external surface area consequently much larger (as seen in the Ar isotherm), they have similar levels of silanols and silanol accessibility (180–185 μmol g^{-1}, 46–47% accessibility – Table 4.7).

The accessibility of the Si–OH and Si–OH–Al follows the same trends (Table 4.7) observed throughout the data discussed so far, with the TPA_AliPr_H and TPA_AlOH_H samples exhibiting the largest accessibility, followed by the OSDA_AlOH_H and OSDA_Y_H samples. The peak at 3745 cm^{-1} loses the least amount of intensity upon Py adsorption in the case of TPA_diQuin-C8_H and it is the closest to the loss observed in ERI, meaning that the behaviour of TPA_diQuin-C8 is closest to that expected for an 8MR zeolite. (Figure 4.33) There is, however, still an unexpected accessibility of Si–OH–Al and LAS sites, which implies that there are some pathways of access present in this sample, but to a much lesser extent than for the samples prepared with diDABCO-$C8^{2+}$.

Py accessible BAS and LAS concentrations show the same trend as the accessibility of SiOH in the different STA-30 materials. It is interesting to note that the BAS peak is that of a pyridinium cation (Py–H^+) which is the result of the interaction of Py with either Si–OH and Si–OH–Al. Since the Py interacts largely with SiOH in TPA_diQuin-C8_H, rather

than with Si–OH–Al, it could explain how TPA_diQuin-C8_H still exhibits a high amount of BAS, even though its Py accessibility of Si–OH–Al is much lower than that of the other samples.

Finally, adsorption isotherms were collected for isopentane (2-methylbutane) onto diDABCO-C8_STA-30_H and diQuin-C8_STA-30 at 293 K. Branched alkanes such as this cannot pass through the 8R windows, so the uptake of isopentane can occur either on the surface or into pore space (such as the 1.3 nm pores observed via the HK plots) accessible via medium or large pore windows. Figure 4.34 shows that a Type I isotherm is obtained for the adsorption of isopentane on diDABCO-C8_STA-30, but there is a very low uptake of isopentane in diQuin-C8_STA-30. The additional pore volume is 0.12 cm^3 g^{-1} (calculated via the excess uptake at p/p_o = 0.2 and using the liquid density). This confirms that diDABCO-C8_STA-30 zeolites possess additional porosity above that present in diQuin-C8_STA-30 zeolites.

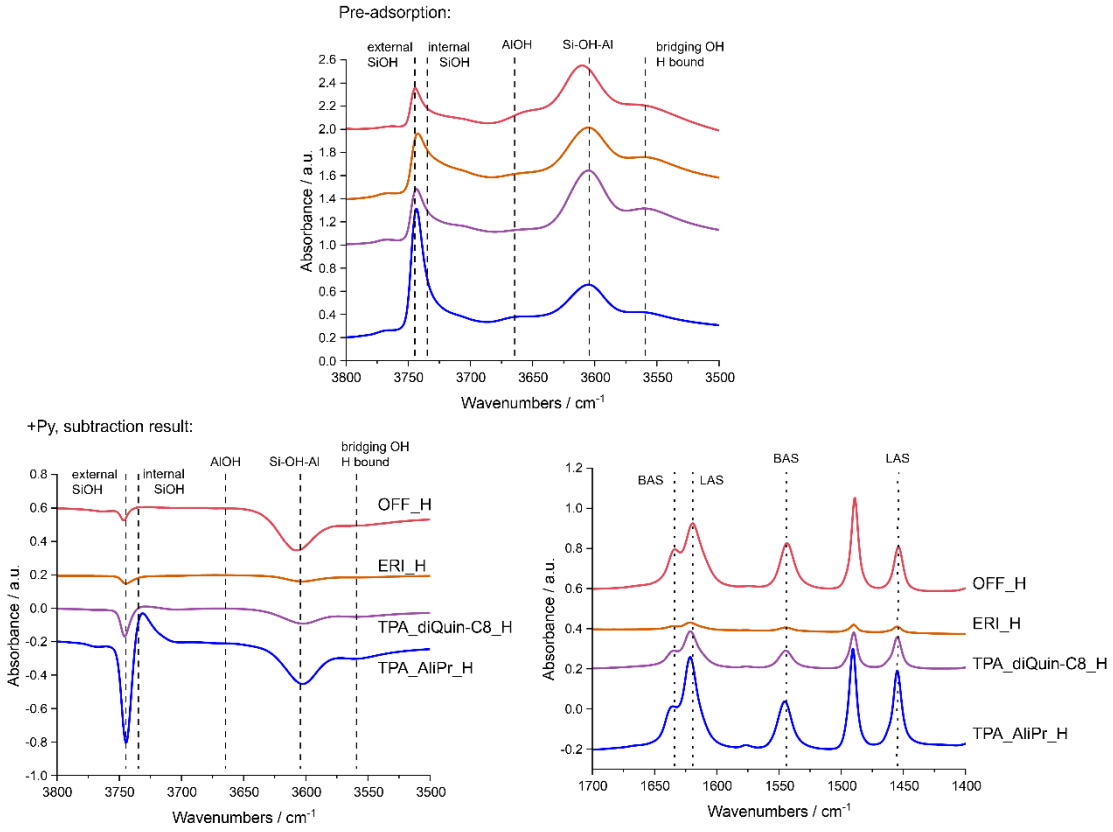

Figure 4.33 SiOH region of the FTIR spectra of the H–forms of TPA_AliPr, TPA_diQuin-C8, ERI and OFF, after dehydration (top) and difference FTIR spectra between the aforementioned data and the spectra of the samples upon pyridine (Py) adsorption at 473 K – SiOH region (bottom, left) and Py region (bottom, right). Absorbance values were normalised to the largest sample mass and offset for clarity.

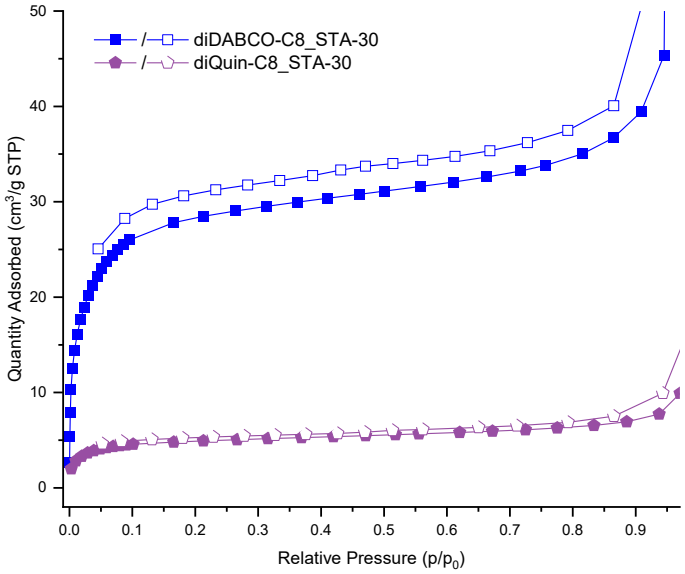

Figure 4.34 Adsorption isotherm of isopentane at 293 K measured on diDABCO-C8_STA-30 and diQuin-C8_STA-30.

In a continuation of this experiment, a sample of STA-30 with additional microporosity was allowed to adsorb isopentane at 293 K at 0.28 bar ($p/p_o = 0.36$), before being cooled to 87 K to 'freeze' the isopentane in place. Subsequent measurement of the Ar adsorption isotherm gave an uptake of 110 $cm^3\ g^{-1}$ (STP). (Figure 4.35) This may reasonably be compared to 180 $cm^3\ g^{-1}$ (STP) measured for the diQuin-C8_STA-30, although it is plausible that part of the isopentane molecule, while not having full access to the crystalline framework, will take up some 8R window sites at the interface between crystalline and additional porosity. In any case, this demonstrates that most of the crystalline pore space, as defined by the small pore SWY structure, remains accessible even if the larger pores are filled. The HK pore size distribution plot shows that the additional porosity at 1.3 nm is no longer present when the isopentane occupies these larger micropores. Furthermore, by evacuating the sample after this experiment and re–measuring the Ar adsorption at 87 K, Figure 4.35 shows that both the small and large microporosity can be restored in diDABCO-C8_STA-30 zeolites.

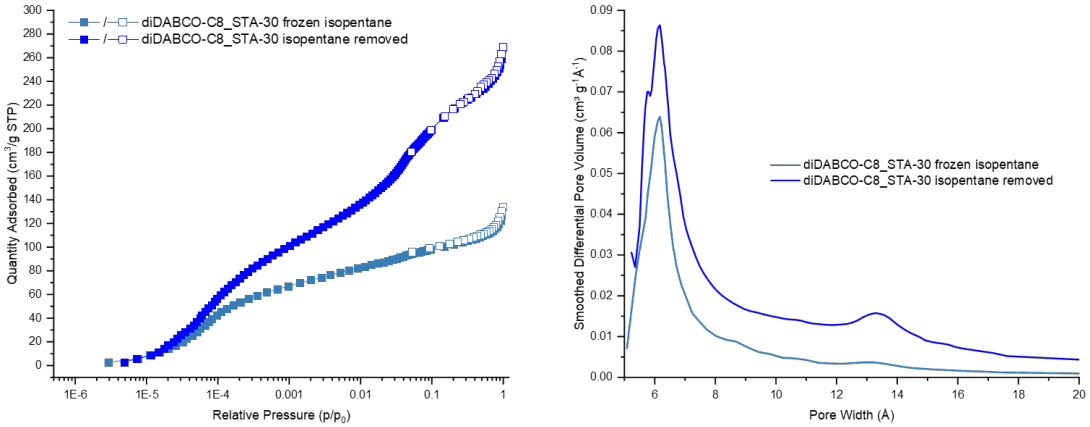

Figure 4.35 Ar adsorption isotherms (left) and derived HK plots (right) at 87 K collected after pre–adsorbed isopentane was frozen into pores (light blue) and after the evacuation of isopentane and Ar (blue). The isotherms are plotted on a logarithmic scale of p/p_0.

Model for hierarchical microporosity

With the additional porosity confirmed and probed through the studies described above, it was possible to build computational models around these observations. The STA-30 structure with K^+ filling the *can* cages was chosen as the parent because it resembled the final activated forms in this study. One structural model for the additional porosity which gives large micropores of around the measured dimensions is given in Figure 4.36. To obtain this model, a column of *can* and *d6r* cages in a 3×3×1 supercell was removed (in CrystalMaker[20]). The addition of H atoms on terminal Si–O within the large pore and a geometry optimisation calculation were performed in Materials Studio using the COMPASS III forcefield.[21,22] Convergence was achieved despite the removal of the *can*+*d6r* column, showing that it is feasible that this could occur inside the zeolite and for it to retain stability.

The Ar adsorption isotherm at 87 K between 10^{-4} and 100 kPa fugacity was calculated using Materials Studio.[21] The calculation was performed on the unit cell of SWY and the results matched closely the Ar adsorption isotherm of TPA_diQuin-C8_H. (Figure 4.37) This validates the computational setup used. Ar adsorption simulations were then conducted at 10^{-4}–1 kPa (4 steps), 10 kPa, 50 kPa and 100 kPa fugacity on a simulated 2×2×1 supercell that had a column of *can* and *d6r* removed as it has been previously described. An isotherm with the same step sizes as for the unit cell was not calculated for this system due to its large size which implied large computational costs for each calculation. It would be beneficial to run more calculations on larger supercells to obtain more accurate data on the uptake of Ar in structures with various proportions of removed

can and *d6r* columns. However, the Monte Carlo type simulations used here would incur too large a computational cost.

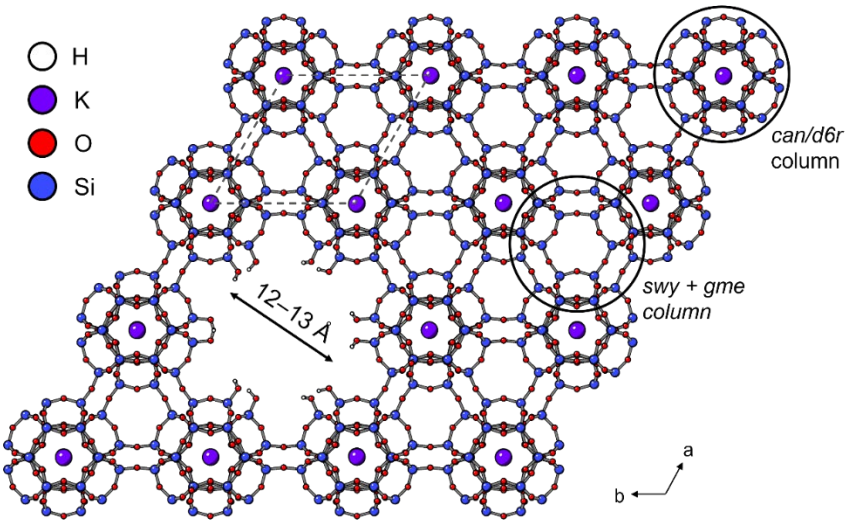

Figure 4.36 Model for hierarchical microporosity in the SWY framework shown on a 3×3×1 supercell for ease of visualisation, the SWY unit cell size is delineated with a dotted line.

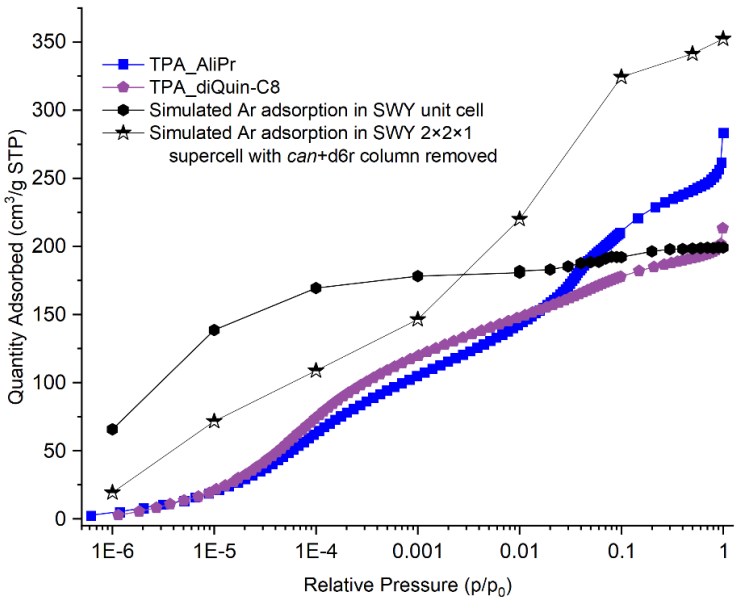

Figure 4.37 Ar adsorption isotherms at 87 K computationally simulated uptake compared with experimental data, presented on a logarithmic scale in the 5×10^{-7}–1 relative pressure.

The simulated values for the uptake at 50 kPa are ~40 Ar atoms in the SWY unit cell and 210 Ar atoms in the large micropore 2×2×1 supercell (which contains the equivalent of 4 unit cells). 50 kPa fugacity was chosen as the data point of reference because at that fugacity there was a very close match between the calculated and experimental uptake of TPA_diQuin-C8_H. The computational models for pressure might not resemble the

real physical system perfectly so there could be a small variation between the fugacity value and the relative pressure in the experimental isotherm, but since the uptake remained constant after 40 kPa, it was considered that the value at 50 kPa would provide an accurate average value. Furthermore, all of the experimental Ar adsorption isotherms showed maximum uptake when the 0.5 p/p_0 relative pressure was reached, but at higher relative pressures effects such as intercrystallite adsorption could influence the uptake values. With the aid of these computed values, it was possible to determine the amount of *can* and *d6r* columns missing in the structure to enable the zeolite to possess the Ar uptake experimentally measured on the diDABCO-C8_STA-30 samples (calculations in Appendix Chapter 4). Thus, approximately 1 in 10 and 1 in 40 columns of *can* and *d6r* cages are missing from the TPA_AliPr_H or TPA_AlOH_H samples and OSDA_AlOH_H or OSDA_Y_H samples, respectively. However, there is a random distribution of these missing columns since the activated diDABCO-C8_STA-30 structures have a good match with the SWY topology, as shown by the Rietveld refinements performed previously.[11] Thus, through the control of the OSDA, it was possible to introduce hierarchical microporosity during the synthesis of STA-30.

The hierarchical extra–large/small microporosity in line with the model proposed above was also observed in images collected with an aberration corrected scanning transmission electron microscope equipped with annular dark field detector (C_s–corrected STEM–ADF). These micrographs were collected by Alvaro Mayoral in Zaragoza. Some of the images collected from the diDABCO-C8_STA-30 and diQuin-C8_STA-30 zeolites are presented in Figure 4.38. The most relevant observation in these images was the fact that no contrast is observed in the diQuin-C8_STA-30 crystals, whereas diDABCO-C8_STA-30 shows variations in contrast throughout the crystal. The width of the regions of varying contrast matches the size of columns of *can*+*d6r* cages in the [100] direction (marked by yellow arrows). The high–resolution images that clearly show the stacking of the ABC layers prove that both zeolites possess ordered SWY structures. Thus, the contrast is due to differences in thickness in the diDABCO-$C8^{2+}$ templated zeolites. Despite the elongated shapes of the crystals, it was possible to collect images along the [001] direction as well which showed that the differences in contrast are indeed due to randomly distributed *can*+*d6r* cages missing from the zeolite. The QSTEM software[23] simulations show that by using the model generated of the SWY supercell with missing *can*+*d6r* cages, similar images can be generated to those captured experimentally of the columns of *can* cages occupied by K^+ atoms.

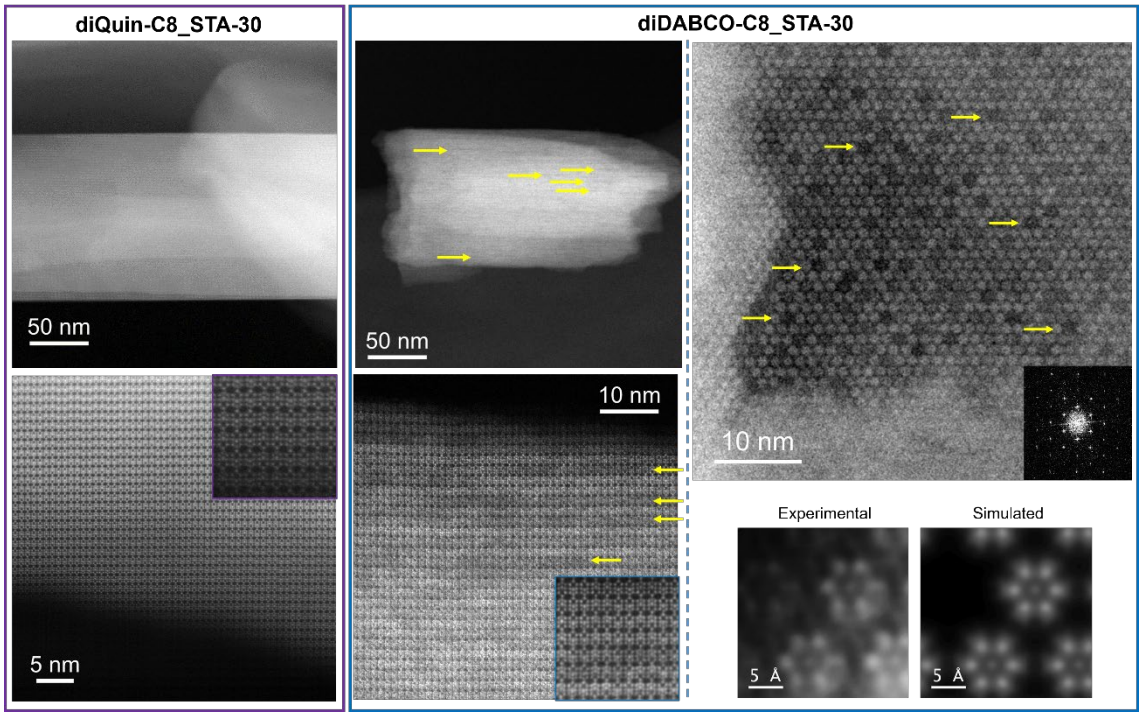

Figure 4.38 C_s–corrected STEM-ADF images of diQuin-C8_STA-30 (left, purple outline) and diDABCO-C8_STA-30 (middle and right, blue outline), highlighting the difference in contrast in diDABCO-C8_STA-30 that represents the missing *can+d6r* columns. A comparison of experimental images of *can* and *d6r* columns observed in diDABCO-C8_STA-30 and the QSTEM simulation STA-30 with removed *can+d6r* columns and K^+ occupying the *can* cages.

The synthesis parameters that lead to the control of hierarchical microporosity will be discussed and summarised for an overview of the mechanism of formation of hierarchical microporosity in STA-30. First of all, the mineraliser source was shown to induce control over the amount of additional microporosity introduced. Large quaternary ammonium cations have been used in the past to introduce hierarchical mesoporosity in materials such as ZSM–5 (MFI).[24] In this study, the presence of TPA^+ in the gel could serve as an initiator for the formation of larger microporosity as it would hold aluminosilicate precursors further apart in the solution due to its larger size and lower charge density compared to diDABCO-$C8^{2+}$. However, it is clear that it acts in concert with diDABCO-$C8^{2+}$ cations and it enhances their effect.

Most significantly though, the diDABCO molecules are the principal cause of hierarchical microporosity in STA-30 by serving a dual structure directing purpose here, as confirmed by the ^{13}C CP MAS NMR spectra discussed earlier (Figure 4.28). Thus, diDABCO based templates act in a similar manner to soft templates which are used in hierarchical mesoporous materials to template specific cages in the target zeolite, but also as the mesoporogen. Meanwhile, the diQuin–based OSDA only acts as the template for the

swy cage, as evidenced by the lack of splitting in any of the peaks in its ^{13}C CP MAS NMR spectra, so it is not capable of structurally directing the formation of the larger micropore.

The most relevant difference between these two molecules is the fact that DABCO unit terminates with a N atom with a lone pair of electrons, whereas the quinuclidine unit terminates with a C–H group. The presence of the lone pair enables the DABCO end–group to potentially H–bond to a Si–OH during crystallisation, and then disrupt the growth of the zeolite. Furthermore, once this larger micropore might start forming due to this interaction, diDABCO-C8^{2+} molecules could potentially template the larger micropore by fitting normal to the *c*–direction. Schematic representations of possible positions of diDABCO-C8^{2+} in the large micropore can be found in Figure 4.39. Since the C–H group on the quinuclidine end group of diQuin-C8^{2+} is not capable of forming H-bonds with Si–OH, it does not favour the interaction between the OSDA and the framework, so it does not favour the formation of the additional micropore. The H–bonding of some of the DABCO units would create a secondary set of environments compared to the intact molecule that templates an ideal *swy* cage, as observed in the ^{13}C NMR spectra of the as–made and diDABCO-C8^{2+} loaded diDABCO-C8_STA-30 materials.

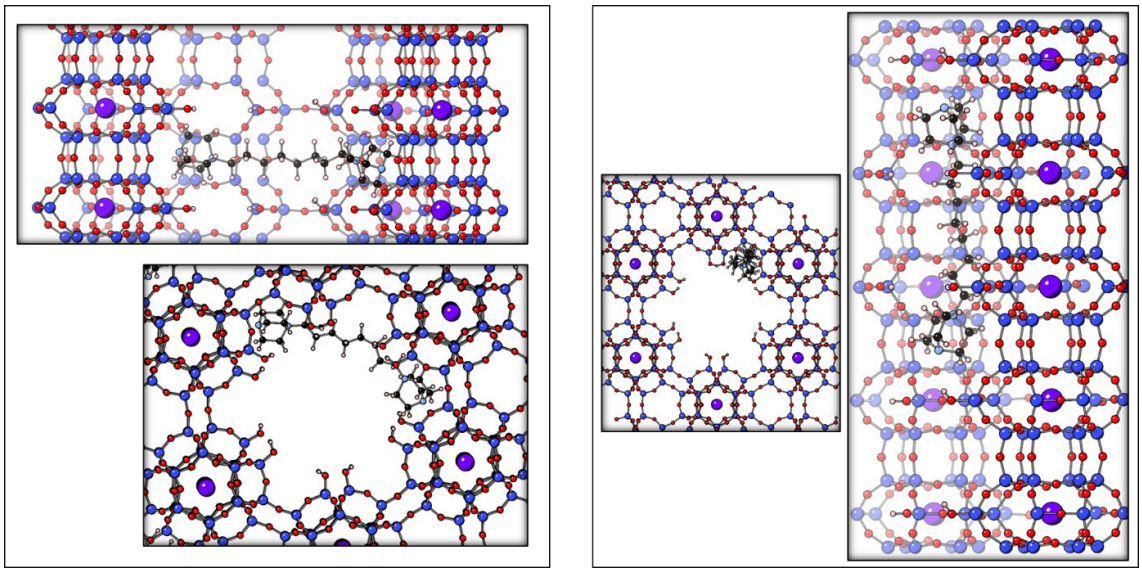

Figure 4.39 Schematic representation of potential arrangements of diDABCO-C8^{2+} in the large micropore present in diDABCO-C8_STA-30 zeolites.

Conclusion

New synthesis pathways to aluminosilicate STA-30 were designed and optimised successfully, beyond the initial CDM based preparation that used diDABCO-C8^{2+} and

KOH as crystallisation SDAs. New inorganic cations, OSDA precursors and a new OSDA were successfully incorporated in the second step of the CDM type approach. It was found that this allows the *in–situ* synthesis of the OSDA with no impact on the properties of the crystallised zeolite in terms of stability upon activation. Furthermore, diQuin-C8^{2+}, which is a molecule with a very similar composition to diDABCO-C8^{2+}, was successfully used to synthesise STA-30 with a new crystallite morphology and properties. Similar gel compositions in terms of OH^-, Si, Al to those used in CDM were adapted for use in other approaches, such as a more 'conventional' hydrothermal approach with no aging step and also for a partial interzeolite conversion route. It was found that a solution of the hydroxyl form of diDABCO-C8^{2+} could successfully act as a mineraliser in these routes, avoiding the use of additional TPAOH. While aluminosilicate STA-30 could be prepared through all these routes, the crystallisation kinetics of the three approaches were different, with the slowest being the hydrothermal approach, followed by CDM and then partial IZC.

The unusually large number of defects in the STA-30 zeolite reported in the previous chapter has been explained in this chapter through a careful study of the synthetic conditions and in–depth characterisation of selected samples. Ar adsorption studies showed an increased uptake for the samples synthesised with (diDABCO-C8)Br_2 as OSDA, compared to STA-30 synthesised with the similar compound (diQuin-C8)Br_2. This observation, in conjunction with the NMR and FTIR spectroscopic studies led to the discovery of an additional non-crystallographic micropore 12–13 Å wide in the diDABCO-C8_STA-30 zeolites. The presence of the larger micropore, in turn, leads to an increase in the amount of SiOH groups and Brønsted acid sites that can be accessed by molecular probes, such as pyridine, which cannot diffuse through 8R windows of the ideal SWY framework. Thus, by consideration of the gel components and treatment, one could influence the amount of hierarchical microporosity present in STA-30. This additional microporosity is introduced during the synthesis and has no impact on the overall stability of the zeolite upon activation.

The preparation of hierarchical 3D extra–large/small pore in STA-30 during synthesis and unlocked simply by calcination represents a new approach of introducing a secondary microporosity in a small pore zeolite. This is attractive as many of the current approaches for the introduction of larger porosity in zeolite make use of complex organic compounds or harsh processes that increase the cost of the preparation of the material.[25] Similar to hierarchical mesoporous zeolites, this new feature in STA-30 could lead to

enhanced diffusivity and different activity as a catalyst. The larger amount of SiOHs introduced along with the secondary microporosity could prove useful in various reactions and also as sites for further functionalisation. At the same time, this study showed that an STA-30 zeolite that behaves more like a small–pore zeolite can be prepared as well, with a reduced amount of SiOHs via choice of OSDA. This work effectively provides various scalable routes for the synthesis of STA-30 with desired properties for target applications.

References

1. US20220333519A1, 2022.
2. I. C. Medeiros-Costa, E. Dib, N. Nesterenko, J.-P. Dath, J.-P. Gilson and S. Mintova, *Chem. Soc. Rev.*, 2021, **50**, 11156–11179.
3. J. Zhu, Z. Liu, K. Iyoki, C. Anand, K. Yoshida, Y. Sasaki, S. Sukenaga, M. Ando, H. Shibata, T. Okubo and T. Wakihara, *Chem. Commun.*, 2017, **53**, 6796–6799.
4. J. Zhu, Z. Liu, L. Xu, T. Ohnishi, Y. Yanaba, M. Ogura, T. Wakihara and T. Okubo, *J. Catal.*, 2020, **391**, 346–356.
5. M. Fechtelkord, B. Posnatzki, J.-C. Buhl, C. A. Fyfe, L. A. Groat and M. Raudsepp, *Am. Mineral.*, 2001, **86**, 881–888.
6. J. H. Lee, M. B. Park, J. K. Lee, H.-K. Min, M. K. Song and S. B. Hong, *J. Am. Chem. Soc.*, 2010, **132**, 12971–12982.
7. Tokyo Chemical Industry UK Ltd., https://www.tcichemicals.com/GB/en/, (accessed 22 May 2023).
8. J. Devos, M. A. Shah and M. Dusselier, *RSC Adv.*, 2021, **11**, 26188–26210.
9. IZA database, http://www.iza-structure.org/databases/, (accessed 30 June 2023).
10. Sanidine R060313 - RRUFF Database: Raman, X-ray, Infrared, and Chemistry, https://rruff.info/Sanidine/R060313, (accessed 14 October 2022).
11. R. G. Chitac, J. Bradley, N. D. McNamara, A. Mayoral, A. Turrina and P. A. Wright, *Chem. Mater.*, 2021, **33**, 5242–5256.
12. M. Ravi, V. L. Sushkevich and J. A. van Bokhoven, *J. Phys. Chem. C*, 2019, **123**, 15139–15144.

13. M. Ravi, V. L. Sushkevich and J. A. van Bokhoven, *Nat. Mater.*, 2020, **19**, 1047–1056.

14. A. G. Stepanov, eds. B. F. Sels and L. M. B. T.-Z. and Z.-L. M. Kustov, Elsevier, Amsterdam, 2016, pp. 137–188.

15. S. Bordiga, C. Lamberti, F. Bonino, A. Travert and F. Thibault-Starzyk, *Chem. Soc. Rev.*, 2015, **44**, 7262–7341.

16. B. Gil, S. I. Zones, S.-J. Hwang, M. Bejblová and J. Čejka, *J. Phys. Chem. C*, 2008, **112**, 2997–3007.

17. M. Niwa and N. Katada, *Chem. Rec.*, 2013, **13**, 432–455.

18. V. Zholobenko, C. Freitas, M. Jendrlin, P. Bazin, A. Travert and F. Thibault-Starzyk, *J. Catal.*, 2020, **385**, 52–60.

19. P. Bräuer, P. L. Ng, O. Situmorang, I. Hitchcock and C. D'Agostino, *RSC Adv.*, 2017, **7**, 52604–52613.

20. CrystalMaker Software, 2023.

21. Dassault Systèmes BIOVIA Materials Studio 2020, San Diego: Dassault Systèmes, 2020.

22. R. L. C. Akkermans, N. A. Spenley and S. H. Robertson, *Mol. Simul.*, 2021, **47**, 540–551.

23. C. Koch, Arizona State University, 2002.

24. S. Abelló, A. Bonilla and J. Pérez-Ramírez, *Appl. Catal. A Gen.*, 2009, **364**, 191–198.

25. J. Čejka, R. Millini, M. Opanasenko, D. P. Serrano and W. J. Roth, *Catal. Today*, 2020, **345**, 2–13.

Appendix

Chapter 3

Figures

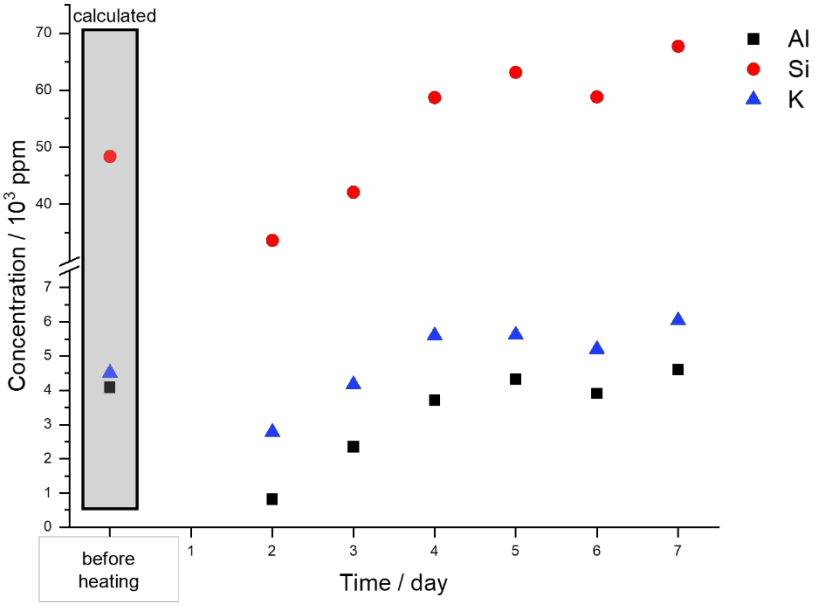

Figure 3.1 ICP results measured from the mother liquors separated from the samples collected during the crystallisation kinetics study. The values for the synthesis gel were calculated based on the amounts of reagents added.

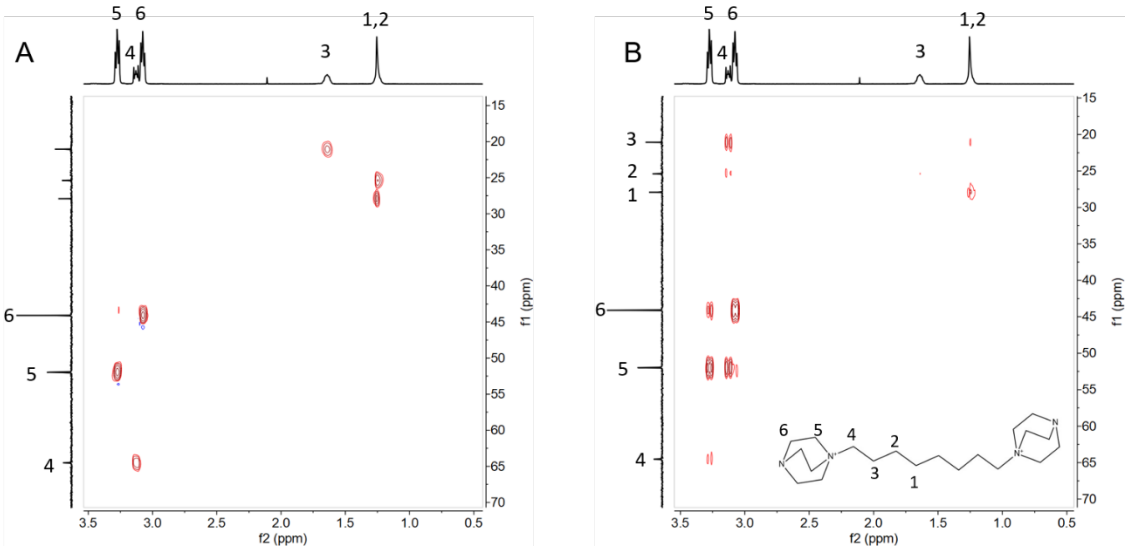

Figure 3.2 2D NMR spectra of (diDABCO-C8)Br_2 in D_2O: ^1H-^{13}C HSQC spectrum (A) and ^1H-^{13}C HMBC spectrum (B).

Tables

Table 3.1 Structural parameters of the calcined and activated STA-30 samples.

Dehydrated calcined STA-30						
Atom	x	y	z	Occupancy	Mult.	U_{iso} (Å^2)
Si/Al1	0.0938(5)	0.4264(5)	0.1251(4)	0.874/0.126	24	0.0232(10)
Si/Al2	1.0019(8)	0.2380(9)	0.1983(4)	0.874/0.126	24	0.0232(10)
Si/Al3	-0.0029(8)	0.2339(9)	0.0521(4)	0.874/0.126	24	0.0232(10)
O1	0.2323(7)	0.4647(15)	0.1228(12)	1.0	12	0.0221(18)
O2	0.0172(16)	0.3446(15)	0.1666(6)	1.0	24	0.0221(18)
O3	0.0785(15)	0.5392(7)	0.1249(13)	1.0	12	0.0221(18)
O4	0.0304(14)	0.3518(14)	0.0801(5)	1.0	24	0.0221(18)
O5	0.1001(12)	0.2002(23)	0.1864(10)	1.0	12	0.0221(18)
O6	0.9984(20)	0.2736(28)	0.25	1.0	12	0.0221(18)
O7	0.8713(11)	0.1287(11)	0.1866(9)	1.0	12	0.0221(18)
O8	0.0992(11)	0.1984(21)	0.0605(10)	1.0	12	0.0221(18)
O9	0	0.2643(28)	0	1.0	12	0.0221(18)
O10	0.8797(10)	0.1203(10)	0.0706(8)	1.0	12	0.0221(18)
K1	0	0	0.8739(21)	0.777(8)	4	0.02995
K2	0.5046(12)	0.4954(12)	0.25	0.495(12)	6	0.11604
Dehydrated activated STA-30						
Atom	x	y	z	Occupancy	Multiplicity	U_{iso}(Å^2)
Si/Al1	0.0900(4)	0.4225(4)	0.12601(31)	0.875/0.125	24	0.0228(8)
Si/Al2	0.9997(6)	0.2389(6)	0.19735(22)	0.875/0.125	24	0.0228(8)
Si/Al3	-0.0024(6)	0.2287(6)	0.05120(24)	0.875/0.125	24	0.0228(8)
O1	0.2256(6)	0.4512(12)	0.1305(7)	1.0	12	0.0179(15)
O2	0.0057(11)	0.3444(11)	0.1668(4)	1.0	24	0.0179(15)
O3	0.0794(13)	0.5397(6)	0.1206(8)	1.0	12	0.0179(15)
O4	0.0316(12)	0.3432(11)	0.0820(4)	1.0	24	0.0179(15)
O5	0.1073(10)	0.2147(20)	0.1859(7)	1.0	12	0.0179(15)
O6	1.0000(17)	0.2634(21)	0.25	1.0	12	0.0179(15)
O7	0.8801(11)	0.1199(11)	0.1836(7)	1.0	12	0.0179(15)
O8	0.0909(6)	0.1818(13)	0.0565(7)	1.0	12	0.0179(15)
O9	0	0.2677(19)	0	1.0	12	0.0179(15)
O10	0.8752(8)	0.1248(8)	0.0710(7)	1.0	12	0.0179(15)
K1	0	0	0.8720(25)	0.668(9)	4	0.10432

Table 3.2 Structural parameters of the as–prepared STA-30 sample.

Atom	x	y	z	Occupancy	Mult.	U_{iso} (Å^2)
Si/Al1	0.09201(13)	0.42331(9)	0.12649(10)	0.876/0.124	24	0.0200(6)
Si/Al2	1.00038(17)	0.23892(20)	0.19784(7)	0.876/0.124	24	0.0200(6)
Si/Al3	0.00027(9)	0.23424(21)	0.05162(8)	0.876/0.124	24	0.0200(6)
O1	0.22720(25)	0.4544(5)	0.13101(24)	1.0	12	0.0103(11)
O2	0.0167(4)	0.35033(27)	0.16926(15)	1.0	24	0.0103(11)
O3	0.0897(4)	0.54485(21)	0.12322(15)	1.0	12	0.0103(11)
O4	0.0331(4)	0.34814(27)	0.08196(14)	1.0	24	0.0103(11)
O5	0.10787(31)	0.2157(6)	0.18712(29)	1.0	12	0.0103(11)
O6	1.0017(9)	0.2684(8)	0.25	1.0	12	0.0103(11)
O7	0.87637(26)	0.12363(26)	0.18540(29)	1.0	12	0.0103(11)
O8	0.09708(26)	0.1942(5)	0.05943(28)	1.0	12	0.0103(11)
O9	0	0.2676(7)	0	1.0	12	0.0103(11)
O10	0.87157(18)	0.12843(18)	0.06557(19)	1.0	12	0.0103(11)
Ow	0.3333	0.6666	0.25	1.0	2	0.50(6)
K1	0	0	0.1196(5)	0.883(6)	4	0.00827
K2	0.4330(11)	0.5670(11)	0.25	0.623(9)	6	0.50566
C282	0.22886	0.68076	0.97885	0.0833	24	0.005
C283	0.22446	0.67078	0.92836	0.0833	24	0.005
C285	0.44312	0.80687	0.92854	0.0833	24	0.005
C286	0.43812	0.80986	0.979	0.0833	24	0.005
C287	0.35395	0.6872	0.86114	0.0833	24	0.005
C288	0.26465	0.57685	0.8362	0.0833	24	0.005
C290	0.40148	0.60899	0.76991	0.0833	24	0.005
C289	0.28458	0.59602	0.78619	0.0833	24	0.005
C291	0.41522	0.62159	0.71963	0.0833	24	0.005
C292	0.43025	0.73845	0.70494	0.0833	24	0.005
C293	0.44951	0.75708	0.65256	0.0833	24	0.005
C294	0.33934	0.6671	0.62768	0.0833	24	0.005
C296	0.22019	0.5764	0.56026	0.0833	24	0.005
C297	0.2174	0.58086	0.50977	0.0833	24	0.005
C299	0.34486	0.79046	0.50962	0.0833	24	0.005
C300	0.35462	0.79538	0.56012	0.0833	24	0.005
C301	0.4388	0.66055	0.55504	0.0833	24	0.005
C302	0.4266	0.66292	0.50476	0.0833	24	0.005
C303	0.35787	0.60084	0.98427	0.0833	24	0.005
C304	0.36061	0.58839	0.93403	0.0833	24	0.005
N281	0.34111	0.69974	0.99685	0.0833	24	0.005
N284	0.3427	0.68481	0.9115	0.0833	24	0.005
N295	0.34174	0.67776	0.57729	0.0833	24	0.005
N298	0.32709	0.67841	0.4919	0.0833	24	0.005
H305	0.15644	0.60035	0.99389	0.0833	24	0.005
H306	0.21638	0.7542	0.98963	0.0833	24	0.005
H307	0.21327	0.73964	0.91193	0.0833	24	0.005
H308	0.15358	0.58475	0.9166	0.0833	24	0.005
H309	0.4295	0.87477	0.91256	0.0833	24	0.005
H310	0.52649	0.81677	0.91599	0.0833	24	0.005
H311	0.42691	0.88387	0.99012	0.0833	24	0.005
H312	0.5213	0.82427	0.9937	0.0833	24	0.005
H313	0.44433	0.70545	0.85434	0.0833	24	0.005
H314	0.34731	0.76383	0.84971	0.0833	24	0.005
H315	0.17402	0.5566	0.84356	0.0833	24	0.005
H316	0.2711	0.49912	0.84592	0.0833	24	0.005
H317	0.27827	0.67413	0.77671	0.0833	24	0.005

H318	0.21204	0.52064	0.76866	0.0833	24	0.005
H319	0.40635	0.53068	0.78036	0.0833	24	0.005
H320	0.47735	0.68563	0.78535	0.0833	24	0.005
H321	0.33836	0.5459	0.70422	0.0833	24	0.005
H322	0.49303	0.61529	0.70971	0.0833	24	0.005
H323	0.50579	0.81127	0.71999	0.0833	24	0.005
H324	0.35255	0.74653	0.7117	0.0833	24	0.005
H325	0.52708	0.75003	0.64325	0.0833	24	0.005
H326	0.47017	0.84764	0.64468	0.0833	24	0.005
H327	0.26249	0.67345	0.63893	0.0833	24	0.005
H328	0.32155	0.57692	0.63472	0.0833	24	0.005
H329	0.211	0.49342	0.57303	0.0833	24	0.005
H330	0.15178	0.58947	0.57602	0.0833	24	0.005
H331	0.14293	0.59104	0.49843	0.0833	24	0.005
H332	0.20395	0.49782	0.49528	0.0833	24	0.005
H333	0.271	0.80203	0.49864	0.0833	24	0.005
H334	0.42497	0.86324	0.49457	0.0833	24	0.005
H335	0.28522	0.8059	0.57636	0.0833	24	0.005
H336	0.44023	0.86696	0.57189	0.0833	24	0.005
H337	0.42762	0.57633	0.56732	0.0833	24	0.005
H338	0.52404	0.73146	0.56729	0.0833	24	0.005
H339	0.41426	0.58065	0.48986	0.0833	24	0.005
H340	0.50775	0.735	0.49002	0.0833	24	0.005
H341	0.28625	0.5194	0.99904	0.0833	24	0.005
H342	0.44034	0.61414	0.99933	0.0833	24	0.005
H343	0.29012	0.50282	0.92183	0.0833	24	0.005
H344	0.44506	0.6	0.92189	0.0833	24	0.005

Organic template syntheses and characterisation

Synthesis and characterisation of 1,7-(1,4-DABCO)heptyl dibromide - (diDABCO-C7)Br_2

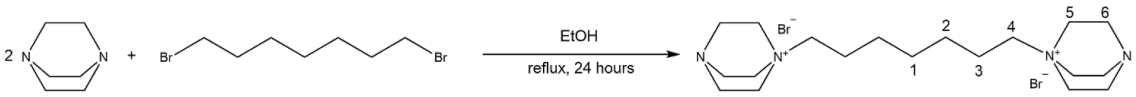

23.1 g (0.21 mol) 1,4-diazabicyclo[2.2.2]octane (DABCO, Sigma Aldrich) were dissolved in 100 mL ethanol and heated up to 50°C under stirring. Another solution was prepared by mixing 10.3 g (0.04 mol) 1,7-dibromoheptane (Sigma Aldrich) and 50 mL ethanol. This solution was added dropwise into the first one. The reaction mixture was refluxed for 24 h. The ethanol was removed by the rotary evaporator and the product was washed using cold diethyl ether, acetonitrile, and acetone. The resulting white solid (16.02 g, 83% yield) was dried overnight and then analysed by NMR.

^{1}H NMR: δ_H (500 MHz, D_2O) 1.27 (6 H, m, H1 and H2), 1.65 (4 H, m, H3), 3.08 (12 H, t, H6), 3.14 (4 H, m, H4), 3.28 (12 H, t, H5). **^{13}C NMR:** δ_C (126 MHz, D_2O) 21.0 (C3), 25.3 (C2), 27.7 (C1), 44.1 (C6), 52.0 (C5), 64.4 (C4).

Characterisation of pre-prepared 1,9-(1,4-DABCO)nonyl dibromide - (diDABCO-C9)Br_2

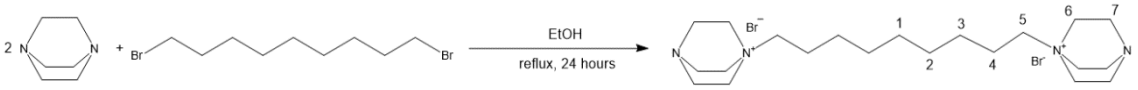

^{1}H NMR: δ_H (500 MHz, D_2O) 1.24 (10 H, m, H1+H2+H3), 1.65 (4 H, m, H4), 3.08 (12 H, t, H7), 3.14 (4 H, m, H5), 3.28 (12 H, H6). **^{13}C NMR:** δ_C (126 MHz, D_2O) 21.1 (C4), 25.5 (C3), 28.1 (C1 and C2), 44.1 (C7), 52.0 (C6), 64.6 (C5).

Synthesis of 1,10-(1,4-DABCO)decyl dibromide - (diDABCO-C10)Br_2

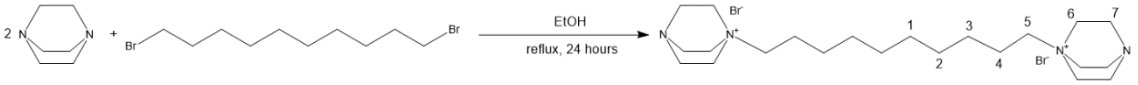

14.6 g (0.13 mol) 1,4-diazabicyclo[2.2.2]octane (DABCO, Sigma Aldrich) were dissolved in 50 mL ethanol and heated up to 50°C under stirring. Another solution was prepared by mixing 7.4 g (0.02 mol) 1,10-dibromodecane (Aldrich Chemical Co. Ltd.) and 70 mL ethanol. This solution was added dropwise into the first one. The reaction mixture was refluxed for 24 hours. The ethanol was removed by the rotary evaporator and the product was washed using cold diethyl ether, acetonitrile, and acetone. The resulting white solid (10.20 g, 78% yield) was dried overnight and then analysed by NMR.

^{1}H NMR: δ_H (500 MHz, D_2O) 1.22 (12 H, m, H1+H2+H3), 1.64 (4 H, m, H4), 3.08 (12 H, t, H7), 3.13 (4 H, m, H5), 3.28 (12 H, t, H6). **^{13}C NMR:** δ_C (126 MHz, D_2O) 21.1 (C4), 25.5 (C3), 28.1 (C1 and C2), 44.1 (C7), 52.0 (C6), 64.6 (C5).

Synthesis of offretite (OFF) and zeolite T material for comparison

1.71 g sodium hydroxide and 0.70 g potassium hydroxide are dissolved in 8.4 mL H_2O. Then, 1.34 g aluminium isopropoxide are added to the alkaline mixture and stirred at 100°C for 15 min or until complete dissolution. This mixture is added to 11.20 g colloidal silica (Ludox HS-40) and, then it is left to stir for 30 min. Finally, 0.18 g tetramethylammonium (TMA) chloride are added to the Teflon liner and the entire reaction mixture is left stirring for one hour. In the case of zeolite T, less is added to dissolve the inorganic bases and a hexamethonium bromide solution is prepared as well. The ratio of TMA^+:HM^{2+} is 1:4. This is added along with the tetramethylammonium chloride. Then, the reaction takes place in the stainless-steel autoclave at 100°C for 8 d. The white solid formed is washed with water under vacuum until the filtrate reaches pH lower than 10. The product is dried overnight at 65 °C.

Chapter 4

Figures

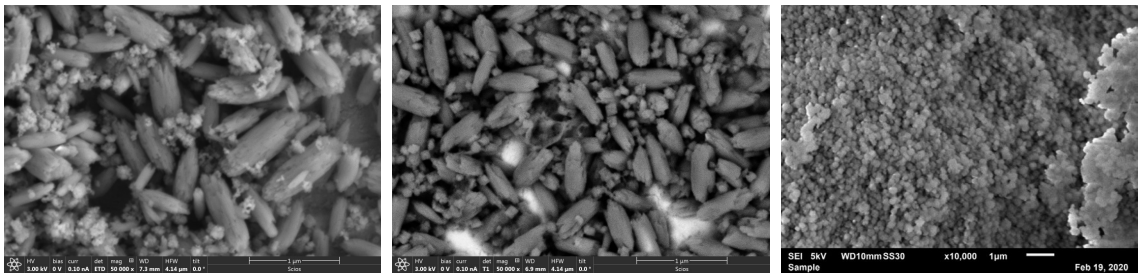

Sr-STA-30 Li-STA-30 Cs-STA-30

Figure 4.1 SEM images of Sr-STA-30 (left), Li-STA-30 (middle) and Cs-STA-30 (right).

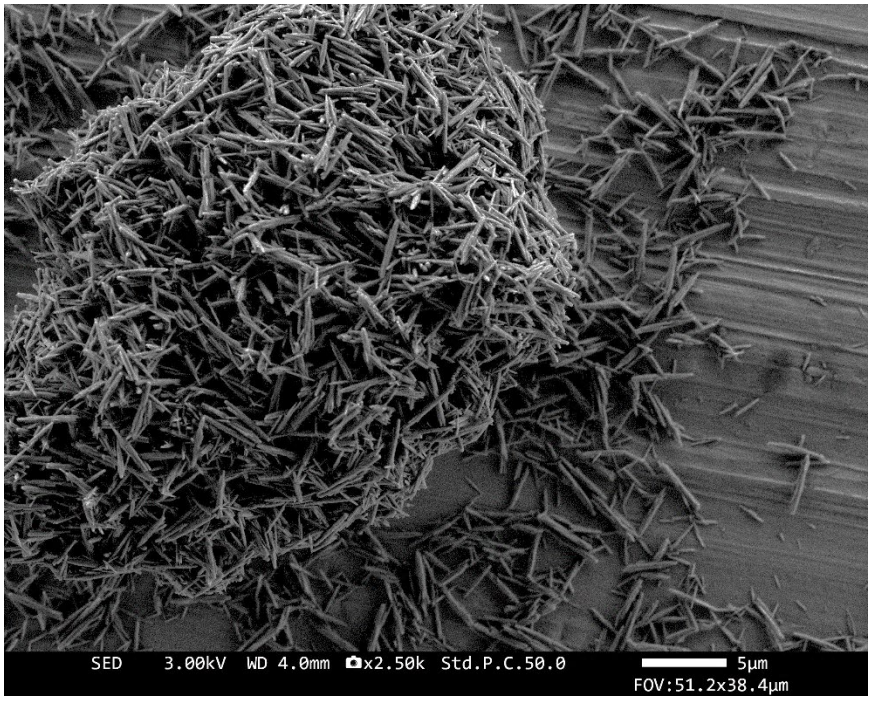

Figure 4.2 SEM image of diDABCO-C8-STA-30 synthesised through a CDM type approach from the following gel composition: 0.4 TPAOH : 0.05 Al_2O_3 : 1.0 SiO_2 : 0.16 $(diDABCO\text{-}C8)Br_2$: 0.2 KOH : 20 H_2O.

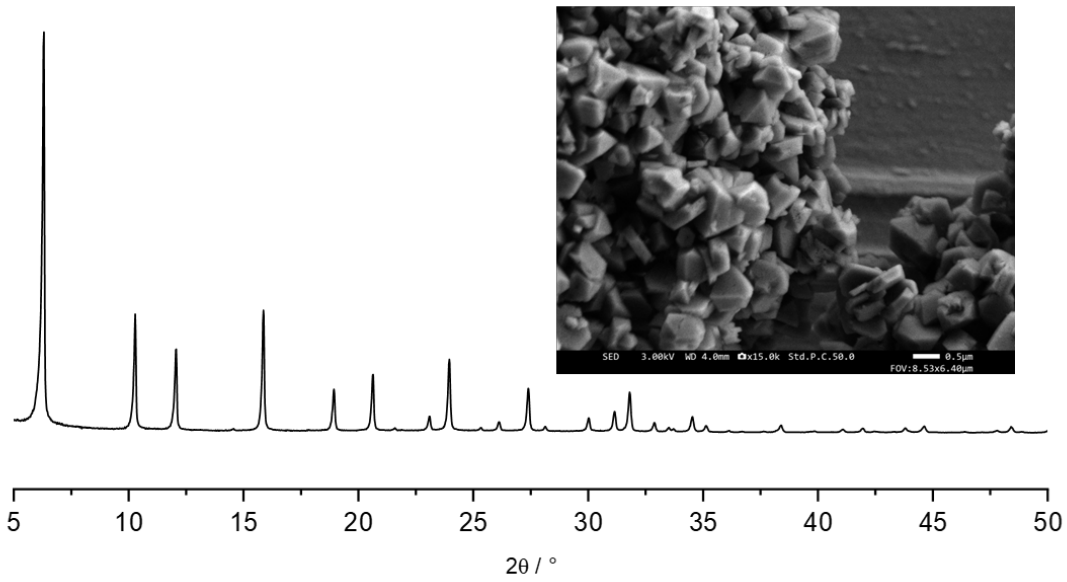

Figure 4.3 PXRD pattern and SEM image of CBV 712, used as Al and Si source in the partial IZC approach.

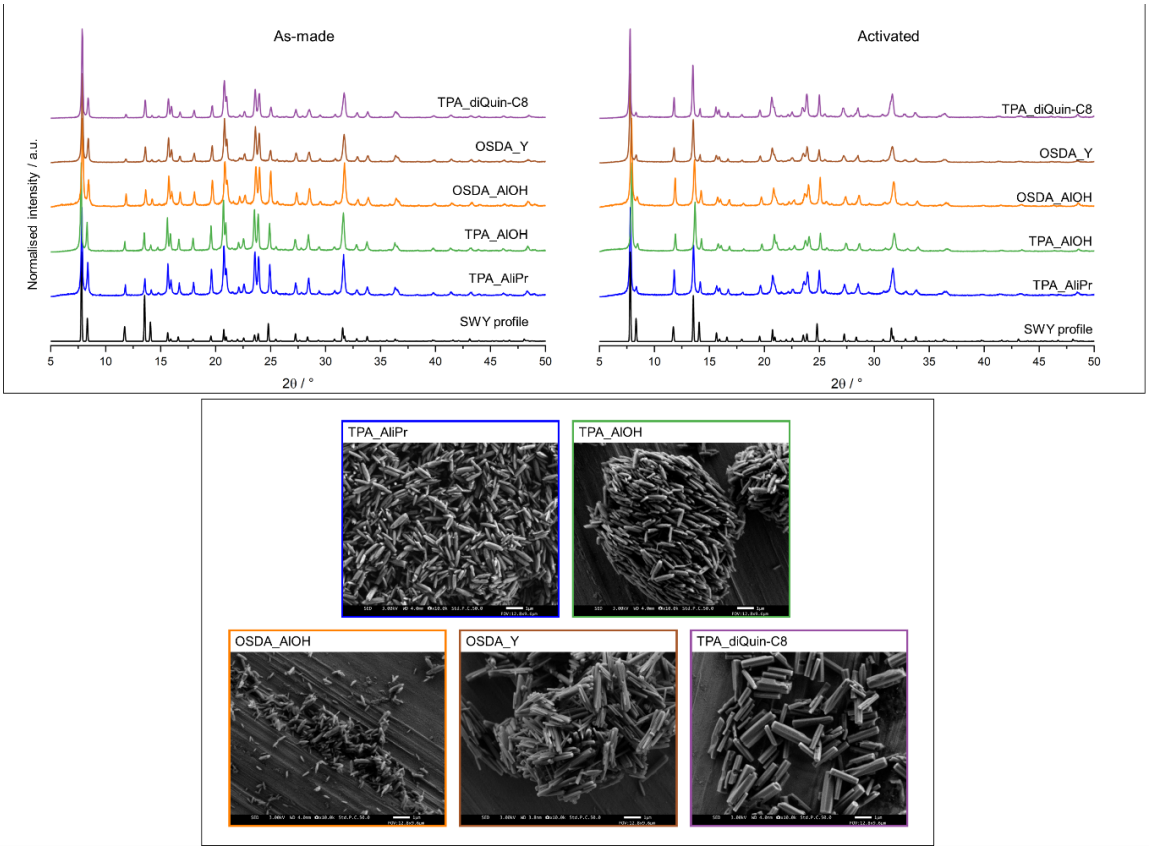

Figure 4.4 PXRD patterns of selected STA-30 samples in as-made forms (top, left) and activated forms (top, right). SEM images of the same selected samples (bottom).

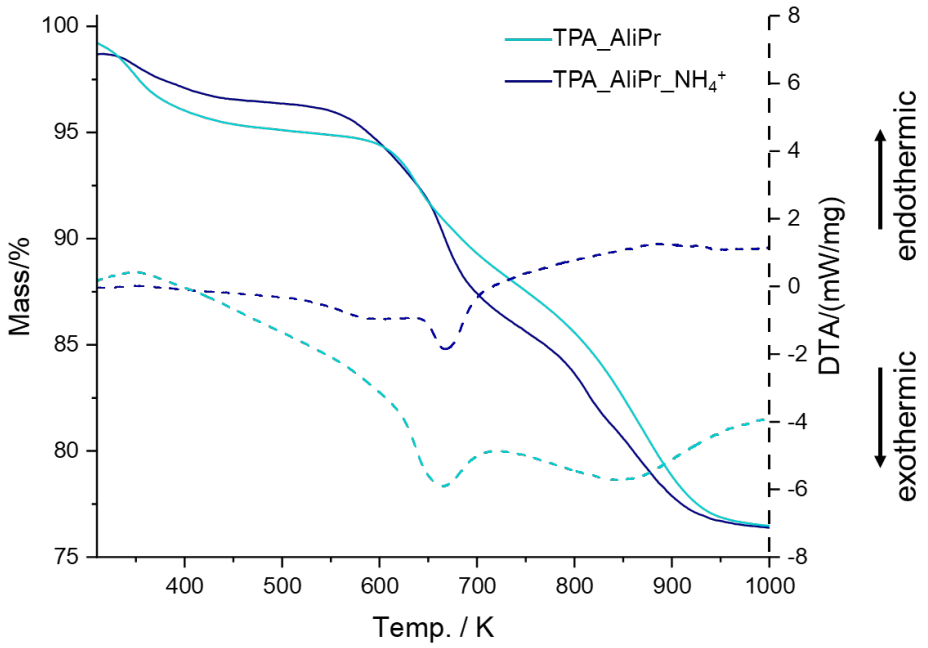

Figure 4.5 TGA mass loss curves and DTA analysis of as–made TPA_AliPr and TPA_AliPr as–made exchanged with NH_4Cl.

Synthesis and characterisation of di(Quin-C8)Br_2 (1,8–(1–azabicyclo[2.2.2]octane)octyl dibromide)

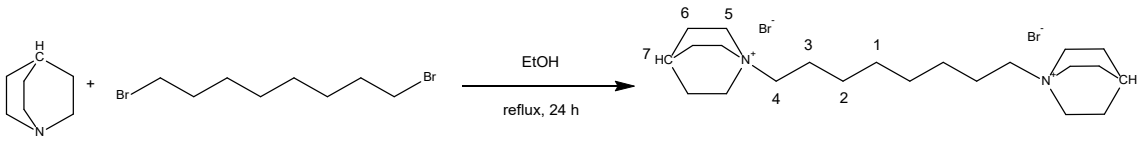

Figure 4.6 Reaction scheme for synthesis of (diQuin-C8)Br_2.

7.1 g (63.8 mmol) quinuclidine (TCI) and 9.2 g (33.1 mmol) 1,8–dibromooctane (Lancaster Chemicals) were dissolved in 120 mL ethanol. The mixture was heated under reflux for 24 hours. The solvent was removed with a rotary evaporator and the resulting white solid was washed with cold diethyl ether and acetone. The resulting white powder (15.6 g, 99% yield) was dried overnight and then analysed by NMR.

^{1}H NMR: δ_H (400 MHz, D_2O) 1.24–1.27 (8 H, m, H1+H2), 1.63 (4 H, m, H3), 1.90 (12 H, m, H6), 2.10 (2 H, m, H1), 3.02 (4 H, m, H4), 3.30 (12 H, t, H5). **^{13}C NMR:** δ_C (100 MHz, D_2O) 19.1 (C7), 21.4 (C3), 23.4 (C6), 25.6 (C6), 27.9 (C7), 54.6 (C5), 64.3 (C4).

Calculations of 'missing' *can+d6r* columns for the introduction of observed additional microporosity

$$Uptake\ (cm^3\ g^{-1}\ STP) = \frac{\frac{no.of\ Ar\ atoms/unit\ cell}{N_A} \cdot V_{m\ (STP)}}{\frac{M_{unit\ cell}}{N_A}}$$

$$= \frac{no.of\ Ar\ atoms/unit\ cell \cdot 22.4 \cdot 10^3}{M_{unit\ cell}}$$

Ar adsorption isotherm simulation performed on ideal SWY unit cell with K occupying all *can* cages which had the formula $K_4Si_{72}O_{144} \Rightarrow M_{unit\ cell\ ideal}$ = 4482.46 g mol^{-1}. At 50 kPa, the number of Ar atoms adsorbed into the unit cell according to the Sorption calculation was 39.7. Thus, by applying the formula above, the uptake of the ideal unit cell would be 198.4 cm^3 g^{-1}.

Ar adsorption isotherm simulation performed on 2×2×1 SWY supercell that had a column of *can* cages and d6r removed, H added for any Si–O terminations introduced through the removal and K positioned into all other *can* cages. This supercell had the formula $H_{24}K_{12}Si_{216}O_{444} \Rightarrow M_{supercell\ with\ vacancies}$ = 13663.57 g mol^{-1}. At 50 kPa, the number of Ar atoms adsorbed into this supercell according to the Sorption calculation was 208.3. Thus, by applying the formula above, the uptake of this supercell would be 341.5 cm^3 g^{-1}.

For a sample that is theoretically made up of a fraction of ideal SWY unit cells (considered below as an ideal 2×2×1 SWY supercell) and a fraction, $f_{vacancies}$, of 2×2×1 SWY supercells with removed *can* columns, the total uptake is made up of:

$$Total\ experimental\ uptake = \frac{f_{ideal} \cdot 198.4 \cdot M_{ideal} + f_{vacancies} \cdot 341.5 \cdot M_{supercell\ with\ vacancies}}{M_{dehydrated\ zeolite}},$$

$$\text{where } f_{ideal} + f_{vacancies} = 1\,,$$

$$M_{dehydrated\ zeolite} = f_{ideal} \cdot M_{ideal} + f_{vacancies} \cdot M_{supercell\ with\ vacancies}\ and$$

$$M_{ideal} = 17929.84\ g\ mol^{-1} and\ M_{supercell\ with\ vacancies} = 13663.57\ g\ \ mol^{-1}$$

The experimental uptake at 0.5 relative pressure for TPA_AliPr_H was 241.4 cm^3 g^{-1}. By plugging this number into the relationship above, the fraction of ideal unit cells and 2×2×1 supercells with vacancies are:

$$f_{ideal} = 0.64 \text{ and } f_{vacancies} = 0.36.$$

If ~36% of the structure of TPA_AliPr_H is described by the 2×2×1 supercell with a column of *can*/d6r cages removed and 3 columns intact, and the rest of the structure is described by the ideal unit cell, this means that ~9% of *can*/d6r cages have to be removed to introduce the additional porosity observed in TPA_AliPr_H.

The experimental uptake at 0.5 relative pressure for OSDA_Y_H was 212.3 $cm^3\ g^{-1}$. By plugging this number into the total uptake equation, the fraction of ideal unit cells and 2×2×1 supercells with vacancies are:

$$f_{ideal} = 0.88 \text{ and } f_{vacancies} = 0.12.$$

If ~12% of the structure of OSDA_Y_H is described by the 2×2×1 supercell with a column of *can*/d6r cages removed and 3 columns intact, and the rest of the structure is described by the ideal unit cell, this means that ~3% of *can*/d6r cages have to be removed to introduce the additional porosity observed in OSDA_Y_H.